POLITECNICO DI MILANO
DIPARTIMENTO DI ELETTRONICA, INFORMAZIONE E BIOINGEGNERIA
DOCTORAL PROGRAM IN INFORMATION TECHNOLOGY

DEVICES AND TECHNOLOGIES FOR LARGE-SCALE INTEGRATED PHOTONICS CONTROL

Doctoral Dissertation of:
Stefano Grillanda

Advisor:
Prof. Andrea Melloni

Co-advisor:
Dr. Francesco Morichetti

Tutor:
Prof. Michele D'Amico

The Chair of the Doctoral Program:
Prof. Carlo Fiorini

2014 – XXVII

Abstract

This thesis aims to develop novel devices and technologies to boost the complexity of integrated photonics and for the realization of complex photonic systems-on-chip. Here, a non-invasive integrated light observer was demonstrated in silicon photonics, enabling local monitoring of the status of a circuit without perturbing its operation and without wasting additional photons with respect to those naturally lost by the waveguide. Low-power, transparent actuators, based on the integration of photosensitive chalcogenide glasses with the silicon platform, were realized to provide post-fabrication permanent trimming functionalities both for compensation of fabrication tolerances and circuit reconfiguration. Furthermore, athermal and trimmable silicon waveguides were developed, in order to enable simultaneously passive thermal stabilization and post-fabrication trimming of silicon circuits. Also, resiliency of these devices to high-power induced thermal effects is shown. Active stabilization and feedback control of thermally actuated silicon resonators was demonstrated by exploiting an error signal provided by non-invasive light monitors integrated inside the microrings. Control functionalities such as wavelength tuning, locking and swapping are shown. Finally, advanced functionalities and concepts, such as transfer function recovery, reconfigurability, adaptability were addressed in high order filters and delay lines composed of several coupled ring resonators, and by even more complex integrated circuits, such as variable symbol-rate differential phase-shift keying receivers.

Acknowledgments

First, I would like to thank Prof. Andrea Melloni for making this PhD possible and for giving me the opportunity to work in his Group at Politecnico di Milano since my Master Degree thesis. I'm indebted to him for introducing me to the world of photonics, and for his valuable guidance, continous advice, and support over the years. A special thank goes also to Dr. Francesco Morichetti for following my work daily, and for constant help and invaluable discussion within my research activity.

I'm grateful to Dr. Antonio Canciamilla for teaching me most of what I know about working in a lab, and especially about photonic measurements. I thank all the colleagues and friends of the groups of Photonics Devices and Optical Communications at Politecnico di Milano, Daniele Melati, Carlo Ferrari, Alberto Gatto, Anna Boletti, Marco Brunero, Marco Mattarei and Andrea Annoni, with whom I shared much work but also fun and joyful moments.

I'm indebted to Dr. Anu Agarwal and Prof. Lionel Kimerling from MIT for giving me the opportunity to spend 7 months in the EMAT Group at MIT under their supervision, within a Progetto Rocca collaboration. I thank all the EMAT Group members, and especially friends and collegues Vivek Singh, Vivek Raghunathan, Neil Patel, and Juejun Hu for a fruitful and successful collaboration on the trimming of photonic devices over the years, and in particular for fabricating all the chalcogenide-assisted circuits utilized in this thesis.

I thank Prof. Marc Sorel and Dr. Michael Strain from the University of Glasgow for fabricating most of the silicon photonics devices and circuits

developed in this work.

I'm grateful to Dr. Marco Carminati and Prof. Marco Sampietro from Politecnico di Milano for the unique collaboration on the CLIPP, and for making this fabulous new device concept possible.

Finally, the biggest thank goes to my parents Giacomo and Giovanna, and to my sister Francesca, for continuous and loving support, and without whom all these great results and achievements would not have been accomplished.

Contents

Introduction

Integrated photonics has been imposing as an enabling technology in a broad variety of fields of application, such as for instance telecom [1], optical interconnects [2], bio-sensing [3], and quantum photonics [4]. Among the different photonic platforms, silicon (Si) plays a leading role, thanks to its ability of providing devices with unique performances in the manipulation of light on chip.

However, it is widely believed that the applications that will really benefit from the exploitation of the silicon platform are those requiring the aggregation of many components [5] into complex systems-on-chip for the delivery of advanced functionalities [6–8]. Indeed, much technological effort has been dedicated to scaling device dimensions down to the ultimate physical limit, so that now the silicon technology is mature enough to pack thousands of components into small chips [9]. Yet, the realization of large-scale integration circuits performing complex tasks is a challenge, and the result is that the perspective is still on the device rather than on the system [5].

In photonics, as in the case of electronics, device miniaturization is not a direct synonimous of device integration. In fact, integrated circuits cannot function properly without adequate tools to dynamically steer and hold each embedded device to the desired working point, counteracting functional drifts due to fluctuations in the environment, aging effects, mutual crosstalk, and fault events. Indeed, as the scale of integration increases the aforementioned effects become critical, and consequently monitoring, control and stabilization of components is mandatory. At the same time, while

aggregating several devices, the power consumption required by tuning and control operations should not increase as well.

This thesis aims to fill the existing gaps that are currently preventing photonic integrated circuits (PICs) to move from a single-device level to a new system-on-chip paradigm. Although most of the work here presented refers mainly to silicon photonics, the concepts and ideas that are developed can be extended to other photonic integrated platforms.

In particular, Chapter 1 provides some state-of-the-art, background information, and motivations for this work, describing the scenario and main applications of PICs, and what devices and technologies are beneficial to increase the scale of integration in photonics. Also, integration with electronics and some significant examples of exploitation of Si photonics circuits, such as in large-scale optical interconnection networks and in space-division-multiplexing (SDM) systems, are provided.

Chapter 2 presents low-power actuators and post-fabrication trimming techniques for PICs, based on the integration of photosensitive As_2S_3 chalcogenide glass with photonic waveguides. First the concept of photo-induced trimming is described with reference to As_2S_3 core waveguides, then is extended to Si photonic waveguides and devices. Permanent trimming of the spectral response of an As_2S_3-assisted Si microring resonator is shown; performances of the trimming process in terms of stability, saturation and speed are investigated in detail. Also, optimization of the waveguide design and non-linear behavior of As_2S_3-assisted Si waveguides are reported.

Chapter 3 is entirely dedicated to the ContactLess Integrated Photonic Probe (CLIPP), that is a novel non-invasive observer of light, here proposed and experimentally demonstrated in Si photonic waveguides and circuits. This Chapter begins with a description of the concept of non-invasive light observation in Si photonic waveguides, then investigation of the non-perturbative nature of the CLIPP and application to multipoint light monitoring is provided. Finally, details on the electronic experimental setup, systematic investigation of the CLIPP performances (dependence on waveguide geometry, polarization, wavelength, speed and sensitivity, parasitism and miniaturization), and extension of the CLIPP to other photonic platforms such as indium phosphide (InP) are reported.

Chapter 4 provides thorough information on the physical mechanisms behind the CLIPP. In particular, surface-state-absorption (SSA) is identified as the physical effect responsible for the operation of the CLIPP by excluding all the other possible mechanisms. Then, a novel all-optical technique for probing and measuring the effects of SSA (generated carriers and absorption) in Si photonic waveguides is developed, providing direct ex-

perimental evidence that SSA is the mechanism exploited by the CLIPP.

Chapter 5 focuses on the stabilization and feedback control of Si PICs. First, athermal and trimmable Si waveguides are demonstrated, providing simultaneously passive thermal compensation and post-fabrication trimming functionalities to Si circuits. Also, passive thermal mitigation is demonstrated even at high power, thus pushing toward a concept of power insensitive Si devices. Then, feedback control of thermally actuated Si resonators is realized with the assistance of the CLIPP, that is integrated inside the microring. Advanced control functionalities, such as wavelength tuning, locking, and swapping assisted by the CLIPP are demonstrated in a resonator. The Chapter ends with a Section dedicated to the process of fiber-to-waveguide alignment, that is here achieved with the CLIPP and feedback loops. Although this application slightly differs from the previous ones of this Chapter, it is well suited within a discussion on stabilization and feedback control.

Finally, the last part of this thesis (Chapter 6) presents examples and applications of complex photonic circuits that exploit the devices and technologies developed in the previous parts of this manuscript (CLIPP, feedback control, trimming etc.), thus clearly showing the vision, perspective, and outlook of this work. In particular, advanced functionalities such as transfer function recovery, reconfiguration and local monitoring of complex filters and delay lines composed of several coupled resonators are demonstrated. The Chapter ends with the demonstration of an even more complex PIC, that is a variable simbol-rate differential phase-shift keying (DPSK) receiver in silicon photonics, thus opening the way to the implementation of adaptive functionalities. Device concept, experimental results, and resiliciency versus high-power thermal effects are reported.

CHAPTER 1

From a device perspective to a system-on-chip paradigm

This chapter provides some state-of-the-art and background information for the work that is developed in the next Chapters of this thesis. In particular Sec. 1.1 motivates the need of scaling the complexity of photonic integrated circuits. Section 1.2 describes what devices and technologies are needed to keep photonics under control, while issues of integration with electronics are briefly introduced in Sec. 1.3. Finally, Sec. 1.4 shows some examples of the main applications and fields of exploitation of complex and large scale integration PICs.

1.1 Scaling the complexity of integrated photonics

Integrated photonics technologies have reached incomparable results in the manipulation of light so that today a large variety of components and functionalities are available among the different photonic platforms. The significant development of photonic technologies is directly reflected by the deep penetration of integrated optics in a number of applications where it has become a game-changing technology, such as for instance telecom [10],

optical interconnections [2], bio-sensing [3], and quantum photonics [4].

Indeed, in this scenario, a leading role is played by the silicon photonics platform, that provides both passive and active devices with best-in-class performances, such as low-loss waveguides [11, 12], complex switches [1], low-power modulators [13], and photodetectors [14, 15]. In addition, the miniaturization of components has been pushed so far that now the silicon platform is mature enough to squeeze thousands of components in a footprint of less than 1 mm^2 [9]. Yet in photonics, like in analog electronics, device miniaturization is not a direct synonimous of device integration [16, 17]. The result is that, although extensive research effort has been dedicated to miniaturization and development of single devices [5], the integration of many components into complex photonic systems-on-a-chip for the delivery of advanced functionalities is still a challenge [5, 6].

In addition to the need of scaling the complexity and boosting the integration of photonic components, integrated optics technologies have to respond to urgent needs of adaptability and programmability, which are imposing as new key concepts in photonics, and enable the realization of arbitrary, reconfigurable, complex circuits.

The issue is that photonic integrated circuits are inherently imperfect because their operation is significantly limited by the effects of fabrication tolerances, thermal fluctuations, cross-talk effects, aging, fault events etc. For instance, this is easily confirmed if one considers that a 1 nm deviation in the width of a sub-micrometer silicon waveguide is enough to induce a wavelength shift of 100 GHz in the transfer function of any interferometric device, or that a thermal drift by 1°C results in a 10 GHz wavelength shift.

The key is in keeping photonics under control. As in analog electronics, photonic integrated circuits cannot function properly without adequate tools to dynamically steer and hold each embedded device to the desired working point. In this sense, in order to have photonic integrated circuits leaping from device level to system-on-a-chip paradigm, and to respond to urgent needs of reconfigurability and adaptability, operations such as monitor, control and reconfiguration of the circuit functionality are highly needed.

1.2 Keeping photonics under control

As anticipated, evolution from photonic integrated devices to photonic integrated systems require to keep optical components under control, so that the detrimental action of fabrication tolerances, temperature fluctuations, cross-talk etc. is mitigated and the circuit is locked to the desired working

point. The dream is to have a way to monitor a circuit non-invasively and to apply a simple, fast and robust feedback control. To this aim, three main existing gaps of current photonic technologies need to be addressed.

Low-power actuators

Scaling up the complexity of photonic integrated circuits should be achieved without increasing at the same time the power consumption required for tuning, reconfiguration and control operations, and with no need of a continuous, always-on energy consumption to hold the state of the circuit.

With reference to the silicon platform, typical actuators are based on the thermo-optic effect, thus requiring a power consumption in the order of few mW to achieve a π shift in a μs time scale (more power-efficient solutions have been proposed, yet typically requiring a longer switching time [18]). This high power consumption, along with thermal crosstalk, prevents their integration on large scale circuits. Other typical actuators involve the use of biased junctions to achieve fast switching, however they typically suffer from high power consumption or low phase shift efficiency [19, 20] (though recent results showed that with quite advanced and complex structures power consumption can be significantly reduced [13]).

Other approaches employ liquid crystals, however they require high control voltages [21] and result in a dramatic increase of the loss [22], or are based on the switching of state of phase-change-materials (PCMs), such as GeSbTe compounds [23], and oxides such as VO_2 [24], yet light propagation is typically inhibited in one of the switching states.

This thesis exploits the use of photosensitive As_2S_3 chalcogenide glasses that are integrated with silicon waveguides (nonetheless this approach is general and can be extended to other photonic technologies). By changing the refractive index of the chalcogenide material with low-power, near band-gap illumination the effective index of the waveguide can be varied, without introducing any appreciable loss to the waveguide. This enables permanent trimming of photonic devices and circuits with no need of a continuous power consumption (Chapter 2, 5, 6) and post-fabrication treatments in polymer-coated athermal devices (Chapter 5).

Transparent photodetectors

Local inspection and monitoring of the status of a photonic device is fundamental in order to steer and hold the circuit to the desired functionality. Typically in integrated optics this is realized by tapping a portion of the light from the waveguide [13, 25–27] in order to re-route it to a photodetec-

tor [14, 15]. Indeed this is invasive, and consequently only a few probing points can be placed in a circuit, otherwise a large amount of power would be wasted for monitoring operations.

Although in literature tap monitors of only small percentages have sometimes been utilized [28], light tapping from the waveguide represents a significant limitation for photonic integration, suggesting that the use of a fully transparent light detector is required.

This thesis proposes, experimentally demonstrates, and exploits in practical system-level applications a non-invasive light monitor (i.e., the CLIPP) for silicon photonic waveguides. This transparent monitor exploits the interaction of the optical mode with intrinsic surface states, and neither absorbs additional photons with respect to those naturally lost by the waveguide, nor introduces significant perturbations of the optical field (Chapters 3, 4, 5, 6). Thanks to its non-invasive nature, the CLIPP is an enbling technology for large scale circuits where many components need to be monitored and controlled. Though most of the work is here developed in Si waveguides, application to InP devices is shown, and extension to most semiconductor technologies is expected.

Stabilization and feedback control

A control plane should be provided to complex photonic circuits in order to steer and hold its functionality. In particular, feedback control loops are beneficial to stabilize the circuit operation and hold its status to the desired working point in presence of impediments like thermal fluctuations or cross-talk.

Recently, several approaches have been proposed and demonstrated in silicon photonics for the stabilization of resonators and microring modulators [13,25–27], yet as anticipated in the previous sections most approaches require the use of tap photodetectors to probe the status of the circuit, and therefore are hardly scalable to many components.

Here, feedback control for the circuit stabilization against temperature drifts and laser wavelength detuning is demonstrated in thermally actuated silicon devices by using feedback loops assisted by the CLIPP (Chapter 5), thus not requiring any light tapping from the waveguide.

Furthermore, passive stabilization of silicon devices versus thermal fluctuations is achieved by using novel athermal and trimmable waveguide structures, that are realized by integrating silicon waveguides with chalcogenides (for trimming) and polymers with negative thermo-optic coefficient (for thermal compensation) (Chapter 5).

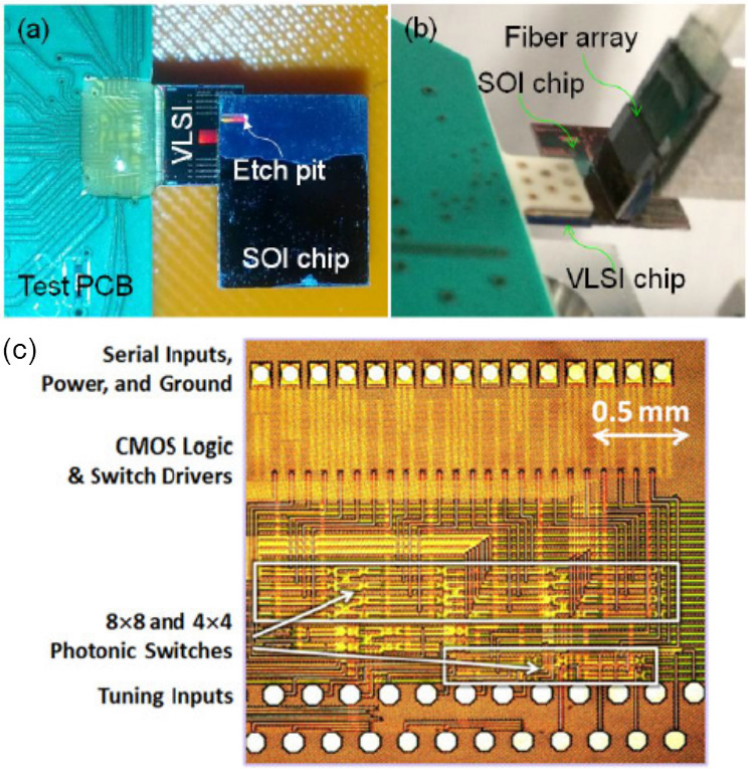

Figure 1.1: *Examples of state-of-the-art demonstrations of (a)-(b) hybrid photonic-electronic integration by Oracle (reproduced from 2014 OSA [29]) and (c) monolithic integration by IBM (reproduced from 2014 IEEE [30]).*

1.3 Integration with electronics

When dealing with large-scale integration PICs or complex systems-on-chip issues of integration with electronics to manage each photonic device (in terms of delivery of the electric signals for tuning and feedback control, and to bias devices such as modulators or detectors) should be taken into account.

Figure 1.1 report some state-of-the-art examples that represent two different approaches to photonic-electronic integration. Figure 1.1(a) and (b) show a nice demonstration of hybrid integration by Oracle [29]. In this case, a 10 Gbit/s silicon microring modulator, with integrated germanium (Ge) photodetector for power monitoring and integrated heater for tuning and feedback control, is fabricated using a 130 nm silicon-on-insulator (SOI) CMOS process. Then the Si photonic chip is hybrid integrated with

40 nm bulk CMOS chip that hosts the driver for the 10 Gbit/s modulator and the circuitry to manage the closed-loop control.

The other example [Fig. 1.1(c)] is a recent demonstration by IBM [30] of monolithic integration. In this case 4×4 and 8×8 Si switch fabrics, composed by cascaded Mach-Zehnder interferometers (MZIs), are integrated onto a single chip that hosts also digital CMOS logic, drivers for the devices, thermo-optic tuners and electro-optic modulators, fabricated with IBM's 90 nm Si integrated nanophotonic technology.

It is not clear yet which integration philosophy will dominate the future market. According to [30], monolithic integration enables complex optoelectronic cicuits, and potentially could reduce the cost of the system. However, which approach will be more convenient in the long run (in terms of scalability, cost, volume production etc.) has yet to to be understood.

1.4 Exploiting complex photonic systems-on-chip

As anticipated in the previous sections, controlling photonic integrated circuits by means of transparent photodetectors, low-power actuators, and closed-loop algorithms is a necessary step toward a real scaling of the complexity and integration scale of photonics. Indeed, large-scale PICs are an enabling technology in different fields; here we motivate the need of boosting photonics integration with reference to two significant applications of silicon photonics: optical interconnection and switching networks, and arbitrarily reconfigurable optical components.

Optical interconnection and switching networks

Silicon photonics is currently envisioned as the primary technological platform to overcome the limitations of traditional interconnections based on copper/dielectric paradigms [2, 31]. Several interconnection networks and switch fabrics implementations [1, 30, 32–35], based on MZIs or ring resonator switches, have been proposed in literature (some state-of-the-art examples are reported in Fig. 1.2).

However, their performances are extremely sensitive to thermal drifts and cross-talk effects, thus requiring a perfect reconfiguration and optimization of the status of each switching element [30], otherwise the price to pay is a significant reduction of the extinction ratio between the routed channels, thus inducing an overall degradation of the circuit. In the end, the result is that, although the silicon platform can potentially allow switching and routing of several channels, the number of ports that have been interconnected is still moderate.

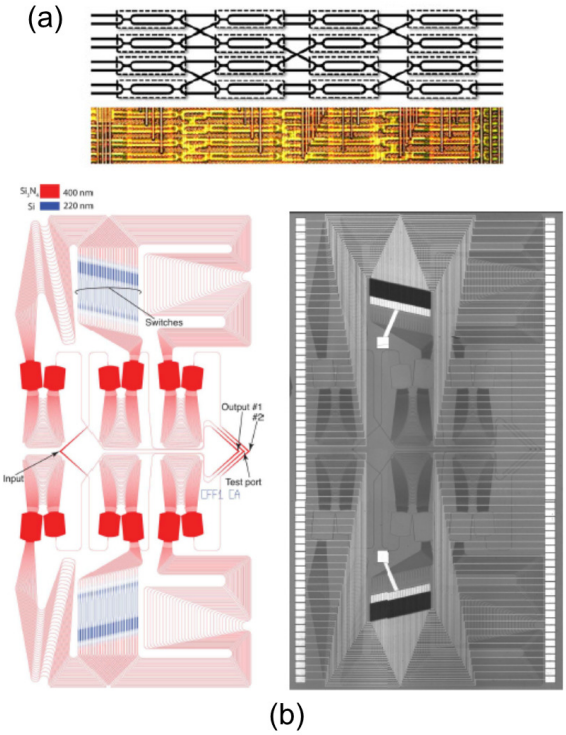

Figure 1.2: *Applications of complex photonics systems-on-chip. (a) 8x8 switch fabrics in silicon photonics by IBM (reproduced from 2014 IEEE [30]). (b) Wavelength selective switch in silicon photonics by Bell Labs (reproduced from 2012 IEEE [1]).*

Indeed, the complexity of state-of-the-art solutions can be significantly scaled up by improving the ability to monitor and control each switching element with local and transparent photodetectors. Also, with the use of local feedback loops, global multiparameter optimization and complex look-up tables can be avoided. Furthermore, the integration of low-power actuators would allow the scaling of the circuit while keeping low the power consumption.

Arbitrarily reconfigurable optical components

The potential of arbitrarily reconfigurable photonics and the enabling conditions at which it can be realistically achieved have been recently envisioned by Miller [6, 7]. He demonstrated that a set of optical elements, like the arrangement of MZIs shown in Fig. 1.3(a) [7], can self-configure to perform any linear function or mode mapping [36] between inputs and

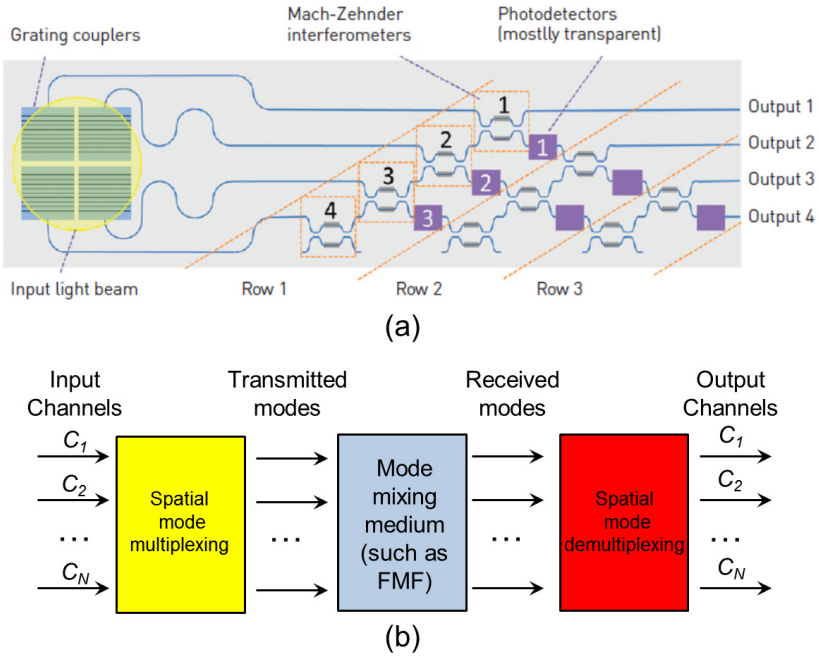

Figure 1.3: *Applications of complex photonics systems-on-chip. (a) Arbitrarily reconfigurable linear mode converter (reproduced from 2013 OSA [7]). (b) Typical architecture of space-division-multiplexing (SDM) systems where integrated optical components are much needed to perform mode multiplexing/demultiplexing functions.*

outputs. Feedback-control is mandatory to steer and hold the entire system to the desired functionality, and make it immune to fabrication tolerances, functional and environmental drifts, and mutual crosstalk effects. Local feedback loops, setting individual optical elements within the circuit, appear a more viable route than global multiparameter optimization of the entire system, yet requiring multipoint monitoring of the circuit status through transparent on-chip detectors.

Arbitrary reconfigurable circuits have a direct and strong impact on several applications, such as for instance on systems employing space-division-multiplexing (SDM) [37], which is currently envisioned as a viable approach to significantly scale the capacity of optical fibers [38]. Figure 1.3(b) shows the typical architecture of a SDM system, where different information channels C_i are transmitted on spatial modes of a medium, such as few-mode-fibers (FMF) [39], that can introduce a strong mixing between the modes, so that after propagation electronic [40] or all-optical multiple-input multiple-output (MIMO) [8, 10] is required to recover the transmitted

channels. In this scenario, integrated devices and components, such as spatial multiplexer/demultiplexer, all-optical MIMO, and mode converters are much needed [41].

The circuit of Fig. 1.3(a) is essentially a mode-converter [36], and therefore offers a nice integrated platform to implement SDM components. However, this circuit cannot function unless transparent detectors and feedback loops are utilized. In fact, when optimizing the working point of each element of the circuit, additional mode-dependent loss should not be introduced, otherwise orthogonality between the modes would be lost [41], and the desired unscrambling/scrambling of the modes would not be accomplished. In this sense, this circuit cannot be realized with conventional, state-of-the-art, power-hungry, tap detectors. Furthermore, the use of low-power actuators to set the status of each element enables to scale this circuit to an arbitrarily large number of modes without increasing at the same time the power consumption required by control operations.

CHAPTER 2

Low-power actuators

The strong light confinement offered by high index contrast technologies, such as silicon photonics, enables the realization of ultra-small footprint and large bandwidth photonic integrated circuits. However, high index contrast and sub-micrometer waveguide dimensions are also responsible for a strong sensitivity to fabrication tolerances, that currently represent one of the main constraints of silicon PICs.

For instance, considering a typical monomode nanowaveguide, a width deviation of only 1 nm causes an effective index variation of about $2{\cdot}10^{-3}$, producing a frequency shift of about 100 GHz in the spectral response of any interferometric device [42–44]. Even for the most advanced and highly accurate fabrication processes, these figures pose huge technological challenges and severe design constraints, especially for resonant, multi-stages or high-quality-factor devices [42, 43, 45–47].

Post-fabrication treatments, enabling to finely tailor the local properties of silicon PICs, are therefore mandatory to compensate for unavoidable fabrication inaccuracies in order to recover the desired specifications and functionalities. Moreover, they also open the way to the realization of PICs with complex and reconfigurable transfer function (see also Chapter 6).

Active tuning techniques, such as local heating through thermo-optic

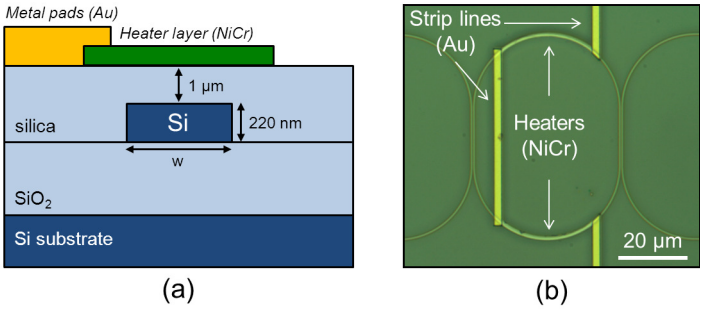

Figure 2.1: *(a) Cross-sectional view of a Si waveguide where the thermal actuator structure, that is composed of a heater layer in NiCr (green) and a Au layer (brown), is visible. (b) Photograph of a microring resonator where a thermal actuator is integrated. Waveguide width is typically w = 480 nm to ensure monomode propagation on TE polarization.*

actuators [48] or carrier injection through p-i-n junctions [49], are commonly used. Nevertheless they require additional fabrication steps and, being based on "always-on" mechanisms, are inherently power-hungry and poorly efficient when continuous and fast reconfiguration is not required, especially when integrated in circuits aggregating several components [9]. For this reason, actuators enabling to tune or trim the circuit response with low power consumption are highly desired in photonics.

The first section (Sec. 2.1) of this chapter analyzes the typical structure and performances of conventional thermo-optic actuators that are utilized in this work, whereas the second one (Sec. 2.2) is entirely dedicated to the description of novel low-power actuators and post-fabrication trimming based on photosensitive As_2S_3 chalcogenide glasses (ChGs). Although here they are integrated onto the silicon platform, in general they can be applied for the trimming of any photonic technology or circuit. Design, optimization, fabrication, and experimental performances are thoroughly investigated.

2.1 Conventional thermo-optic actuators

Figure 2.1(a) shows the cross-section of the silicon waveguides here utilized, with the typical structure of the thermal actuators, as fabricated by the James Watt Nanofabrication Centre (JWNC) at the University of Glasgow. The waveguide core, that is patterned by electron-beam lithography according to the process described in [11], has width $w = 480$ nm and height 220 nm and is buried in a silicon dioxide (SiO_2) cladding (see Sec. 3.2 for additional details on waveguide fabrication). The NiCr heaters [in green

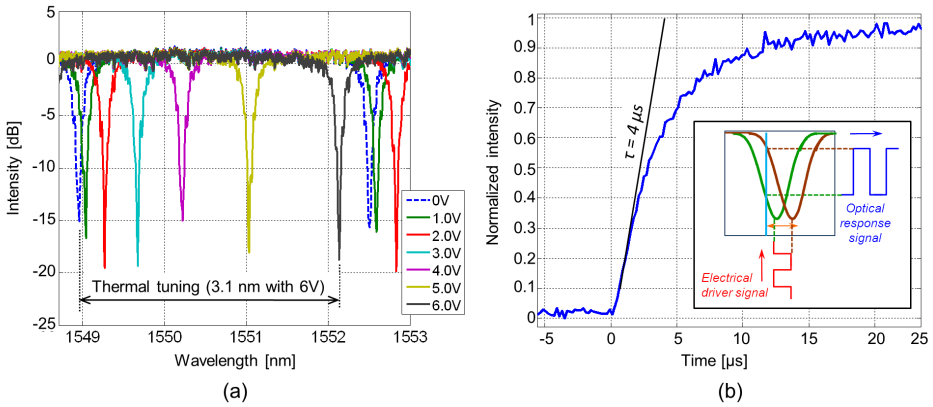

Figure 2.2: *Performances of the thermal actuator integrated in the microring. (a) Spectral response of the resonator for different voltage applied to the heater from 0 to 6 V, the achieved wavelength shift indicates a tuning efficiency of about 52 μW/GHz. (b) Temporal response of the heater when the applied voltage is modulated with a square wave, indicating a time constant τ = 4 μs. (Courtesy of Dr. Antonio Canciamilla).*

in Fig. 2.1(a)] have a width of 900 nm and a thickness of 50 nm, and are deposited on top of the silica cladding, at a distance of about 1 μm from the Si core; Au contacts instead have a typical thickness of 200-300 nm. A 20 nm thick Ti layer is deposited under the NiCr/Au layer to ensure adhesion between the metal and the silica cladding. Both the NiCr heater and the Au contacts are patterned by means of a conventional lift-off technique.

The heaters were deposited on top of microring resonators [Fig. 2.1(b)] to tune their transfer function. The total length of the thermal actuator is about 54 μm, whereas its geometry is designed in order to have no overlapping with the coupling regions of the resonator, thus minimizing thermal crosstalk with the directional coupler.

Figure 2.2(a) shows the transfer function of the fabricated microring for increasing voltages applied to the heater from 0 (blue dashed line) up to 6 V (black solid line). The resonant wavelength rigidly red-shifts as the heater voltage is increased achieving a total wavelength shift of 3.1 nm (388 GHz) with 6 V (the FSR of the resonator is about 3.5 nm). This means that the average power consumption for this heater technology is around 52 μW/GHz, that is more than 200 times smaller than that required by silica-based technologies [50]. This energy consumption is roughly in line with that typical of thermal actuators in silicon photonics [51], however it can be reduced by about one order of magnitude by thermally isolating the microring from the silicon substrate [18, 52], yet at the price of slowing

down significantly the time constant of the heater [18].

Finally, in order to investigate the time response of the fabricated thermal actuators the voltage applied to the heater pads was modulated with a square wave [inset of Fig. 2.2(b)] while the optical intensity at the output of the resonator was recorded versus time with an oscillope. As shown in Fig. 2.2(b), the heater exhibits a time constant τ of about 4 μs, thus requiring only 12 μs to achieve 90% of the desired optical intensity. Though the μs-time scale is typical for thermo-optic actuators in silicon photonics [51], faster thermal actuators ($\sim$100 ns time scale) can be achieved by direct pulsed excitation of the silicon layer [53]; even faster time response can be achieved by means of actuators based on carrier injection through p-i-n junctions [49].

2.2 Low-power actuators based on photosensitive chalcogenides

Recently, permanent trimming techniques, where the induced refractive index change does not disappear when the trimming source is switched off, have attracted great interest in order to significantly reduce the power consumption required by conventional heaters or carrier injection based actuators.

The trimming of silicon microring resonators has been demonstrated by exploiting the oxide compaction induced by electron beam exposure [54] or the silicon oxidation induced by the tip of an atomic force microscope [55]. Although large (up to $1.3{\cdot}10^{-2}$) effective index variations can be achieved, these techniques require sophisticated, expensive and power-consuming equipment, that is hardly in line with low-cost manufacturing and makes real-time monitoring of the process difficult. A more flexible solution, successfully applied to both Si photonic crystal cavities [56] and microring resonators [57], is the use of a highly localized laser beam to selectively induce oxidation, amorphization or nanomilling of the silicon surface. Nevertheless it needs very high energy density (in the order of 10^8 and 10^{15} mW/cm^2, respectively) and is affected by transient thermo-optic and surface chemistry effects. Alternative techniques, used on different high index contrast technological platforms, employ UV sensitive polymer films as waveguide cladding [58, 59], whose refractive index is tailored by local ultra-violet (UV) exposure. Besides requiring a UV-source for the trimming, most polymers suffer from poor temporal stability and optical degradation at relatively low temperatures.

Here, an innovative approach to realize trimmable silicon PICs is proposed and demonstrated. Chalcogenide-assisted silicon waveguides are

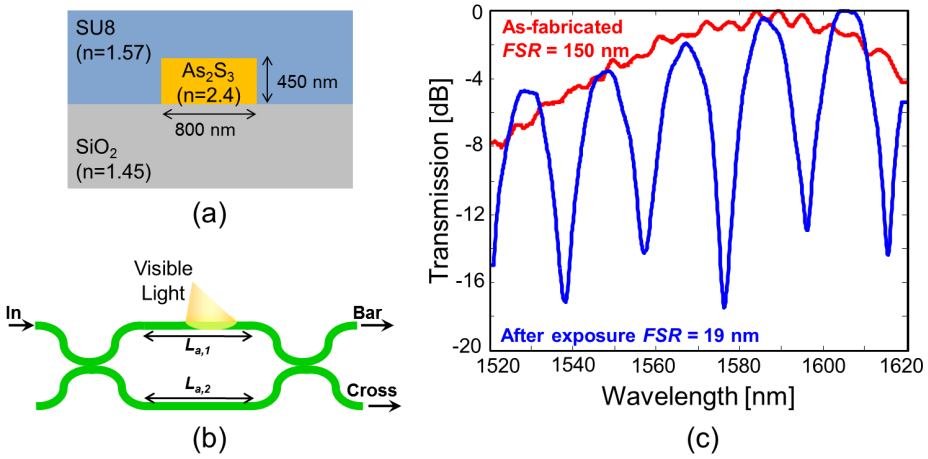

Figure 2.3: *Photo-induced trimming of As_2S_3 MZIs. (a) Schematic view of the cross section of the fabricated As_2S_3 core waveguides (dimensions, materials and refractive indices are also reported); (b) Schematic layout of the fabricated Mach-Zehnder interferometer; (c) Spectral response at the Cross port of the as-fabricated device (red line) and after visible light exposure (blue line).*

made by depositing As_2S_3 glass as upper cladding in an otherwise standard Si process. The photosensitivity of ChG materials is then exploited to selectively tailor the local optical properties of the waveguides, by using nothing more than a low-intensity visible-light source. The trimming technique is simple, accurate, low-cost, and permanent, enabling compensation for fabrication tolerances and reconfiguration of the circuit transfer function (see also Sec. 6.1-6.2). Its performances are investigated in detail by trimming the resonance frequency of a silicon microring resonator: saturation effects, velocity and temporal stability of the process are characterized and the optimum design of the ChG-assisted Si waveguide is discussed.

The properties of this waveguide technology are described first with reference to As_2S_3 chalcogenide core waveguides and devices (Sec. 2.2.1), and then on the aforementioned As_2S_3-assisted silicon waveguides and circuits (Sec. 2.2.2, 2.2.3, 2.2.4, 2.2.5, 2.2.6).

2.2.1 As_2S_3 chalcogenide waveguide

Channel waveguides in As_2S_3 chalcogenide glass were fabricated at MIT according to the cross-sectional schematic reported in Fig. 2.3 (a). A 450-nm-thick film of As_2S_3 with refractive index 2.4 was thermally evaporated on a silica buffer oxide. The 800-nm-wide waveguides, optimized

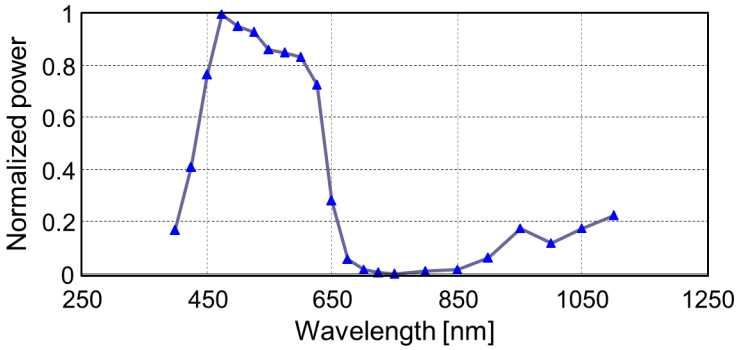

Figure 2.4: *Normalized spectrum of the lamp utilized for the trimming of the devices, most of the emission is included between 450 and 650 nm with an intensity that can be varied from 0.3 mW/cm^2 to 10 mW/cm^2.*

for tranverse-magnetic (TM) polarization, were then patterned by lift-off lithography and covered by a SU8 polymer with refractive index 1.57 according to the fabrication tecnique described in [60].

By employing this waveguide structure, balanced MZIs were fabricated, according to the scheme of Fig. 2.3(b), with nominally identical arms of length $L_{a,1}$ = $L_{a,2}$ = 20 mm, and input/output 50% directional couplers. Due to the tolerances of the fabrication process, the devices exhibit a spectral response at the Cross port with a free-spectral-range FSR = 150 nm [Fig. 2.3(c), red line], implying a difference in the group indices of the waveguides forming the arms of about $9.3{\cdot}10^{-4}$.

In order to implement the trimming procedure, one of the arms of the interferometer was entirely exposed to visible light radiation, as depicted in the schematic of Fig. 2.3(b), by means of a multimode optical fiber (30 μm mode field diameter) placed on top of the chip and coupled to a halogen lamp, the position of its end-facet being controlled by a micro-positioning stage in order to expose only desired areas of the circuit. The lamp has a spectrum in the range 450-650 nm (Fig. 2.4) and an intensity which can be varied from 0.3 mW/cm^2 to 10 mW/cm^2. During the whole trimming procedure the rest of the device is kept in dark. At the end of the light exposure the device has FSR = 19 nm [Fig. 2.3(c), blue line], which corresponds to an unbalance in the group indices of the waveguides forming the arms of about $6.1{\cdot}10^{-3}$. Therefore, the visible trimming light has progressively changed the group index of the exposed waveguide up to about $5.2{\cdot}10^{-3}$, which corresponds to a variation in the index of the As_2S_3 glass of about

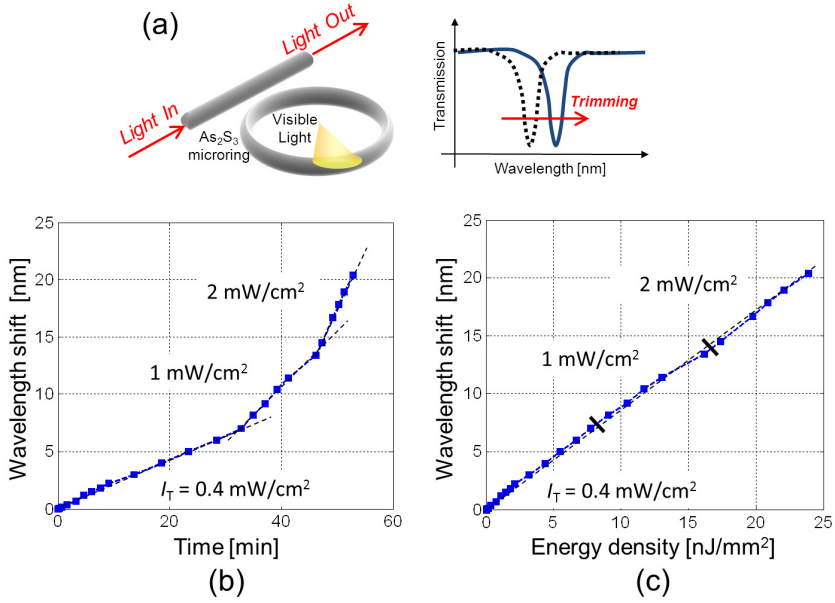

Figure 2.5: *(a) Schematic view of an As_2S_3 microring resonator exposed to near band-gap visible light to trim its resonant wavelength. Photo-induced shift of the resonant wavelength of As_2S_3 microrings versus (a) exposure time and (b) energy density at increasing trimming intensity I_T = 0.4, 1, 2 mW/cm^2.*

$3.2{\cdot}10^{-3}$. Also, by further trimming the waveguide forming the other arm of the MZI (so far kept in the dark), it is possible to restore the initial periodicity of the device, thus demonstrating a complete reconfigurability of the interferometer, and pushing toward a concept of programmable PICs.

Also, the performance of the photo-induced trimming technique was investigated in terms of maximum refractive index change and photo-writing speed. To this aim, microring resonators were fabricated, with 100 μm bending radius and 350×200 μm^2 footprint, providing a free spectral range FSR = 130 GHz (i.e. 1.04 nm). The directional coupler has a length of 150 μm with a gap distance of 700 nm from the bus waveguide to the resonator. As shown in Fig 2.5, resonant wavelength shifts as large as 20 nm were achieved in As_2S_3 microrings, corresponding to about 20 FSRs and an effective index change of $3.2{\cdot}10^{-2}$. This means that the refractive index of the ChG core can be varied through exposure to visible light by at least $\Delta n_{As_2S_3} = 4{\cdot}10^{-2}$. Up to this shift, no saturation effects were observed. Figures 2.5(a) and 2.5(b) point out that the speed of the wavelength shift linearly increases with the trimming light intensity I_T, while the total shift

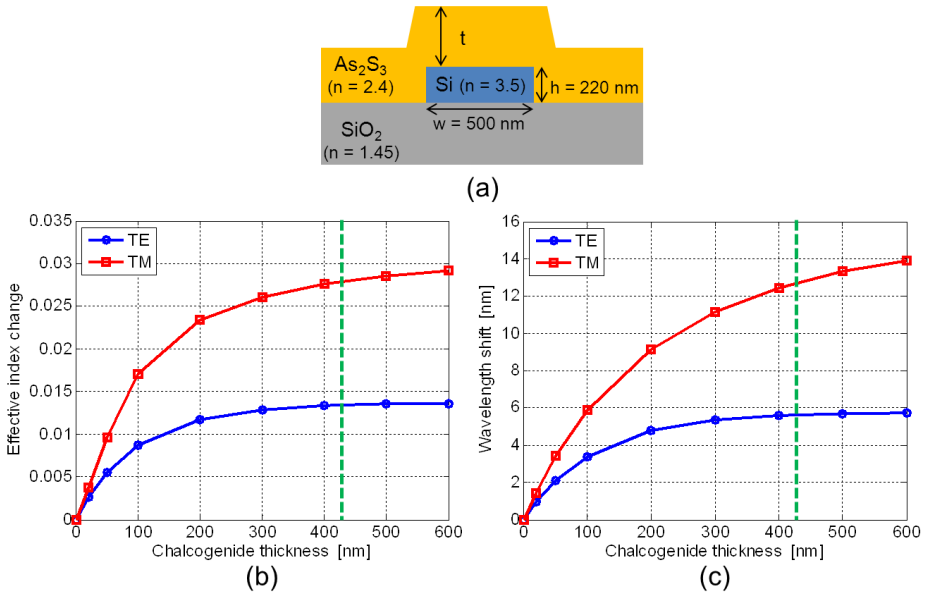

Figure 2.6: *ChG-assisted silicon waveguides: (a) schematic view of the waveguide cross section; (b)-(c) numerical simulations of the effects of ChG photosensitivity (for $\Delta n_{As_2S_3} = 4 \cdot 10^{-2}$): (b) effective index variation and (c) corresponding wavelength shift versus ChG thickness t, for TE (blue circles) and TM (red squares) polarizations. Green dashed line corresponds to the value selected for device fabrication ($t = 420$ nm).*

depends only on the energy density. A resonance shift velocity of 1 nm/min needs only I_T = 2 mW/cm^2 and less than 25 nJ/μm^2 energy density is required to cover a shift wider than 20 nm.

2.2.2 As_2S_3 chalcogenide assisted silicon waveguide

As_2S_3 glass is used here to realize ChG-assisted silicon waveguides with a cross section that is depicted schematically in Fig. 2.6(a). A typical SOI single-mode channel waveguide, optimized for TE polarization propagation, with height h = 220 nm and width w = 500 nm [11], is covered by an upper cladding layer of As_2S_3, with refractive index $n_{As_2S_3}$ = 2.4 at the wavelength 1550 nm. A photo-induced refractive index change of the As_2S_3 cladding results in a permanent variation of the effective index Δn_{eff} of the waveguide modes, making the optical properties of silicon structures easily trimmable. Moreover this Δn_{eff} produces, in any interferometric device, a wavelength shift of the transfer function equal to $\Delta\lambda = \lambda_0 \Delta n_{eff}/n_g$, where λ_0 is the central wavelength and n_g is the group

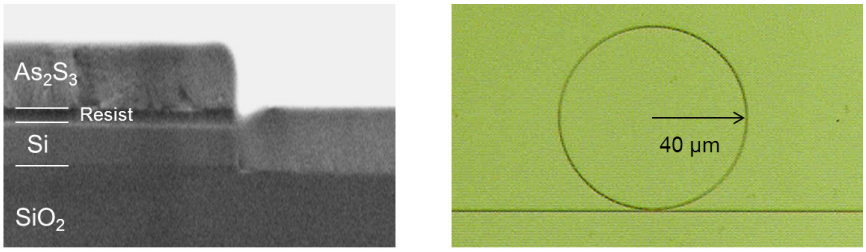

Figure 2.7: *Photomicrographs of the fabricated ChG-assisted silicon devices: (a) SEM image of the waveguide cross section; (b) optical microscope top-view of a microring resonator.*

refractive index.

The effects of ChG photosensitivity on the waveguide propagation have been investigated through numerical electromagnetic simulations, assuming a $\Delta n_{As_2S_3}$ equal to $4{\cdot}10^{-2}$ (see Sec. 2.2.1). Figures 2.6(b) and (c) show, respectively, the behavior of Δn_{eff} and $\Delta\lambda$ as a function of the ChG cladding thickness t, for both TE (blue circles) and TM (red squares) polarizations.

Even a thin layer of ChG is able to provide a large trimmability of the circuits: for TE mode, for example, $t = 20$ nm enables a $\Delta\lambda$ as large as 1 nm, i.e. 125 GHz. For $t > 400$ nm, the effects of photosensitivity become poorly dependent on t. Figure 2.6 also shows that, given the same index change of ChG cladding, the TM-polarized fundamental mode of the waveguide is twice as sensitive as the TE-polarized fundamental mode, because of its weaker confinement factor. Therefore, depending on the specific application, the optimum polarization can be used to maximize either the trimmability of the circuits or the bandwidth and compactness of the devices.

In agreement with these considerations, ChG-assisted silicon waveguides were fabricated at MIT with an optimum As_2S_3 thickness value of t = 420 nm (green dashed line in Fig. 2.6(b) and (c)), from which a waveguide sensitivity of $\partial n_{eff}/\partial n_{As_2S_3}$ = 0.33 is expected, resulting in Δn_{eff} = $1.3{\cdot}10^{-2}$ and $\Delta\lambda$ = 5.6 nm (i.e. 700 GHz). The silicon core waveguide was patterned through electron-beam lithography and inductively coupled plasma reactive ion etching, according to the process described in [11]. In order to improve the fiber-to-waveguide coupling efficiency, the waveguide is widened up to 5 μm approaching the chip end-facets. The As_2S_3 glass cladding layer was thermally evaporated on top of the waveguide according

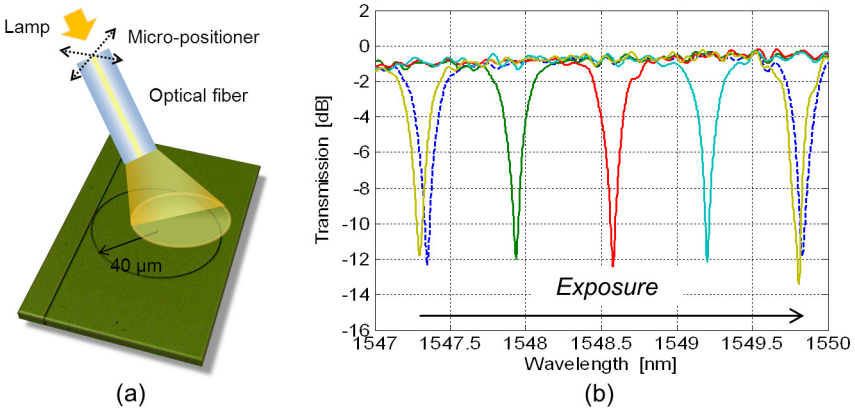

Figure 2.8: *(a) Schematic view of the trimming process of a ChG-assisted SOI microring. (b) Experimental spectral response of the microring: progressive photoinduced red-shift from the as-fabricated condition (blue dashed line) to 1 FSR shift (brown line).*

to the process described in [61]. Figure 2.7(a) reports an SEM (Scanning Electron Microscope) photomicrograph of the realized waveguide cross-section at the chip end-facet, showing good uniformity and conformity of the deposition process. The 70-nm-thick layer between the silicon core and the ChG upper cladding is the hydrogen silsesquioxane (HSQ) resist used for e-beam lithography, that is not removed, since it does not significantly affect the waveguide properties.

2.2.3 Trimming of a silicon microring resonator

The trimmability of ChG-assisted silicon waveguides and circuits and the performance of the trimming technique were experimentally investigated by observing the photo-induced resonance frequency shift of a resonator. The waveguide and the fabrication process described above were used to realize the microring depicted in the top view photomicrograph of Fig. 2.7(b) and 2.8(a). The filter has a coupling gap between the ring and the bus waveguide of 300 nm, a bending radius of 40 μm and a FSR of 2.48 nm (310 GHz). Both the ring and the coupled bus waveguide are covered with 420 nm of As_2S_3 and, after fabrication, the device was stored in the dark in order to avoid any spurious light exposure. The experimental spectral response of the as-fabricated ring resonator (for a TE-polarized input light) is reported in blue dashed line in Fig. 2.8(b), showing good filtering performance, with a -3 dB stop-band of 19 GHz (0.15 nm) and an extinction ratio of 11 dB.

In order to modify the transfer function of the resonator, we locally and selectively trim the n_{eff} of the waveguide forming the ring, by using a visible-light source and an optical fiber, as described in Sec. 2.2.1 [Fig. 2.8]. The experimental results reported in Fig. 2.8(b) show that light exposure is responsible for a progressive red shift of the frequency response of the ring over a whole FSR (solid lines, from green to brown). In this case, the whole waveguide forming the ring is uniformly exposed, except the coupling region to avoid coupling coefficient variations. The wavelength shift is rigid, with neither appreciable changes in the depth nor in the width of the resonant notch, thus demonstrating the lack of additional losses induced by the trimming process and the ability to avoid the exposure of the coupler.

These achievements therefore demonstrate the twofold appealing property of ChG-assisted SOI waveguides: besides enabling easy counteraction of the technological tolerances of the SOI platform and restoration of the desired response of the devices, they also open the way to the realization of PICs that can be reconfigured after fabrication (see also Sec. 6.1-6.2).

2.2.4 Performance of the trimming technique

Once demonstrated the capability to finely trim the optical properties of ChG-assisted SOI devices, the performance of the trimming technique in terms of maximum achievable index change, saturation effects, speed and temporal stability was investigated.

The measured wavelength shift $\Delta\lambda$ of the ring resonance is reported in Fig. 2.9(a) versus the exposure time, when the intensity of the visible light at the fiber output is I_T = 1 mW/cm^2. The experimental (blue circles) and interpolated curves (red dashed line) show that the material photosensitivity moves toward saturation, enabling a maximum achievable $\Delta\lambda$ as large as 6.7 nm (i.e. about 2.5 times the FSR of the ring resonator). This corresponds to an average effective index change of Δn_{eff} = $1.6{\cdot}10^{-2}$, due to an estimated refractive index variation of the ChG cladding of $\Delta n_{As_2S_3} = 4.8{\cdot}10^{-2}$. These values are in good agreement with the simulations reported in Fig. 2.6, based on the experimental results on ChG-core PICs reported in Sec. 2.2.1.

At I_T = 1 mW/cm^2 the time constant of the whole trimming process, measured from 10% to 90% of the maximum $\Delta\lambda$, is about 400 minutes, while the trimming velocity in the linear region of the curve is about 65 pm/min, i.e. 8 GHz/min. Figures 2.9(b) and (c) compare the results of Fig. 2.9(a) (red dashed line) with the $\Delta\lambda$ measured over a nominally identical

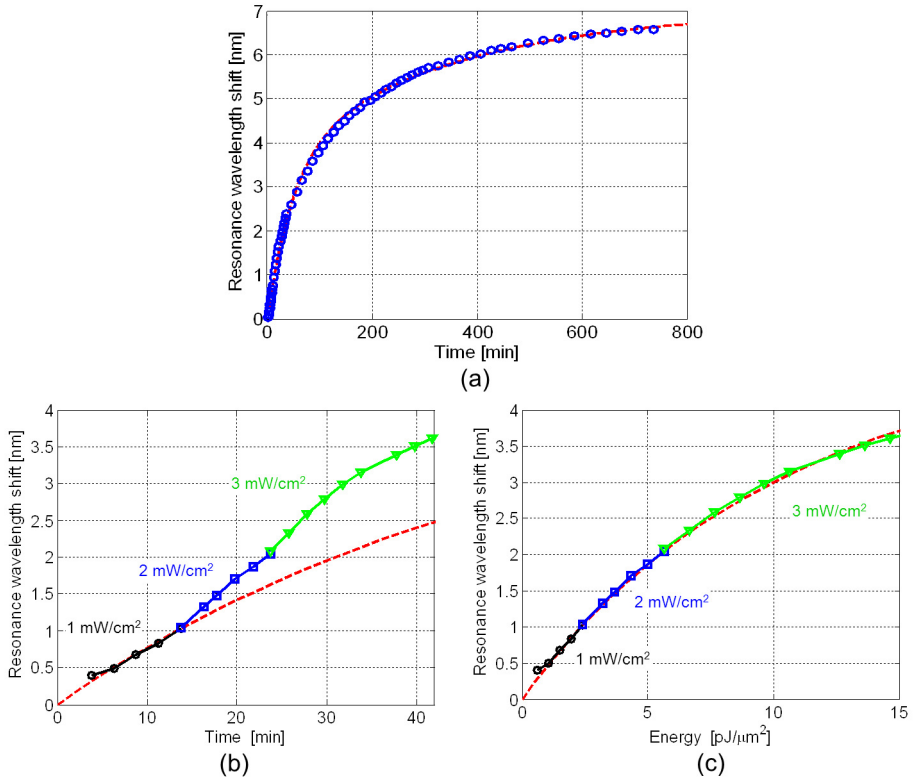

Figure 2.9: *Experimental behavior of the photo-induced resonance wavelength shift of ChG-assisted SOI micro-rings: (a) versus exposure time, when I_T = 1 mW/cm^2 (blue circles); (b) versus exposure time and (c) exposure energy density, for different values of I_T: 1 mW/cm^2 (black circles), 2 mW/cm^2 (blue squares) and 3 mW/cm^2 (green triangles). Red dashed line is the interpolating curve of the experimental data in (a), reported for comparison also in (b) and (c).*

ring resonator (solid lines with markers), exposed to three different values of light intensity I_T: 1 mW/cm^2 (black circles), 2 mW/cm^2 (blue squares) and 3 mW/cm^2 (green triangles).

These experimental results show that the velocity of the trimming process scales linearly with the intensity of the incident visible light [Fig. 2.9(b)], since the photo-induced wavelength shift is proportional only to the exposure energy density [Fig. 2.9(c)]. In particular, in the unsaturated region, the resonant wavelength moves with a velocity of about 65·I$_T$ pm/min (I_T being the light intensity in mW/cm^2 units), producing a wavelength shift $\Delta\lambda \approx 330 \cdot E_T$ pm (E_T being the light energy density in pJ/μm^2 units). This means that a wavelength shift of the microring resonance over

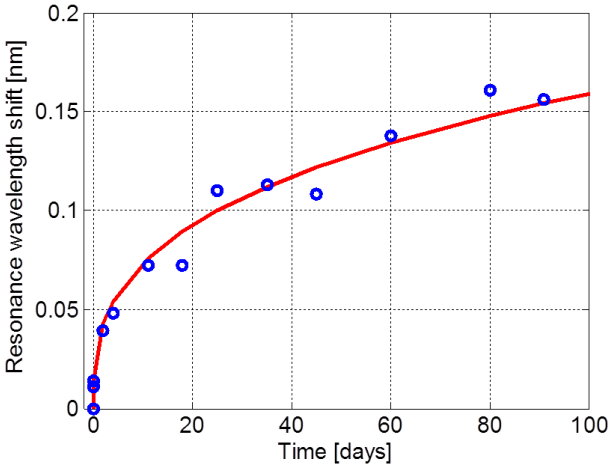

Figure 2.10: *Time stability of the trimming process of a ChG-assisted SOI ring resonator, when the device is stored in the dark after light exposure: measured (blue circles) resonance wavelength shift and power-law fitting curve (red solid line).*

an entire FSR, i.e., a complete trimming or reconfiguration of the device transfer function, is achieved in about 40 minutes at I_T = 1 mW/cm^2, but requires only 1 minute if a moderately low intensity of I_T = 40 mW/cm^2 is used, reaching a tuning speed of 5.2 GHz/s. In both cases it requires an energy density of only 7.4 pJ/μm^2.

To check the temporal stability of the trimming process, the device described above was stored in dark for 91 days after light exposure and periodically measured keeping the sample at the constant temperature of 25°C by means of a thermoelectric cooler. Experimental results (blue circles) in Fig. 2.10 reveal a small red-shift of 0.16 nm of the resonant wavelength, corresponding to only 2% of the wavelength shift induced by visible-light trimming. This wavelength drift is due to the structural relaxation experienced by ChG materials after exposure to light at photon energy above the band gap [62, 63]. Its temporal evolution is consistent with a power-law description (red curve in Fig. 2.10), that is commonly used in literature to model the drift of the electrical parameters of ChG materials [64].

Regarding the magnitude of the wavelength drift, experimental results suggest that it depends on the overall induced wavelength shift. This means that a wavelength shift lower than a FSR (2.4 nm in the described device) would be followed by a drift significantly lower than 0.16 nm, which would be tolerable with respect to the bandwidth of the device. This perception is confirmed by previous results obtained on ChG core waveguides [65]: in

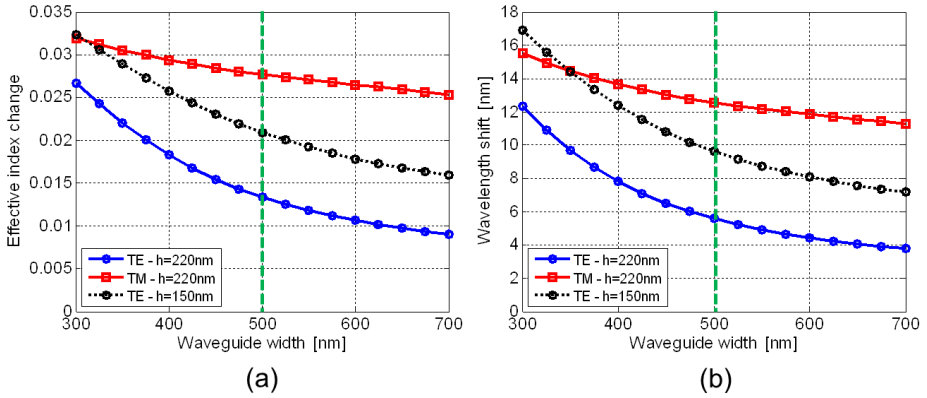

Figure 2.11: *Numerical simulations of the effects of photosensitivity on ChG-assisted SOI waveguides (ChG thickness $t = 420$ nm, $\Delta n_{As_2S_3} = 4 \cdot 10^{-2}$), versus the width w and height h of the core: (a) effective index variation and (b) corresponding wavelength shift, when $h = 220$ nm (solid lines), for TE (blue circles) and TM (red squares) polarizations, and when $h = 150$ nm (solid lines), for TE (black circles) polarization. Green dashed line corresponds to the value $w = 500$ nm.*

that experiment the resonant wavelength of a ring resonator was trimmed by 0.35 nm to restore the spectral response of a two-ring filter, and a negligible wavelength drift was observed compared to 0.26 nm bandwidth (32.5 GHz) of the filter. To better clarify the relationship between the induced wavelength shift and the subsequent drift, an extensive investigation is ongoing and results will be reported in future contributions.

2.2.5 Waveguide optimization

The trimming performance reported in the previous section refers to the TE-polarized fundamental mode of standard SOI channel waveguides covered by As_2S_3 cladding. According to numerical simulations of Fig. 2.11, the maximum effective index change, the corresponding achievable wavelength shift, and the trimming velocity are all expected to double for the TM-polarized fundamental mode of the same waveguides. To further speed up the trimming process and to improve its performance, the waveguide design can be engineered to maximize its sensitivity to light exposure.

To this aim, the effects of photosensitivity on ChG-assisted SOI circuits were numerically investigated as a function of the waveguide dimensions. Figures 2.11(a) and (b) show, respectively, the behavior of Δn_{eff} and $\Delta\lambda$ versus the core width w, assuming a ChG thickness $t = 420$ nm, as in the fabricated waveguides, and $\Delta n_{As_2S_3} = 4 \cdot 10^{-2}$, as in previous simulations

reported in Fig. 2.6. Since different silicon waveguide cross-sections with thinner core layer were recently proposed and successfully applied [44,66], we also investigated two different values of core height: $h = 220$ nm (solid lines), as in the realized waveguides, for both TE (blue circles) and TM (red squares) polarizations, and $h = 150$ nm (dashed line), for TE (black circles) polarization.

From Fig. 2.11 we observe that, for decreasing values of w, the waveguide photosensitivity increases for both polarizations and for both silicon thicknesses. In particular, for $h = 220$ nm, when waveguide width is narrowed from 500 nm (green dashed lines, corresponding to the fabricated waveguides) to 300 nm, the photosensitivity of the TE mode is more than doubled, the Δn_{eff} rising from 0.13 to 0.27 and the $\Delta\lambda$ from 5.7 nm to 12.5 nm. This behavior is expected: by decreasing w, the fundamental mode becomes less confined and therefore the same amount of ChG cladding refractive index change is able to produce a larger variation of the mode effective index, thus increasing the photosensitivity. However, narrowing the waveguide width also modifies the mode propagation properties and can significantly change the circuit performance. Firstly, the lower confinement factor increases the minimum achievable bending radius and imposes devices with larger footprint and smaller FSR. Secondly, the stronger interaction of the mode with waveguide sidewalls produces, in high-index contrast technology and mainly in SOI, a remarkable increase of roughness-induced propagation losses and backscattering effects [45]. In contrast, when w is increased above 500 nm, the waveguide loss figure improves, but the photosensitivity decreases and light propagation moves toward multi-mode regime.

Similar considerations hold even when the variation of the silicon core thickness h is analyzed: as h decreases from 220 nm (blue solid line) to 150 nm (black dashed line), the confinement factor worsens and the waveguide photosensitivity improves, but the mode propagation properties change significantly. Assuming, for instance, a waveguide with width w = 500 nm (green dashed line), both Δn_{eff} and $\Delta\lambda$ of the TE mode increase by a factor 1.6.

This study proves the general validity and flexibility of the proposed approach, enabling to obtain efficiently trimmable circuits from any kind of silicon waveguide structure. The engineering of ChG-assisted waveguides has then to be optimized according to the requirements of each specific application, in order to find the best trade-off between the trimmability of the circuit and its performance in terms of insertion losses, bandwidth, single-mode propagation, and footprint.

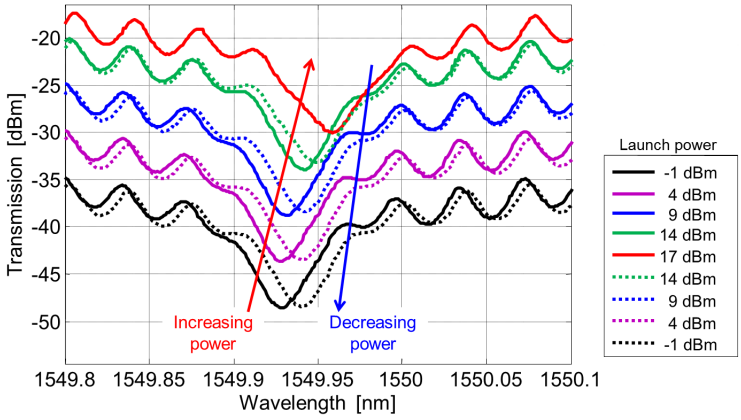

Figure 2.12: *Spectral response of the ring resonator measured with a pump-probe experimental setup with the launch optical pump power that increases from -1 dBm to 17 dBm (solid lines, red arrow) and then decreases down to -1 dBm (dotted lines, blue arrow).*

2.2.6 Nonlinear behavior and IR writing

Finally, we investigate the properties of the As_2S_3-assisted Si waveguides at high optical power. As is well known, when the propagating optical power increases, two photon absorption (TPA) and free carrier dispersion (FCD) effects arise in a Si platform [67]. These non linear phenomena are responsible for both propagation loss increase and refractive index change, that are power dependent and can significantly affect device response and performance [43].

It was recently demonstrated that ChG-based PICs exhibit a certain degree of photosensitivity also to infrared (IR) radiation (1550 nm wavelength), when optical power density in the waveguide exceeds the threshold of 0.1 GW/cm^2 [68]. This is confirmed also for these ChG-assisted silicon waveguides.

The spectral response of a ChG-assisted SOI ring resonator was measured with a pump-probe experimental setup (Fig. 2.12) with the launch optical pump power that increases from -1 dBm to 17 dBm (solid lines, red arrow) and then decreases down to -1 dBm again (dotted lines, blue arrow).

Due to the build-up factor of the resonator, that is about 16, the pump power propagating inside of the cavity is correspondingly increased up to about 250 mW (taking into account also coupling losses), enhancing therefore all the non linear effects.

The resonance wavelength shift of the ring notch is reported in Fig. 2.13

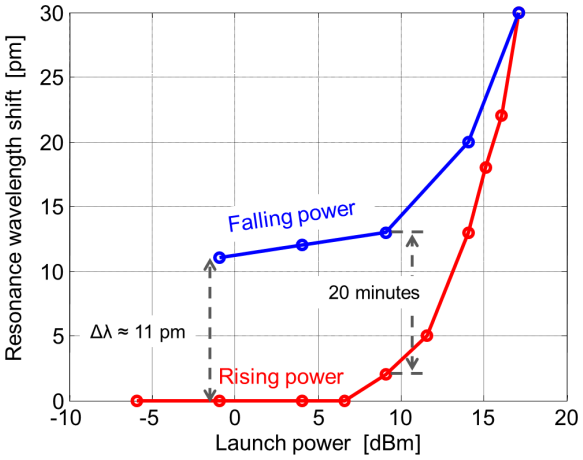

Figure 2.13: *Resonance wavelength shift of the ring notch versus the rising (red line) and decreasing (blue line) value of the launch optical pump power.*

versus the rising (red line) and decreasing (blue line) value of the launch optical pump power.

As expected, two effects can be observed. First, the FCD-induced refractive index change in the silicon core produces a maximum non linear red shift of about 30 pm; this effect is completely reversible and disappears when the pump power decreases down to the linear regime. This behavior is in good agreement with previous results on SOI ring resonators [43], demonstrating that the ChG cladding does not remarkably modify the TPA and FCD induced effects on silicon waveguides. Second, the IR-photosensitivity of the ChG cladding produces a red shift of about 11 pm: this effect is the result of an exposure of about 20 minutes to a 1550 nm wavelength radiation with power above 10 dBm. This effect is permanent and the wavelength shift is maintained also when the optical pump power is decreased down to the linear regime.

CHAPTER 3

Non-invasive light observation

Indeed, low-power actuators and post-fabrication trimming techniques are fundamental tools to recover and steer the circuit to the desired working point. However, circuit monitoring and feedback control operations are required as well to counteract the effect of fabrication tolerances, environmental fluctuations, and mutual cross-talk [51, 69] (see Sec. 5.2 for details and for experimental demonstration of feedback control), especially when many photonic devices are aggregated into complex circuits. To this aim, the current status of each part of the circuit needs to be inspected real-time without altering its working point. As long as the components count in a circuit is limited to a few units, light monitoring can be achieved by tapping a small fraction of the optical power from the waveguide [13, 25, 26, 29, 70] and rerouting it to a photodetector [14, 15]. Yet, when hundreds or thousands of devices are integrated, the number of probing points increases accordingly, and any light attenuation or perturbation should be avoided [6, 7, 31].

Light tapping from the waveguide can be circumvented by using the waveguide itself as a power monitor. In silicon waveguides, where material absorption is inhibited at wavelengths above 1.1 μm, photocarrier generation has been demonstrated by exploiting two photon absorption (TPA)

[71, 72], and sub-bandgap absorption mechanisms, including surface-state absorption (SSA) [73, 74] and defect mediated absorption induced via selective ion-implantation [75, 76]. However, power monitors proposed so far based on these effects require the waveguide core to be electrically contacted through highly doped regions [74–76] or electric lines [73] to sweep out carriers from the absorbing region. This leads to additional optical loss that limits the number of probing points to a few units. The development of minimally-invasive waveguide power monitors still presents one of the key challenges for integrated optical technology [31].

Here, non-invasive light observation is demonstrated in silicon photonics devices by exploiting photon interaction with intra-gap energy states localized at the waveguide surface. The physical effect exploited in this technique is the change of the waveguide conductance induced by native interaction of photons with the intra-gap energy states localized at the Si-SiO_2 interface [77] that exist even in an ideal roughness-free interface [78]. Unlike other techniques, a capacitive access to the waveguide is used, thereby avoiding direct contact with the waveguide core, and no specific treatments at the waveguide surface need to be done. Neither photon tapping is required nor appreciable perturbation on the optical field is introduced, thereby implementing a truly non-invasive light observation.

The concept of the non-invasive light observer, that is the ContactLess Integrated Photonic Probe (CLIPP), is presented in Sec. 3.1, with details on its fabrication and technology in Sec. 3.2. Experimental results, including measurement setup and light monitoring in silicon waveguides and resonators, are shown in Sec. 3.3. An in-depth analysis of the non-perturbative nature of the CLIPP is presented in Sec. 3.4, whereas Sec. 3.5 focuses on the electronic system utilized to read the CLIPP. Furthermore, results of extensive and systematic characterization of the CLIPP, including the dependence on waveguide geometry, polarization and wavelength, as well as issues like speed and sensitivity, parasitism, and size, are presented in Sec. 3.6. Finally, the Chapter ends with some information on the extension of the CLIPP concept to semiconductor technologies other than silicon, such as indium phosphide (Sec. 3.7).

3.1 The CLIPP concept

The CLIPP concept is represented in the schematic of Fig. 3.1(a). The CLIPP consists simply of two metal electrodes surrounding the optical waveguide structure and spaced from the silicon core by an electrically insulating layer. In the configuration of Fig. 3.1(a), both electrodes are lo-

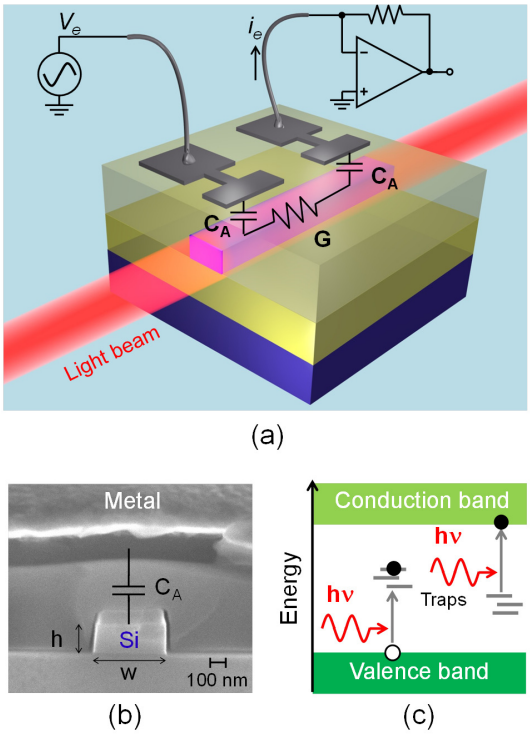

Figure 3.1: *Non-invasive light observation on a silicon chip. (a) Schematic view of the CLIPP, consisting of two metal electrodes deposited onto the electrically-insulating upper cladding and capacitively coupled (C_A) to the electrically-conductive (G) Si waveguide. (b) Scanning electron microscope (SEM) photograph of the Si waveguide cross-section (w = 480 nm and h = 220 nm). (c) Schematic representation of surface-state-absorption process (SSA), where intra-gap energy states create a free carrier and a corresponding recombination center.*

cated above the waveguide on top of the upper cladding layer. A Si channel waveguide with a rectangular core region is here considered, but the CLIPP can be applied to arbitrary waveguide geometries, such as shallow and deep etched rib, slot, or photonic crystal waveguides.

The operation principle of the CLIPP can be explained by considering the behavior of the Si waveguide in the electrical domain. Because of the typical doping level of commercial SOI wafers (10^{15} cm^{-3}, p-type), the Si core acts mainly as a conductive wire, with conductance $G = \sigma wh/L$ that depends on the width w and the height h of the Si core, on the length L of the considered waveguide section (that is the distance between the metal contacts), and on the electrical conductivity σ of Si. The latter is related essentially to the average number of free carriers locally contained in the

Si layer. For instance, in the waveguide shown in Fig. 3.1(b), with w = 480 and h = 220 nm, about 10^2 free holes are distributed in the volume of a 1-μm-long waveguide section, thus providing a conductance of about 8 nS for a 100 μm-long waveguide.

As light propagates in the waveguide, additional free carriers are generated by surface-state-absorption (SSA) mechanisms [see Fig. 3.1(c)], that locally modify the waveguide conductivity, and hence the overall electric conductance G. (Chapter 4 of this thesis is entirely dedicated to the identification of SSA as the physical phenomenon responsible for the operation of the CLIPP and to the observation of its effects on Si photonic waveguides). Therefore, a measurement of the light dependent change of the waveguide conductance ΔG provides direct information on the light intensity in the waveguide.

In order to implement a truly non-invasive light observation, the CLIPP exploits a capacitive access to the waveguide, thereby avoiding direct contact with the waveguide core. For the channel waveguide of Fig. 3.1(b), the electrodes are spaced from the silicon core by a 1-μm-thick silica film, providing access capacitances C_A to the Si waveguide. At the wavelength of 1550 nm, the optical intensity at the SiO_2-metal interface is 80 dB below its peak value in the waveguide, so that the electrodes do not induce any appreciable change in the waveguide propagation loss, here amounting to about 2 dB/cm.

Neglecting parasitic effects, such as those due to the Si substrate and to the capacitance between the electrodes, that are discussed in details in Sec. 3.6.5, the equivalent electric circuit of the CLIPP consists simply of two access capacitances C_A in series with the waveguide conductance G [Fig. 3.1(a)]. Thus, the light dependent conductance variation ΔG can be inferred from the measurement of the overall electric impedance at the two metal electrodes through an ultra-sensitive impedance measurement system [79]. The experimental setup here utilized is described in Sec. 3.3.1.

3.2 CLIPP fabrication and technology

The silicon waveguides were fabricated by the University of Glasgow on a commercial SOI wafer with a 220-nm thick Si core on a 2 μm thick oxide buffer layer. The waveguide pattern is written on a hydrogen silsesquioxane (HSQ) resist through electron-beam lithography and then transferred to the Si core by an inductively coupled plasma etching process [11]. A residual 80-nm thick HSQ cap layer on top of the waveguide is visible in the SEM picture of Fig. 3.1(b). The waveguide core is buried under a 1-μm thick

cover layer, consisting of 550 nm of spun and baked HSQ and 450 nm of silicon dioxide grown by plasma enhanced chemical vapor deposition (PECVD).

The electrodes of the CLIPP consist of a 200 nm thick Au film deposited onto the silica cladding (with an intermediate 20 nm thick Ti adhesion layer) and patterned by lift-off technique. The CLIPP can be fabricated by using any CMOS compatible metal technology and can exploit conventional processes used for realizing thermal actuators [80], without additional process steps.

Inversely tapered waveguide sections, buried in a SU8 polymer waveguide, were realized at the chip facets in order to reduce the coupling loss with optical lensed fibers (1.7 μm mode field diameter) to 5 dB/facet.

3.3 Experimental results

3.3.1 Experimental setup

The real and imaginary parts of the waveguide impedance are measured through a synchronous detection architecture, including a low-noise transimpedance amplifier coupled to a high precision lock-in demodulator. In order to measure ΔG, a sinusoidal voltage V_e at a frequency f_e is applied to one electrode of the CLIPP, the other being connected to a transimpedance amplifier to collect the flowing current i_e [Fig. 3.1(a)]. The transimpedance amplifier has a 10^4 V/A conversion gain, a bandwidth of 80 MHz, and a 6 pA·Hz$^{-1/2}$ minimum noise floor at 1 Hz integration bandwidth, resulting in a total measured rms noise of about 80 pS. In the perturbation measurement discussed in Sec. 3.4, the output optical signal is detected by an external photodiode and then collected by a second channel of the lock-in detector, thus enabling synchronous detection of the optical and the electrical signals.

The temperature of the optical chip is controlled within 0.1 K by a Peltier thermocooler integrated inside a customized holder. The state of polarization of the input light is controlled with a polarization controller providing an extinction ratio greater than 30 dB between the excited quasi-transverse electric (TE) and quasi-transverse magnetic (TM) modes over a wavelength range of about 20 nm around 1550 nm.

3.3.2 Light induced conductance change

The measured conductance variation ΔG versus the optical power P is shown in Fig. 3.2 for a single mode (w = 480 nm, red circles) and a mul-

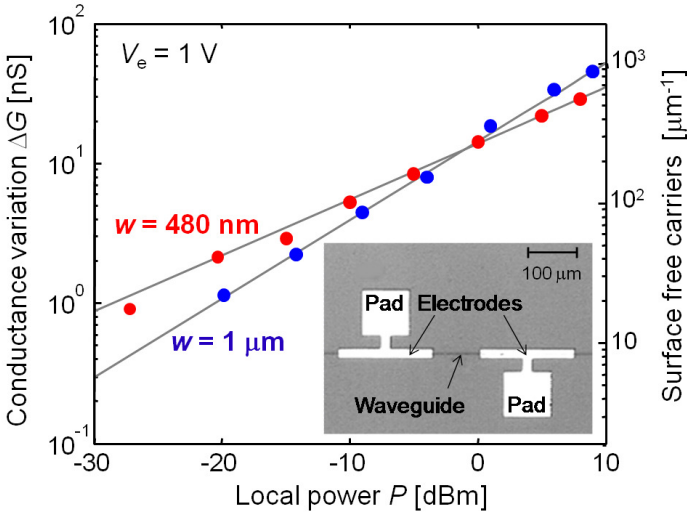

Figure 3.2: *Optical power monitoring performed with a CLIPP. Measured conductance variation ΔG versus the optical power P for a single mode (w = 480 nm, red circles) and a multimode (w = 1 μm, blue circles) silicon waveguide. The CLIPP is driven at V_e = 1 V and f_e = 1 MHz, metal electrodes (20 μm $\times$ 200 μm) are placed at distance L = 100 μm. The 100 μm $\times$ 100 μm metal pads are used for wire bonding with the impedance read-out system.*

timode (w = 1 μm, blue circles) silicon waveguide. Light intensity was observed over a dynamic range of 4 orders of magnitude, down to -30 dBm (1 μW), this performance largely fulfilling the requirements of several practical applications. A response time down to 50 μs was achieved by driving the device with a voltage V_e = 1 V and a frequency f_e = 1 MHz. The inset shows a top-view photograph of the device with a 100-μm-long waveguide section enclosed between two narrow electrodes.

An in-depth analysis was carried out to identify SSA as the physical effect responsible for the change of waveguide conductance ΔG (see Chapter 4). Results show that ΔG is associated with a carrier density variation rather than with a carrier mobility variation, and that TPA-mediated photocarrier generation is negligible. The sensitivity of the CLIPP is related to the density of free carriers generated by SSA, that depends on the intensity of the optical mode on the waveguide boundaries [73], where surface states are located (typically within the first three/four silicon atomic layers [81]).

For the waveguides considered in Fig. 3.2, the integral intensity of the light along the waveguide perimeter is similar, resulting in a comparable conductance variation ΔG for the same power P of the guided mode (see 3.6.1 for details). This small geometrical sensitivity enables application of

the technique without imposing specific constraints to the design of the optical waveguide. A comparable sensitivity on TM polarization was also observed (see 3.6.2 for details). To improve the CLIPP sensitivity, the modal overlap with the surface can be increased by suitably engineering the cross-sectional waveguide geometry [73], yet at the price of a higher propagation loss [45].

The slope of the log-log ΔG-P curves is related to the density of carriers generated at the surface. A sub-linear relationship is observed, that is consistent with a situation in which the number of photo-generated carriers is larger than those thermally available. A similar behavior has been reported also in metal oxide semiconductor (MOS) devices [82] and in high gap conductors [83]. In this regime an increase of the optical power results not only in a larger carrier density but also in a reduction of their recombination time [84]. This condition is verified in both devices of Fig. 3.2, where, at P = -10 dBm ($\Delta G \approx 5$ nS), about 10^2 μm^{-1} free carriers are locally photogenerated at the surface of a 1-μm-long waveguide section, this number being comparable with the density of native free holes distributed across the waveguide in absence of light. For the same value of optical power P, the single mode waveguide (shorter perimeter) has a higher carrier density with respect to the multi-mode waveguide (larger perimeter), resulting in a slightly lower recombination time, and consequently in a small reduction of the ΔG-P exponent (see Sec. 3.6.1 for more details).

The density of free carriers generated by SSA per unit length (Fig. 3.2, right vertical axis) is estimated by assuming that the photogeneration is homogeneous along the waveguide with a density of photogenerated holes equals to the density of photogenerated electrons, $\Delta N_{e,s} = \Delta N_{h,s} = \Delta N_s/2$. Further, the mobility of carriers generated at the surface ($\mu_{e,s}$ = 500 cm^2/V·s and $\mu_{h,s}$ = 150 cm^2/V·s) is about 30% [85] of the free carriers mobility in the bulk. Thus for an area A we obtain:

$$\Delta G = \Delta\sigma \frac{A}{L} = q \left(\frac{\mu_{e,s} + \mu_{h,s}}{2} \right) \frac{A}{L} \Delta N_s \tag{3.1}$$

from which the value of the linear density of surface free carriers plotted in Fig. 3.2 is calculated.

3.3.3 Multi-point light monitoring

Many light monitors can be placed in strategic positions around the chip enabling real time management of complex integrated optical systems. We fabricated a racetrack silicon resonator [see Fig. 3.3(a)] equipped with three

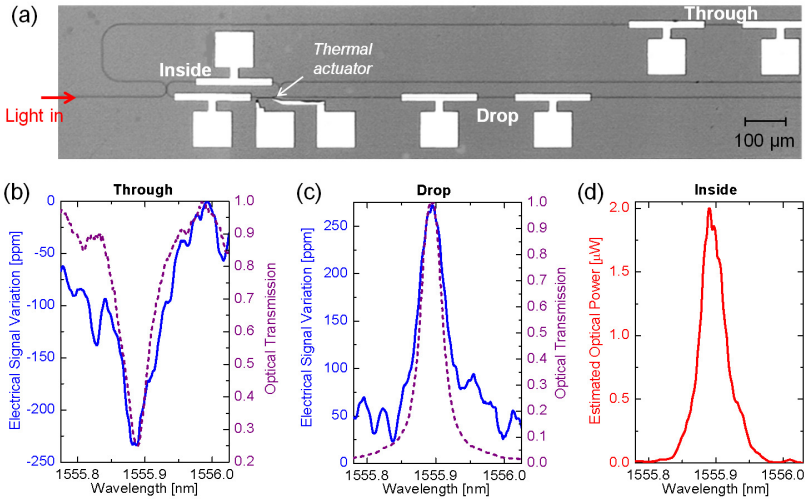

Figure 3.3: *Non-invasive monitoring of a silicon photonic integrated circuit. (a) Top-view optical microscope photograph of a racetrack microresonator with a CLIPP at both the Through and the Drop port bus waveguides, and with an inner CLIPP inside the resonator. The resonator has a radius of 20 µm and a geometric length of 644 µm. (b) Through and (c) Drop port TE transmission measured with an external OSA (purple dashed curves) and with the on-chip CLIPPs (blue solid curves). The amplitude and the frequency of the electric signal driving the CLIPPs are V_e = 1 V and f_e = 2 MHz, respectively. (d) The intracavity optical power around the resonant wavelength is retrieved from the electric signal of the CLIPP inside the resonator.*

CLIPPs: one inside the resonator and the other two at the Through and Drop ports respectively. The same metal technology of the CLIPP is used to realize a thermo-optic actuator [80] inside the resonator (for details on the actuator technology see Sec. 2.1) for the feedback control of its resonant wavelength (Sec. 5.2).

To set a benchmark for performance evaluation, the CLIPPs were first switched OFF (V_e = 0) and the reference transmission spectra of the resonator were measured through a tunable laser with 1 pm resolution, synchronized with an optical spectrum analyzer (OSA). Fig. 3.3(b)-(c) shows in purple dashed lines the transmission of the resonator at the Through and Drop ports, respectively. The measured 3 dB linewidth and free spectral range are 36 pm and 860 pm, respectively, resulting in a Q factor of about 43000. Measurements were repeated with the three CLIPPs switched on at V_e up to 10 V, and no detectable changes of the resonator spectrum and of the intrinsic Q factor (about 55000) were observed.

The transmission spectra of the resonator were then measured by using

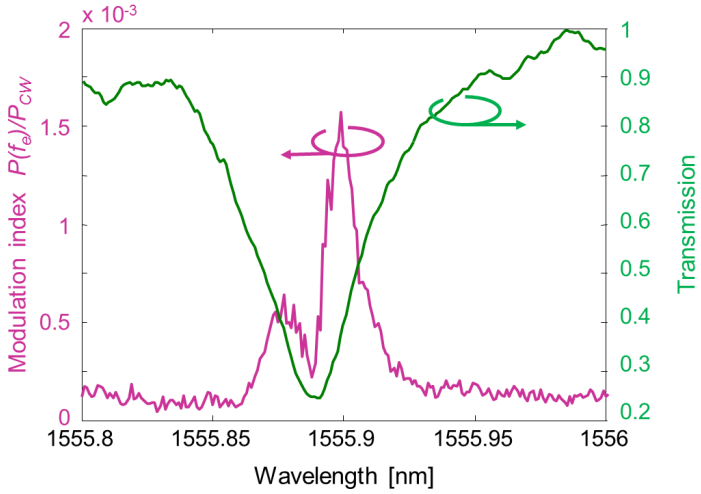

Figure 3.4: *Analysis of the perturbative effects induced by the CLIPP. The purple curve shows the ratio between the perturbation $P(f_e)$, given by the power of the optical signal modulated at the frequency of the electric signal, and the power of the optical signal P_{CW}. The measurement is carried out on the optical signal outgoing from the Through port of the resonator of Fig. 3.3. The asymmetry in the measured perturbation is inherently associated to the non-symmetric transmission spectrum of the resonator (green curve).*

the CLIPPs integrated at the Through [Fig. 3.3(b), blue solid line] and at the Drop [Fig. 3.3(c), blue solid line] ports. The electric signal of the CLIPP provides a direct measurement of the resonance wavelength of the resonator, with less than 1 pm shift compared to the OSA reference. By using the calibration curve of Fig. 2, the spectral line and the optical power level inside the resonator were also retrieved, as shown in Fig. 3.3(d). The -3 dB linewidth, measured at a power level of -30 dBm, is less than 2 pm larger than the OSA measurement, thus demonstrating the accuracy of the CLIPP.

3.4 Perturbation analysis

The non-invasive nature of the CLIPP was explored by looking for the existence of a signal component at the read-out frequency f_e in the output optical signal with a highly sensitive lock-in based detection system (details in 3.5).

As no evidence of disturbance was detected on bare waveguides, we investigated the perturbative effects on high-Q optical microresonators. We

injected a continuous-wave (CW) light into the resonator of Fig. 3.3(a) and measured the ratio between the power $P(f_e)$ at f_e = 2 MHz and the average power P_{CW} of the optical signal outgoing from the Through port, this ratio being typically referred to as modulation index of an intensity modulated signal. The inner CLIPP was driven at V_e = 1 V and the wavelength scanned across 0.2 nm around the resonant wavelength λ_r = 1555.889 nm. As shown in Fig. 3.4 with purple line, the modulation index $P(f_e)/P_{CW}$ is minimum at λ_r, where the slope of the transmission spectrum of the resonator (green line) vanishes, whereas it exhibits local maxima at $\lambda_p = \lambda_r \pm$ 9 pm, where the slope of the spectrum is maximum. This result provides clear evidence that the perturbation is due to a refractive index modulation effect, causing a tiny wavelength shift of the resonator spectrum and an intensity modulation of the output signal [86].

The relative perturbation at the frequency f_e of the electric signal driving the CLIPP can be expressed as

$$\frac{P\left(f_e\right)}{P_{CW}} = \frac{1}{H}\frac{\partial H}{\partial \lambda} d\lambda = \lambda_r \frac{1}{H}\frac{\partial H}{\partial \lambda}\frac{dn_{eff}}{n_g}\frac{L_e}{L_r} \tag{3.2}$$

where H is the intensity transmission spectrum of the ring resonator at the Through port [see Fig. 3.5(a)], $d\lambda$ is the shift of the resonant wavelength λ_r due to the induced perturbation dn_{eff} of the waveguide effective index, and n_g is the waveguide effective group index. The ratio L_e/L_r takes into account that the index perturbation does not occur along the entire ring length L_r, but only in a portion of length L_e underneath the metal electrode where the voltage V_e is applied. For the device of Fig. 3.3(a) driven at a voltage V_e = 1 V, we measured a maximum relative perturbation $P\left(f_e\right)/P_{CW}$ = 1.65·10^{-3} (-27.8 dB) at the wavelength λ_p = 1555.898 nm (where $\partial H/\partial\lambda$ = 30 nm^{-1}) corresponding to a resonance shift $d\lambda$ = 55 fm (6.8 MHz), that is less than 0.1% of the resonator linewidth. The excellent agreement of this model with the experiment is further confirmed in Fig. 3.5(b), where measured (red solid lines) and simulated (black dashed lines) perturbations are plotted for different CLIPP voltages V_e = 0.25, 1, 2 V.

This tiny perturbation is really negligible in most applications. For instance, assuming that a resonant shift of less than 10% of the resonator linewidth is acceptable, then the CLIPP can be used to monitor resonators with a bandwidth as narrow as 50 MHz, that is with a Q factor of about 4·10^6. Hence, the CLIPP can be applied without any disturbance to the Si microring resonators with the highest Q factor realized so far [87], which is in the order of 7.6·10^5.

Furthermore, by substituting in eq. 3.2 the values of the geometric (L_e

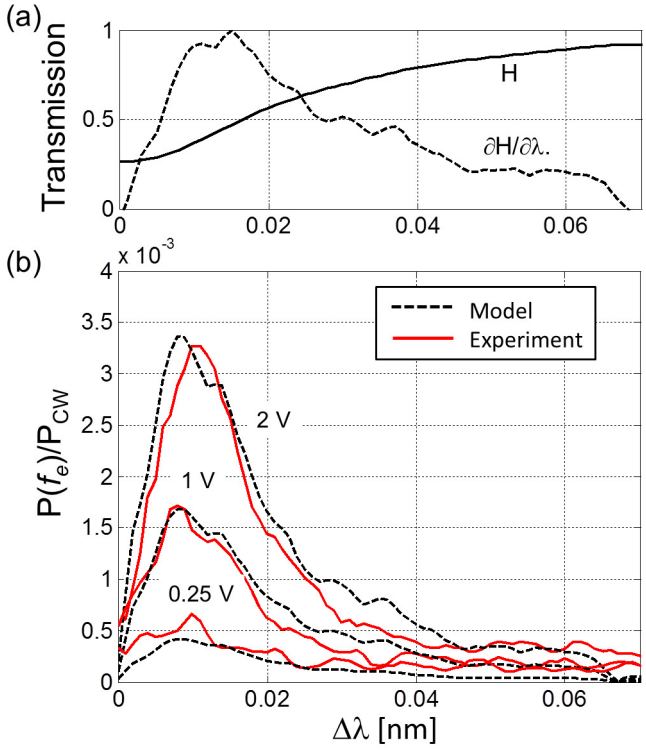

Figure 3.5: *(a) Normalized transmission H of the ring resonator of Fig. 3.3(a) at the Through Port (black solid line) and its normalized derivative function $\partial H/\partial\lambda$ (black dashed line) across half of the linewidth. (b) Measured (red solid lines) and simulated (black dashed lines) perturbation of the optical signal at the read-out frequency f_e normalized to the CW optical signal at the output of the resonator for different CLIPP voltages V_e = 0.25, 1, 2 V.*

= 200 μm, L_r = 644 μm) and optical (n_g = 4.22) parameters of the considered structure, we derived an effective index perturbation dn_{eff} = 5·10^{-7}, amounting to about 0.2 ppm of the waveguide effective index n_{eff} = 2.45, and corresponding to an induced phase modulation of $d\phi = 2\pi dn_{eff}L_e/\lambda_p$ = 0.4 mrad. Also, if assuming a thermo-optic coefficient of 1.84·10^{-3} K^{-1} for the silicon waveguide [88], the induced perturbation is comparable to that induced by a temperature change of 2.7 mK, which is about two orders of magnitude below the thermal stability limit guaranteed by conventional thermo electric coolers and can be considered negligible in practical applications.

Finally, we investigated the physical mechanism originating such a tiny perturbation, by exploring the behavior of the CLIPP up to an applied volt-

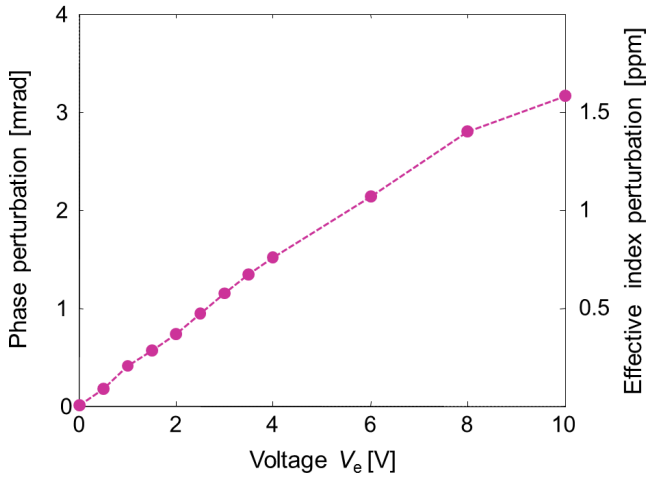

Figure 3.6: *Phase perturbation and effective index perturbation induced by the CLIPP. The typical driving voltage of the CLIPP is around 1 V.*

age of V_e = 10 V. As shown in Fig. 3.6, the linearity of the measured perturbation versus V_e rules out the existence of a significant thermal heating of the waveguide due to a current flow along the silicon core, which would rather exhibit a quadratic behavior versus V_e. Results are instead consistent with a linear electro-optic Pockels effect, according to which the refractive index variation dn of the silicon core is related to the applied electric field E by

$$dn = \frac{n^3}{2} r E = \frac{\chi^{(2)}}{n} E \tag{3.3}$$

where $\chi^{(2)}$ is the second-order susceptibility. In our experiment, the change of the waveguide effective index dn_{eff} corresponds to $dn = 7{\cdot}10^{-7}$ (at V_e = 1 V) and the average electric field in the 3-μm-thick silica layer underneath the electrode is E = 0.3 V/μm. These values lead to an electro-optic coefficient r = 0.1 pm/V ($\chi^{(2)}$ = 5 pm/V) that is consistent with other reports of non-intentionally strained silicon waveguides [89].

3.5 Electric impedance read-out system

In this section, further details are provided on the electric model of the CLIPP, on the read-out system employed for the measurement of the electric impedance, and on the optimization of the CLIPP design.

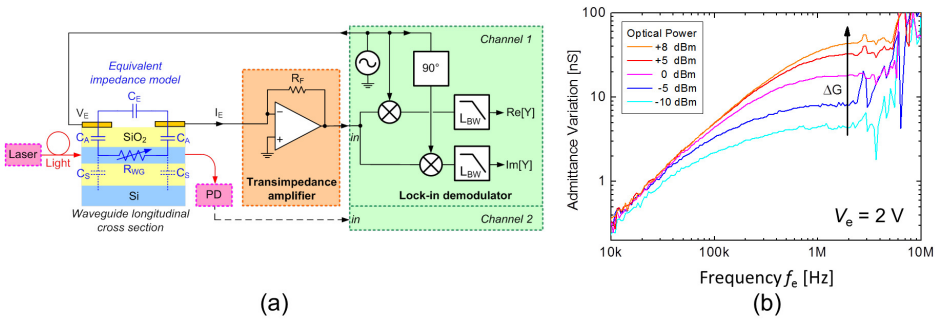

Figure 3.7: *(a) Scheme of the electric impedance read-out system, consisting of a low-noise transimpedance amplifier (with feedback resistance R_F) combined with a precision lock-in detector with bandwidth L_{BW}. The equivalent impedance model of the CLIPP is also shown. (b) Measured differential admittance spectra (with respect to the absence of light) for waveguide power ranging from -10 dBm to 8 dBm.*

Figure 3.7(a) shows a scheme of the read-out system and the electric equivalent model of the CLIPP. The access capacitance C_A to the waveguide can be evaluated (neglecting fringing field effects) as a parallel plate capacitor $C_A = \varepsilon_0 \varepsilon_{ox} wd/t_{ox}$, where t_{ox} and ε_{ox} are the thickness and relative dielectric constant of the SiO_2 upper cladding layer, respectively, ε_0 is the vacuum permittivity, and d the length of the metal electrodes. Similarly, the nominal value of the waveguide resistance in absence of light is $R_{WG} = 1/G = \sigma^{-1} L/wh$ where $\sigma^{-1} \sim 1$ MΩ/μm is the bulk resistivity of the waveguide. In parallel to the main C_A-R_{WG} path, a parasitic capacitance C_E is generated by the stray coupling between the electrodes (measured in the 0.16-0.8 pF range depending on the geometry of the CLIPP electrodes and on the connection wires arrangement). Since in the MHz range the impedance associated to C_E is about 3 orders of magnitude smaller than that of R_{WG}, a lock-in system with 100 ppm resolution is required.

Fig. 3.7(b) shows the variation of the absolute value of the admittance Y measured at the CLIPP electrodes. The change of waveguide conductance ΔG can be extracted by subtracting the reference spectrum of the waveguide admittance (measured in absence of light) from the admittance spectra measured at different optical power levels P. The increase of the plateau level (around 1 MHz in the figure) provides information on ΔG. The spectral position of this plateau is set by the frequency $f_A = 1/(2\pi R_{WG} C_A/2)$ of the pole associated with C_A.

Once w, h, and t_{ox} are fixed according to waveguide optimization criteria, the frequency f_A of the CLIPP can be conveniently adjusted by a suitable choice of the electrodes distance L and of the electrode length d.

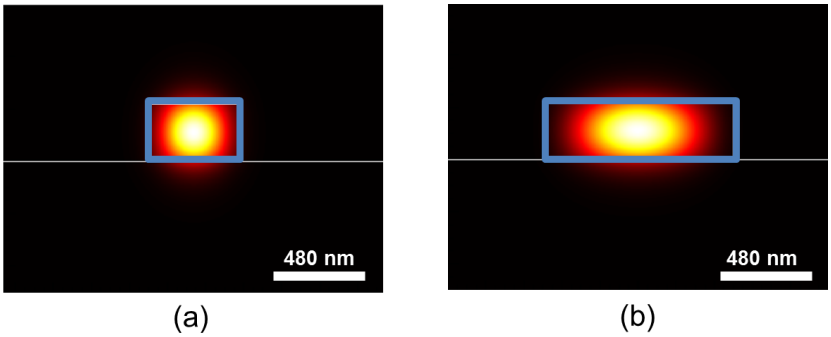

Figure 3.8: *Intensity of the fundamental TE mode of Si waveguides with width (a) w = 480 nm and (b) w = 1 μm simulated via Film-Mode-Matching (FMM) method. The blue solid line highlights the boundary of the waveguides where surface states are located. Both figures have the same horizontal and vertical scale.*

In our case, where L = 100 μm ($C_A \sim$ 5 fF) and d = 200 μm, the resulting f_A is about 1 MHz.

Miniaturization of the CLIPP is possible, yet at the price of a higher f_e, since f_A shifts at higher frequencies when L or d are reduced (see Section 3.6.6). However, a physical upper limit to f_e is set also by the presence of the stray capacitances C_S between the waveguide core and the silicon substrate through the bottom oxide. In fact, this distributed capacitance attenuates the applied electrical signal due to the high frequency partition between C_A and C_S .

In principle, the operative frequency f_e depends also on the thickness t_{ox} of the upper cladding oxide. However, standard deposition techniques guarantee a control of better than 10 nm in the film thickness. This small tolerance introduces no significant variability in the CLIPP performance, because it only induces a 1% change of f_A and thus of f_e.

3.6 Systematic characterization of the CLIPP

3.6.1 Dependence on waveguide geometry

The sensitivity of the CLIPP is related to the number of free carriers generated by surface state absorption. For a given density of traps, this depends on the intensity of the optical mode on the waveguide boundaries (Si-SiO_2 interface), where surface states are located, typically within the first three/-four Si atomic layers ($\sim$1 nm) [81].

For both waveguides of Fig. 3.2, with w = 480 nm (monomode) and w=

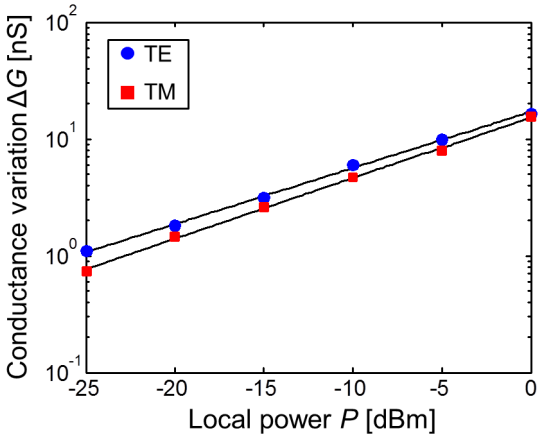

Figure 3.9: *Measured conductance variation ΔG versus the optical power P in a waveguide with width w = 1 μm on both TE polarization (blue circles) and TM polarization (red squares). The CLIPP exhibits a comparable sensitivity to both polarizations, thus indicating its ability to monitor light on TE and TM modes.*

1 μm (multimode), the integral intensity of the light along the waveguide perimeter [marked in blue in Fig. 3.8] is very similar. Therefore, for the same level of total power P of the guided mode, the number of free carriers generated by SSA, and hence the conductance variation ΔG, is comparable. This explains why the CLIPP has a very similar sensitivity in single mode and multimode waveguides, and more generally in all waveguides where the light intensity at the boundary is comparable. In order to improve the CLIPP sensitivity, the modal overlap with the waveguide boundary can be increased by suitably engineering the cross-sectional waveguide geometry [73], yet at the price of a higher propagation loss [45].

The slight difference in the slope of the ΔG-P curves of Fig. 3.2 is due to the slightly different density of carriers generated at the boundary. Since the two waveguides have different perimeters (but the same total intensity at the perimeter), the single mode waveguide (w = 480 nm) has a higher carrier density with respect to the multimode waveguide. A larger carrier density causes a slightly lower recombination time [84], and consequently a reduction of the ΔG-P slope.

3.6.2 Polarization dependence

A similar concept to the case of single mode and multi mode waveguides stands also for polarization dependence: the CLIPP sensitivity to TM po-

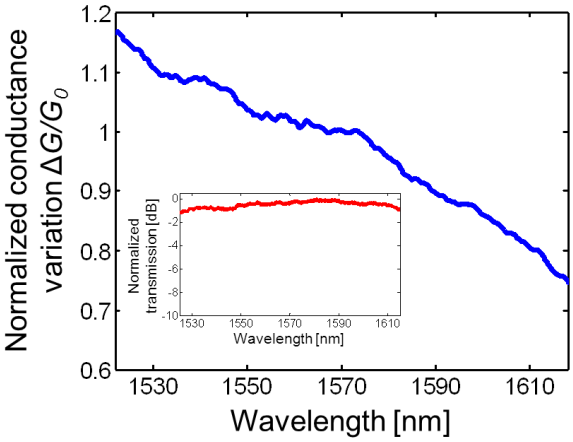

Figure 3.10: *Conductance variation ΔG, measured by the CLIPP as a function of wavelength, normalized to the conductance G_0 measured at the central wavelength 1570 nm (waveguide width 1 μm, TE polarization). The inset shows the normalized transmission of the waveguide across the same wavelength range.*

larized light is related to the overlap of the TM mode with the waveguide boundary.

Experimental results demonstrate that the CLIPP exhibits a comparable sensitivity on TE and TM polarizations, this enabling its application to monitor the light on both polarization states. For example, Fig. 3.9 shows the CLIPP response for a waveguide with width w = 1 μm for TE (blue circles) and TM (red squares) polarization. The CLIPP exhibits a slightly higher sensitivity on TE polarization because the overlap of the TE guided mode with the waveguide boundary is slightly higher than on TM polarization.

3.6.3 Wavelength dependence

The dependence of the CLIPP from wavelength was tested by measuring the variations of conductance ΔG in presence of light as a function of the input wavelength.

Figure 3.10 shows the measured ΔG in the 1520-1620 nm wavelength range normalized to the conductance G_0 measured at 1570 nm on a waveguide with width 1 μm and on TE polarization. Here, ΔG is measured for a waveguide power of about -10 dBm and with a CLIPP driving frequency f_e = 0.91 MHz. This curve represents directly the sensitivity of the CLIPP with wavelength, in fact as shown in the inset of Fig. 3.10 the

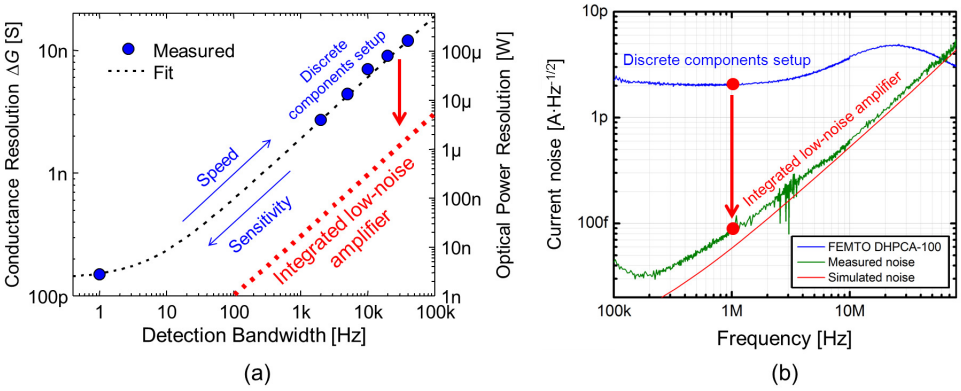

Figure 3.11: *Speed-sensitivity trade-off of the CLIPP. (a) Resolution of the CLIPP (blue solid circles), both in the electrical and optical domain, as a function of the lock-in detector bandwidth here utilized [see Fig. 3.7(a)]. The speed-sensitivity trade-off can be significantly improved by utilizing an integrated low-noise amplifier (red-dashed line). (b) Current noise of the transimpedance amplifier utilized (blue line) that can be significantly reduced with an integrated low-noise amplifier (red and green lines) to improve the CLIPP performances in terms of speed and resolution.*

transmission of the waveguide is essentially flat across the same wavelength range. Indeed, the CLIPP is able to monitor light across a wide wavelength range, with a slight sensitivity variation, here amounting to only $\pm 20\%$ at the edges of the wavelength range, this behavior suggesting that there is a stronger overlap of the optical mode with surface states at lower wavelengths with respect to higher wavelengths.

Finally, it is worth noticing that, although the CLIPP is essentially a broadband light observer, it can distinguish and monitor simultaneously signals at different wavelengths that are labeled with pilot tones (see Sec. 5.2.5 for details), so that the CLIPP can be employed also in applications where a wavelength selective light monitor is preferred.

3.6.4 Speed and sensitivity

Figure 3.11(a) shows the resolution of the CLIPP read-out system (both in the electrical and optical domain) as a function of the bandwidth of the lock-in detector here utilized (see the discrete components setup of Fig. 3.7). The speed of the CLIPP is essentially limited by the noise of the transimpedance amplifier (TIA) utilized for the read-out of the electric signal [DHPCA-100 by Femto with noise around 2 pA·Hz$^{-1/2}$, see blue line in Fig. 3.11(b)]. As shown in Fig. 3.11(a), a trade-off exists between the de-

tection bandwidth (that is the bandwidth of the low-pass filter of the lock-in detector) and the resolution of the read-out system. Here, the input optical power is modulated with a chopper with frequency up to 10 kHz and simultaneously monitored by the CLIPP. The lock-in bandwidth is varied accordingly from 1 kHz to 40 kHz, whereas V_e is fixed to 2 V. The CLIPP speed is as high as 100 kHz at the optical power of -10 dBm, whereas the detection limit can be pushed down to -50 dBm, yet at the price of narrowing the bandwidth down to 1 Hz.

Nevertheless, the trade-off between speed and sensitivity of the CLIPP can be significantly improved by utilizing an integrated transimpedance amplifier. For instance, by employing our custom low-noise amplifier [red and green lines of Fig. 3.11(b)], with noise of about 0.1 pA·Hz$^{-1/2}$ around the typical frequency of the CLIPP (f_e = 1 MHz), the CLIPP sensitivity can be further enhanced by an order of magnitude, and the speed increased by a factor of 100 [see red dashed line in Fig. 3.11(a)]. This integrated electronic read-out system is described in more details in Sec. 5.2.2, where is utilized for the stabilization and feedback control of resonators assisted by the CLIPP.

3.6.5 Parasitism

As anticipated, the primary read-out path of the CLIPP is composed by the series of the conductance G due to the Si waveguide core with the two access capacitances C_A. The electric impedance corresponding to this model is shown in Fig. 3.12 with black dashed line as a function of the electric frequency from 1 kHz to 100 MHz. However, in parallel to this path, there are additional parasitisms that significantly affect the total electric impedance measured at the CLIPP electrodes, thus reducing the detection resolution and the contribution of G on the overall impedance.

The first path is given by the stray capacitance C_E (see inset of Fig. 3.12 that shows the equivalent electric circuit of the Si photonic waveguide structure) due to the direct capacitive coupling between the CLIPP metal electrodes, their metal tracks on the Si chip, and the external connection wires. Using an external discrete component read-out circuit, C_E is typically in the order of 1 pF, and thus largely dominating the total impedance.

Then, a second contribution is given by the capacitive coupling of the Si core to the Si substrate through the bottom oxide (modeled by the capacitances C_S), where the resistance of the thick Si substrate can be neglected [90].

Also, due to the spatial distribution of the total impedance, the lumped-

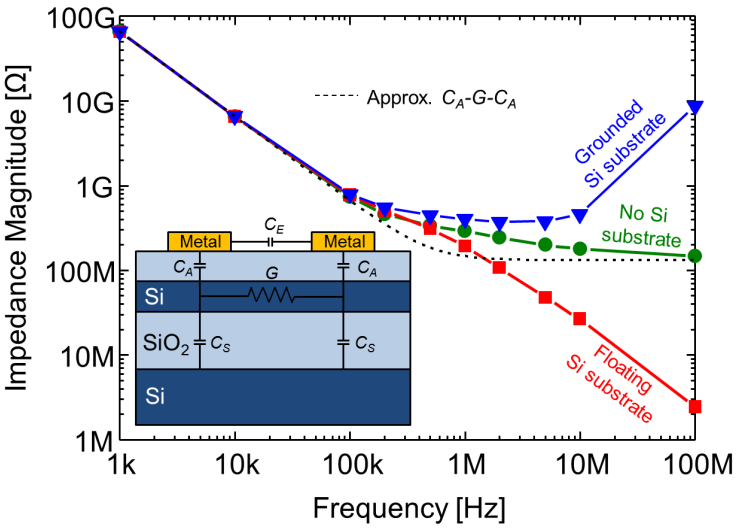

Figure 3.12: *FEM simulations of the electric impedance of the Si photonic waveguide structure comprised between the CLIPP electrodes in different conditions: approximation C_A-G-C_A (black dashed line), no Si substrate that is removed and replaced by a SiO_2 semi-plane (green line and circle markers), floating Si substrate (red line and square markers), grounded Si substrate (blue line and triangle markers). The inset reports the lumped-parameter equivalent electric circuit of the waveguide.*

parameter model, composed by a capacitance $C_A/2$ in series to a conductance G, is an approximation. Therefore, Finite Element Method (FEM) electromagnetic simulations have been performed to quantify the limitation of such estimate, and to investigate the impact of the Si substrate on the impedance spectrum, that is not directly measurable because of the large value of C_E. Initially, the Si substrate is removed and replaced by a SiO_2 lower semi-plane (green line and circle markers in Fig. 3.12): the distributed impedance of the layers underneath the electrodes produces a smoother transition with respect to the approximation C_A-G-C_A in the frequency range 100 kHz - 10 MHz, with sub-unitary slope (smaller than -20 dB/Dec as a constant phase element) between the capacitive region and the resistive plateau (at the edges of the spectrum the values of C_A and G are consistent with the model). Then, when the effect of the Si substrate is taken into account (with same doping of the core), the role of C_S distributed all along the waveguide core becomes clear. For a floating substrate (red line and square markers), the resistive plateau results truncated as, at high frequency, the impedance of C_S bypasses G. Instead, if the bottom of the

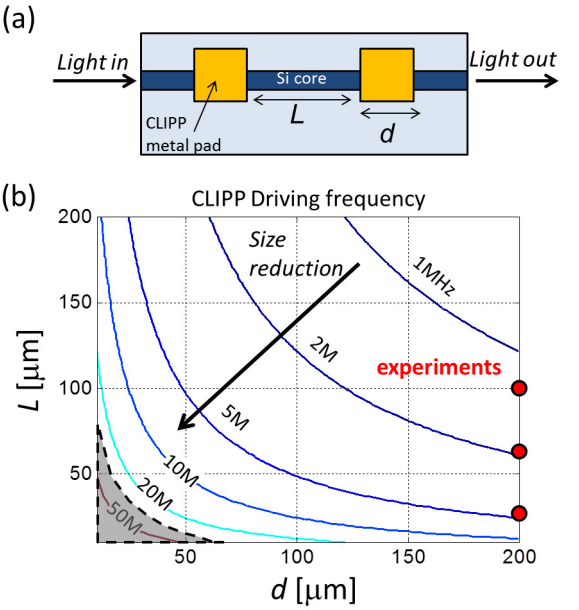

Figure 3.13: *Size and frequency constraints. (a) Top-view schematic of the CLIPP highlighting the distance between the metal contacts L and their length d. (b) Simulation of the driving frequency f_e of the CLIPP as a function of its size, indicating that in order to reduce the CLIPP size a higher operating frequency is required. The red circle markers indicate the experimental points tested in this work.*

substrate is fixed to ground in order to break this path (blue line and triangle markers), the current flows to ground, resulting in an increase of the measured impedance and the current effectively flowing in G is reduced.

The real condition experienced by the Si waveguide corresponds to an intermediate case between the floating and the grounded state, since the Si substrate is capacitively grounded through the bottom native oxide to the metal chip stage.

3.6.6 Size versus frequency

Here, we analize the relation between the CLIPP size and the driving frequency f_e. Tyically, the value of f_e is chosen to be higher than the frequency f_A of the pole associated to the access capacitance C_A, that can be expressed as

$$f_A = \frac{1}{2\pi R_{WG} C_A/2} \tag{3.4}$$

where $R_{WG} = 1/G$ is the resistance associated to the waveguide core. This is confirmed by the electric impedance spectra shown in Fig. 3.7(b) and Fig. 3.12: in fact, by chosing $f_e > f_A$ the resistance of the Si core can be accessed and measured directly.

As anticipated in Section 3.5, R_{WG} depends on the distance L between the metal electrodes, while C_A on the length d of the metal contacts, so that the total linear extension of the CLIPP is $2d + L$ [Fig. 3.13(a)].

Figure 3.13(b) well shows the behavior of f_A, here calculated with Eq. 3.4 and thus neglecting parasitic effects, as a function of the CLIPP size and highlighting the effect of L and d. It is straightforward to notice that by reducing the size of the CLIPP a higher operating frequency is required. For instance, while fixing the electrode length to d = 200 μm the CLIPP size can be reduced by narrowing the distance L between the metal contacts (see the red circle markers, representing the operation points tested within this work, that indicate that L has been reduced from 100 μm down to 25 μm by increasing f_e up to 5 MHz). A further reduction of the CLIPP size is possible by narrowing d, yet at the price of the driving the CLIPP at a higher frequency range. Typically, operating at frequency above 30 MHz represents a complication because the impact on the phase delays of the connection cables is no longer negligible, and the effect of the parasitisms become significant (in fact, the higher f_e, the higher the stray current flowing in C_E and C_S that shunts the waveguide conductive path).

3.7 The CLIPP in other semiconductor technologies

So far, the CLIPP concept and performance have been investigated and developed mainly in the silicon photonics platform. However, since the CLIPP operation relies essentially on a carrier generation process due to surface-states (see Chapter 4 for details), the CLIPP concept can be extended to other semiconductor technologies, such as for instance indium phosphide [91] and germanium [92], where surface states play a role.

Here, the CLIPP concept is demonstrated on an InP waveguide with the cross-section shown in the inset of Fig. 3.14, that was fabricated by the Heinrich Hertz Institute (HHI). The InGaAsP waveguide core (with refractive index 3.26 at 1550 nm) has a rib shape with width 2.5 μm, thickness 1 μm and 600 nm deep etch, and is placed on top of a InP substrate (refractive index at 1550 nm is 3.17). The waveguide structure is surrounded by an insulating cladding, on top of it the CLIPP metal pads are deposited.

Figure 3.14 shows the measured conductance variation ΔG versus waveguide power when the CLIPP is driven with an electrical signal at frequency

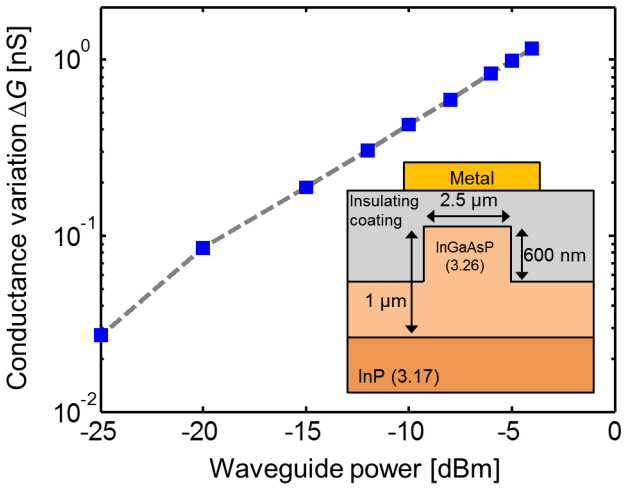

Figure 3.14: *Demonstration of the CLIPP on a indium phosphide waveguide with the cross-section reported in the inset (materials and dimensions are reported as well). Conductance variations ΔG were measured across a 20 dB optical power range, exhibiting similar sensitivity to that observed in silicon waveguides.*

V_e = 2 V and f_e = 100 kHz. The CLIPP operation was demonstrated across 20 dB dynamic range from -25 dBm to -5 dBm, and with similar sensitivity to that exhibited by silicon waveguides (Fig. 3.2).

Although a thorough characterization of the CLIPP in InP-based technologies has not been done yet, this result provides clear evidence that the CLIPP concept can be extended also to photonic platforms other than silicon.

CHAPTER 4

Observation of surface-state induced carrier absorption

This Chapter aims to provide some information on the physics behind the operation of the CLIPP, whose concept and performances were widely discussed in Chapter 3. In particular, a detailed analysis of the physical phenomena affecting light propagation in silicon waveguides is provided in Sec. 4.1, suggesting that SSA is the only candidate to be responsible for the CLIPP operation. Moreover, this is confirmed in Sec. 4.2 where the effects of SSA are experimentally measured with a novel all-optical experiment, this providing quantitative information on both the carrier density generated by SSA and on the absorption that they induce. Finally, we show that this result (achieved in the optical domain) is in line with that of the CLIPP (that operates in the electrical domain).

4.1 Phenomena affecting light propagation in silicon waveguides

In this Section surface-state absorption is identified as the physical effect responsible for the operation of the CLIPP, that is the observation of a change

in the waveguide conductance ΔG with optical power *P* (Fig. 3.2), by excluding all the other possible existing phenomena.

As is well known, the waveguide conductance *G* increases with the geometrical waveguide cross-section *A* = *wh* and decreases with the length *L* of the CLIPP according to the relation

$$G = \sigma \frac{A}{L} \tag{4.1}$$

where the electrical conductivity

$$\sigma = q\left(\mu_e N_e + \mu_h N_h\right) \tag{4.2}$$

of the material depends on the electric charge q, on the mobility of electrons (μ_e) and holes (μ_h), and on the volume density of electrons (N_e) and holes (N_h). Since A and L are fixed by the waveguide geometry, the measured ΔG is essentially due to a conductivity variation $\Delta\sigma$, that is to either a variation in the mobility ($\Delta\mu$) and/or in the density (ΔN) of electrons and holes.

Here, it is shown that a variation $\Delta\mu$ in the carrier mobility does not explain the measured $\Delta\sigma$. Then, focusing on carrier density variations ΔN, the existence of significant photocarrier generation mediated by two-photon-absorption effects is ruled out, proving that surface-state-absorption is the only candidate to be responsible for the observed changes in the waveguide conductance.

4.1.1 Variation of carrier mobility

Typically in Si optical waveguides the mobility of carriers varies in the presence of: (a) radiation pressure and electrostriction induced optical forces, (b) temperature and (c) carrier density variations.

Radiation pressure and electrostriction induced optical forces

From the measured ΔG versus P (see Fig. 3.2) the value of $\Delta\mu$ that would be required to justify the observed change in the waveguide conductance can be determined. By substituting Eq. 4.2 in Eq. 4.1, and assuming that in the p-doped silicon (N_h = 10^{15} cm^{-3}) the conductivity is essentially due to free holes, we obtain a variation of mobility

$$\Delta\mu = \frac{\Delta\sigma}{qN_h} = \frac{1}{qN_h}\frac{L}{A}\Delta G \tag{4.3}$$

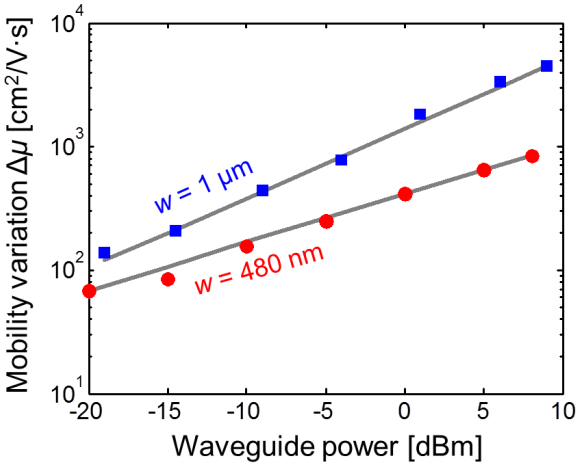

Figure 4.1: *Variation of carrier mobility $\Delta\mu$ as a function of the local waveguide power for the waveguides with width 480 nm (red circle markers) and 1 μm (blue square markers), the grey solid line provides a linear fit of the experimental points.*

that is shown in Fig. 4.1 for the same optical power range of Fig. 3.2. For instance, when the 480 nm wide waveguide operates at P = 0 dBm the mobility variation is $\Delta\mu$ = 417 cm^2/(V·s), which corresponds to a change in the relative hole mobility of $\Delta\mu/\mu_h$ = 0.93 (assuming a typical value μ_h = 450 cm^2/(V·s) for the mobility of free holes). Such mobility variation would require the application of a pressure to the waveguide of about 10^7-10^8 Pa [93]. However, when operating in the optical power range of Fig. 3.2 (from -30 to 10 dBm) the typical radiation pressure level on the waveguide is lower than $2{\cdot}10^3$ Pa [94]. Therefore, radiation pressure induced optical force is not the physical effect responsible for the observed photocarrier generation. Likewise, electrostriction can be excluded, because it induces optical forces of about the same order of magnitude as radiation pressure [95].

Temperature variations

The change of the waveguide conductance ΔG versus the waveguide temperature was measured in absence of light by controlling the chip temperature through a thermo-optic cooler placed below the sample. Figure 4.2 shows that 1 K temperature change is responsible for ΔG = 1.17 nS, this implying that a temperature variation by tens of degrees would be required to justify the results of Fig. 3.2. However, in this case the effects of this large temperature change should be observed also in the optical domain as a

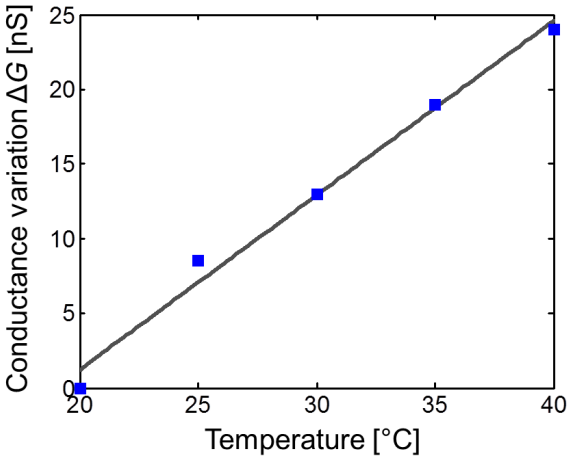

Figure 4.2: *Measured conductance variation ΔG in absence of light in the waveguide CLIPP with a width of 1 μm as a function of temperature (blue square markers), the grey solid line (slope 1.17 nS/K) provides a linear fit of the experimental points.*

wavelength shift of the waveguide transmission spectrum, amounting to 75 pm/K for the single mode silicon waveguide with w = 480 nm on TE polarization (see Sec. 5.1 for details). However, no significant wavelength shift (> 1 pm) is observed for the optical power range employed in the CLIPP measurement.

Carrier density variations

Indeed a variation in the density of carriers induces a change in their mobility [96, 97]. At a typical doping level of 10^{15} cm^{-3} for SOI wafers, to halve the carrier mobility it is necessary to increase their density by at least two orders of magnitude [96, 97]. However, in the experiment of Fig. 3.2, the measured photocarrier generation is of the same order of magnitude of the typical doping level of the waveguide (see Sec. 3.3.2), and thus not sufficient to significantly modify the mobility.

4.1.2 Variation of carrier density

In conventional silicon waveguides, free carrier density varies in presence of two-photon absorption and surface-state absorption. Photocarrier generation by TPA increases quadratically with the local optical power P [67]

$$\Delta N = \frac{\tau_{eff}\beta_{TPA}}{2h\nu}\frac{P^2}{A_{eff}^2} \tag{4.4}$$

where τ_{eff} is the carrier recombination time, β_{TPA} is the TPA coefficient, $h\nu$ is the photon energy and A_{eff} the waveguide effective area. Since ΔG increases linearly with ΔN (see Eq. 4.1 and 4.2), TPA would require a quadratic relation between ΔG and P. As in Fig. 3.2 no quadratic dependence is observed, TPA is not the physical mechanism responsible for the measured photocarrier generation.

In conclusion, SSA is the only physical effect that justifies qualitatively and quantitatively the behavior of the CLIPP. Next Section will provide direct evidence of this result by comparing the measurement performed with the CLIPP (Fig. 3.2) with a novel all-optical experiment designed to observe the effects of SSA (generated carriers and absorption).

4.2 Observation of absorption due to surface-state induced carriers

As shown in Fig. 3.2, as light propagates in a silicon waveguide a number of carriers are generated, with density that depends on the optical intensity in the waveguide. If this is true, then, according to the well known Drude model of free carrier absorption, the presence of these carriers would induce an additional absorption effect in the waveguide, whose behavior depends on the optical power as well. Here, experimental observation of this phenomenon is shown. Furthermore, by comparing its behavior with the CLIPP measurement of Fig. 3.2, a direct evidence that SSA is responsible for the CLIPP operation is provided.

4.2.1 The concept

Figure 4.3 reports a schematic that describes the concept behind the experiment here proposed to measure directly the effects of SSA. Let us assume that a light signal with sinusoidal modulation (with angular frequency ω_0) is injected in a photonic waveguide. If the total waveguide loss α is constant with light intensity, then the output signal will have the same frequency component ω_0 [Fig. 4.3(a)]. In constrast, if α is a function of power, also other harmonic components, at frequencies $2\omega_0$, $3\omega_0$ etc., will be present at the output of the waveguide [Fig. 4.3(b)].

The case of Fig. 4.3(b) is typically experienced by Si photonics waveguides at high optical power, where two-photon absorption and free-carrier

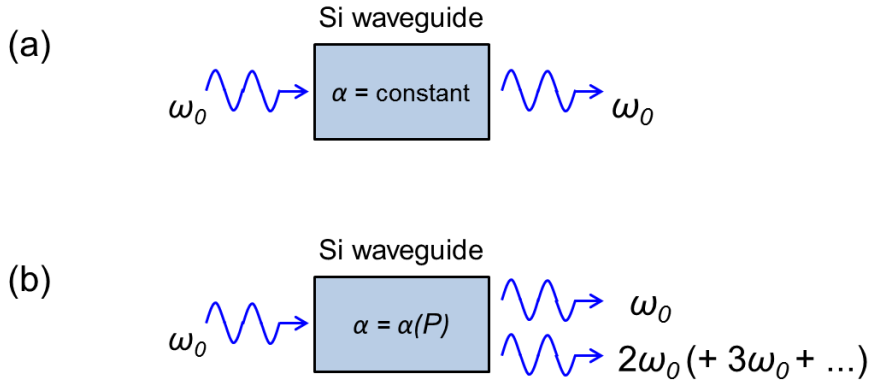

Figure 4.3: *Schematic representation of the proposed experiment, where a modulated light signal with angular frequency ω_0 is injected in a silicon waveguide. (a) If the total waveguide loss α does not depend on the optical power P, the frequency of the signal at the output is ω_0, that is the same of the input. (b) If α is a function of P, other harmonic components at frequencies $2\omega_0$, $3\omega_0$ etc. appear in the signal at the output of the waveguide.*

absorption (FCA) processes induce a non-linear extra-loss that is a function of light intensity [43, 67]. However, in presence of absorption due to SSA-induced carriers, the total loss of the waveguide is a function of the optical intensity even at low-power, where the waveguide operates in the linear regime and TPA/FCA-induced loss is typically negligible. Therefore, by measuring the magnitude of the harmonic components $2\omega_0$, $3\omega_0$ etc. at the output of the waveguide, quantitative information on the loss due to SSA-induced carriers can be found.

4.2.2 Model of waveguide loss

In order to better understand how the measurement of the harmonic components ($2\omega_0$, $3\omega_0$ etc.) leads to the observation of the loss induced by SSA-generated carriers, the following model of waveguide loss α with optical power P is here utilized:

$$\alpha = \alpha_0 + \alpha_1 + \alpha_2 \tag{4.5}$$

where α_0 does not depend on power, α_1 has a linear dependence on P, and α_2 a quadratic dependence on P, so that the loss can be written as:

$$\alpha = a_0 + a_1 P + a_2 P^2 \tag{4.6}$$

where a_0, a_1 and a_2 are coefficients.

The first term (α_0), that is constant with power, represents the effects of defects and imperfections like roughness, that typically result in the coupling of the optical mode with radiation modes (radiation loss) and with counter-propagating modes (backscattering) [98]. Also, this term includes the absorption α_{SSA} due to surface states, that is the loss associated to single photon absorption due to the states localized at the Si/SiO_2 interface, typically within the first three/four atomic layer of the silicon core [81]. It is worth noticing once again that these states are mainly related to the breaking of the symmetry of the Si lattice at the interface, and therefore are present in any silicon photonic waveguide, regardless of the smoothness, quality and uniformity of the waveguide walls.

The second term, α_1, that has a linear dependence with power, represents the effects of TPA according to the well-known relation $\alpha_{TPA} = \beta_{TPA} I$, where α_{TPA} is the loss induced by TPA, β_{TPA} is the TPA coefficient, and I the light intensity. Also, α_1 includes a loss contribution induced by the presence of carriers generated by SSA (that here is measured). The linear dependence of this term from power is easily confirmed if one considers the equation that describes the temporal behavior of the carriers

$$\frac{\partial N}{\partial t} = \frac{\alpha I}{h\nu} - \frac{N}{\tau} \tag{4.7}$$

where N is the carrier density, t is time, $h\nu$ is the photon energy, and τ is the carrier recombination time. In Eq. 4.7, the first term ($\alpha I/2h\nu$) represents a contribution due to the generation of carriers, while the second (N/τ) takes into account the recombination process. If $\alpha = \alpha_{SSA}$, at the equilibrium the SSA-generated carrier density is

$$N = \frac{\alpha_{SSA}\tau}{h\nu} I \tag{4.8}$$

showing the linear relation between the carrier density and power. Furthermore, if one considers that according to Soref's equations [99] the absorption due to free carriers has a linear dependence with carrier density, it is straightforward to find that a linear dependence between loss due to SSA-induced carriers and power exists.

The last term of Eq. 4.5, α_2, has a quadratic dependence on P, and represents the effect of FCA, which is the dominant contribution in silicon photonic waveguides operating at high power.

The measurement of the harmonic components versus power at the output of the waveguide provides quantitative information on the magnitude of

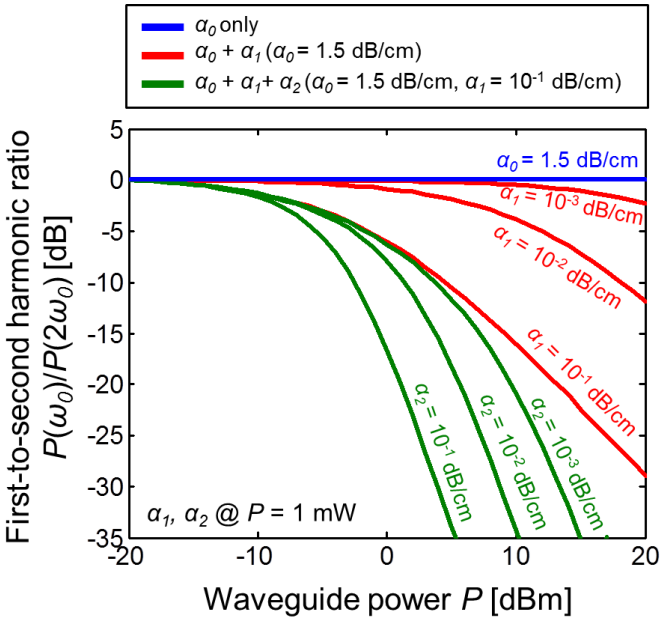

Figure 4.4: *Simulations of the ratio $P(\omega_0)/P(2\omega_0)$ between the first and the second harmonic components versus optical power, and for different values of α_1 and α_2 (values indicated in the figure refer to P = 1 mW).*

the various loss terms, α_0, α_1, and α_2. This is shown in Fig. 4.4, that reports simulations of the normalized ratio $P(\omega_0)/P(2\omega_0)$ between the fundamental component at frequency ω_0 and the harmonic component at $2\omega_0$ versus power, for different values of the absorption terms. If the waveguide loss were constant with power, no variation of $P(\omega_0)/P(2\omega_0)$ with power would be observed. This condition is shown in blue line, where the contribution of α_1 and α_2 are neglected. In constrast, if α is a function of power, a dependence of $P(\omega_0)/P(2\omega_0)$ with light intensity is observed. This is shown with red and green lines, representing respectively the case where only α_0 and α_1 are considered, and the case where α_2 is included as well. It is worth noticing that, by increasing respectively the values of α_1 and α_2, the slope of the curve increases, with much larger values when the contribution of α_2 is included, that is dominant at high intensities.

4.2.3 Experimental setup

Figure 4.5 shows the experimental setup utilized to measure the ratio between the harmonic components at frequencies ω_0 and $2\omega_0$. The light signal at the input of a Si photonic waveguide is generated by means of

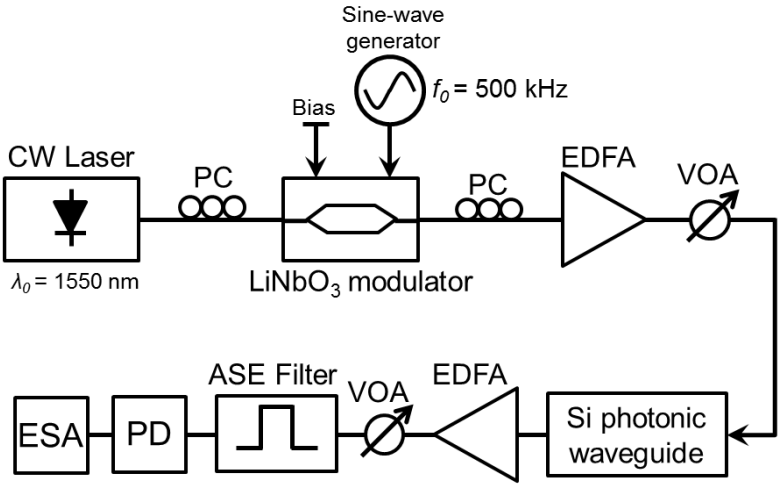

Figure 4.5: *Experimental setup utilized to measure the harmonic components at angular frequencies ω_0 and $2\omega_0$ (with $\omega_0 = 2\pi f_0$).*

a continuous-wave (CW) laser and a $LiNbO_3$ intensity modulator. The light signal is around 1550 nm, whereas the sinusoidal modulation is at frequency f_0 = 500 kHz. An erbium-doped-fiber-amplifier (EDFA) and a variable-optical-attenuator (VOA) enable to accurately and finely control the light intensity at the input of the waveguide. Polarization controllers (PCs) are utilized at the input and at the output of the modulator to control the polarization of the light respectively injected in the modulator and coupled to the photonic waveguide.

At the output of the waveguide the light is collected by a photodetector (PD), whose output feeds an electrical-spectrum-analyzer (ESA) that enables to measure the harmonic components at the relevant frequencies. EDFA and VOA are here employed to provide the same average power to the photodetector, and an ASE filter to reduce the noise components introduced by the EDFAs included in the setup.

4.2.4 Experimental results

Figure 4.6 reports the results of the measurement performed with the technique described in Sec. 4.2.2 and 4.2.3. From the measurement of the ratio between $P(\omega_0)$ and $P(2\omega_0)$ the magnitude of α_1 can be extracted (for low power level where P is lower than 1 mW) considering that α_0 does not affect the ratio of the harmonic components (see Sec. 4.2.2 for details), and that the effect of FCA (that is α_2) can be neglected in practical cases and re-

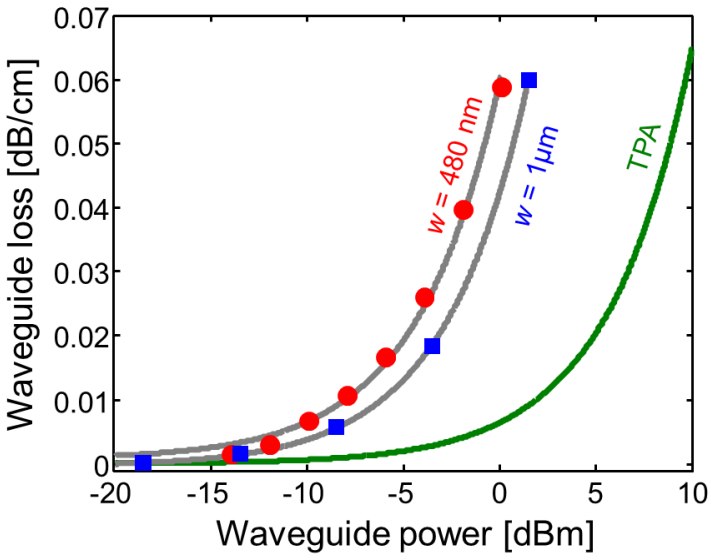

Figure 4.6: *Experimental observation of the absorption due to the carriers generated by SSA processes for waveguides with width of 480 nm and 1 μm. This term is about one order of magnitude larger than TPA for waveguide power up to 1 mW.*

alistic experimental conditions up to a local power around 1 mW [43]. The linear absorption term α_1 is shown versus local waveguide power in Fig. 4.6 for waveguides with width 480 nm (red circle markers) and 1 μm (blue square markers), whereas the grey solid lines provide a linear fit of the experimental points. Also, Fig. 4.6 shows in green solid line the dependence of TPA on power for a waveguide with width 480 nm (here β_{TPA} = 0.7 cm/GW and the effective area is A_{eff} = 0.047 μm^2). The loss due to TPA is more than one order of magnitude smaller than the measured linear loss α_1. This result indicates that TPA has a negligible contribution on α_1 up to 1 mW of power, thus suggesting that for low-power level the linear term of absorption is dominated by the loss contribution given by the carriers generated by SSA.

Furthermore, the result here obtained is compared to the measurement provided by the CLIPP. To this aim the density of carriers ΔN generated by SSA is calculated from the measured α_1 by means of the Soref's equations that, as anticipated, correlates the absorption due to free carriers with their density [99]. This is shown in blue square markers in Fig. 4.7 for the 1 μm wide waveguide, whereas the grey solid line provide a linear fit of the experimental points. Also, the SSA-induced carrier density measured

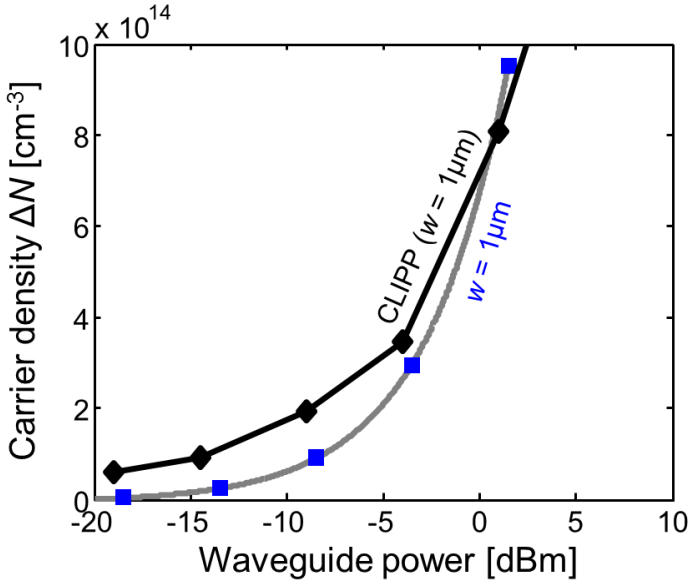

Figure 4.7: *Comparison of the carrier density measured by the CLIPP and with the harmonic components on the same waveguide. The good agreement between the two curves clearly proves that SSA is responsible for the CLIPP operation.*

by the CLIPP on the same waveguide is shown (black diamond markers and solid line), this quantity being provided by correlation of the measured conductance G (Fig. 3.2) to carrier density with Eq. 4.1 and 4.2. The good agreement between the carrier density measured with the CLIPP (in the electrical domain) and with the harmonic components (in the optical domain) provides a clear evidence that the physical effect responsible for the CLIPP operation is indeed SSA.

CHAPTER 5

Stabilization and feedback control

This Chapter analyzes in detail stabilization and feedback control of photonics integrated circuits, to mitigate the detrimental effects of fabrication tolerances, thermal fluctuations, aging, mutual crosstalk and fault events. These effects are particularly severe in silicon photonics, and become prohibitive when dealing with circuits hosting many photonic components. First, passive approaches based on the trimming of athermal silicon waveguides will be discussed (Sec. 5.1), then active approaches exploiting thermo-optic actuators and the transparent light monitoring enabled by the CLIPP will be presented (Sec. 5.2). Finally, the Chapter ends with Sec. 5.3, where the CLIPP and feedback loops are utilized for fiber-to-waveguide alignment; though this application is slightly different from those of the first Sections of this Chapter, this topic is well suited within a larger discussion on circuit stabilization and feedback control.

5.1 Passive thermal stabilization

Athermal waveguides represent one of the fundamental building blocks of silicon photonic integrated circuits because they mitigate the strong dependence of Si on temperature. In fact, because of the large thermo-optic (TO)

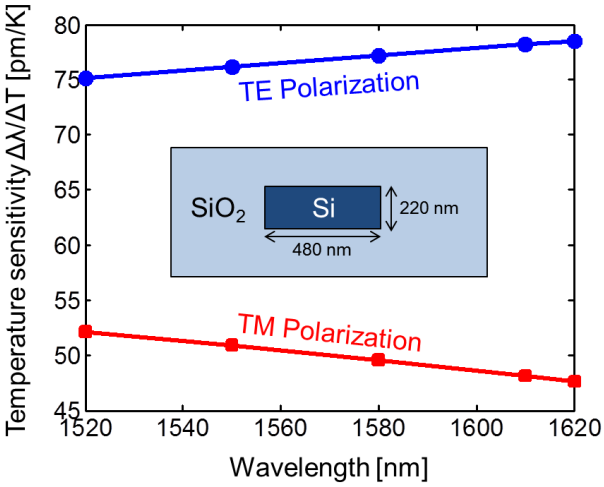

Figure 5.1: *Temperature sensitivity $\Delta\lambda/\Delta T$ versus wavelength of a typical monomode channel silicon waveguide on TE and TM polarization.*

coefficient of Si ($\sim 1.8 \cdot 10^{-4}$, that is about ten times greater than that of silica), even small temperature gradients or fluctuations across the chip may result in large wavelength shifts and severe distortions in the response of interferometric devices. For instance, in a traditional single mode Si channel nano-waveguide [11], a temperature drift of 1°C shifts the overall transfer function of any device by about 75 pm and 50 pm respectively on TE and TM polarization [Fig. 5.1].

Typically, in integrated optics, this issue is counteracted by utilizing active heaters on top of the waveguide (see Sec. 2.1) and thermo-electric chip coolers; however this approach consumes power, and the thermal management of the chip becomes prohibitive when dealing with large scale integrated photonic circuits [9]. The most common approach to passively counteract for temperature drifts in photonic circuits is to cover the waveguide core with a top cladding material with a negative TO coefficient, opposite to that of the core, thus achieving the desired thermal compensation. This approach, that has been realized mainly with polymers (and only recently with CMOS-compatible materials such as TiO_2, see Sec. 5.1.3 for details), was first proposed and demonstrated on glass slab [100] and channel waveguides [101], and then extended to standard Si waveguides [102], observing no appreciable wavelength shift with temperature variations [103, 104].

Instead, according to other approaches, it was demonstrated that some specific interferometric devices, such as Mach-Zehnder interferometers,

can be designed to be robust against temperature fluctuations, though using waveguides that are inherently temperature sensitive. For instance, the two arms of the interferometer can either have different width [105] or operate on orthogonal polarization states [106] in order to cancel out the temperature dependence of the overall circuit. This technique has the advantage to avoid the deposition of an additional thermally compensating material, but typically results in a larger circuit footprint [105] and is hardly applicable to generic circuits [51].

However, although athermal waveguides are quite efficient in terms of thermal compensation [103, 104], Si waveguides are still sensitive to fabrication tolerances, which are one of the main limitations of Si photonic devices. In a sub-micrometer single mode Si waveguide, a variation of 1 nm in the core width results in a shift of about 100 GHz (0.74 nm) in the frequency response of any interferometric device [42–44] (see Chapter 2 for details). Moreover, because of their athermal nature, these waveguides cannot be tuned by exploiting the TO effect, as typical in integrated optics. One approach employs slot Si resonators coated with PMMA polymer to reduce the thermal dependence, and exploits ultraviolet (UV) radiation to trim the resonant wavelength [107]; however, the achieved thermal dependence is high (27 pm/°C) and the trimming capability still limited (lower than the linewidth of the resonator).

Here, the trimming of athermal Si waveguides is demonstrated by exploiting the photosensitivity to near bandgap light of As_2S_3 chalcogenide glass [108]. By depositing a thin photosensitive layer of As_2S_3 chalcogenide glass between the Si core and the polymer top cladding, the design of the Si athermal waveguide [103] is combined with the Si trimmable waveguide (see Sec. 2.2.2), thus giving birth to a new Si waveguide technology that is athermal and trimmable (Sec. 5.1.1). Moreover, this waveguide technology is highly resilient to high power induced thermal effects (which is very appealing for non linear applications), and thus pushes towards a concept of power insensitive Si devices (Sec. 5.1.2).

5.1.1 Athermal and trimmable silicon waveguide

Figure 5.2(a) shows a schematic view of the cross section of the athermal and trimmable waveguide that was fabricated at MIT. A 205 nm thick layer of amorphous silicon (a-Si) was deposited on top of a 3 μm thick silica (SiO_2) buffer oxide by means of plasma enhanced chemical vapor deposition (PECVD) at 200°C using silane (SiH_4, 60 sccm) and argon (Ar, 300 sccm) [104, 109]. Channel waveguides, with a width of 500 nm to

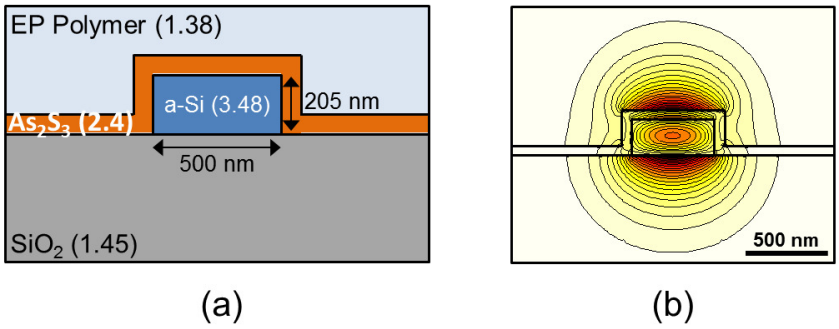

Figure 5.2: *(a) Schematic of the cross section of the athermal and trimmable waveguide, materials and refractive indices are indicated. (b) Profile of the major electric field component of the TM mode of the athermal and trimmable waveguide.*

ensure single mode propagation on TM polarization, were patterned via photolithography [104]. Then, a 50 nm thick layer of photosensitive As_2S_3 glass was evaporated on top of the waveguide core, according to the process described in [60]. Next, 3 μm of a hyperlinked fluoropolymer proprietary of Enablence Inc., hereinafter named EP, was spin coated on top of the waveguide structure. Finally, the samples were exposed to UV radiation with an intensity of 5 mW/cm^2 for 20 minutes, and baked in vacuum at 150°C for 4 hours to cure and stabilize the polymer properties.

The waveguide cross section is optimized to provide both athermal operation and trimming functionality. Figure 5.2(b) shows an electromagnetic simulation, performed via Film Mode Matching (FMM) method, of the profile of the major component of the electric field on TM polarization. The mode expands from the a-Si core, through the As_2S_3 layer and into the EP polymer top cladding in such a way that the effective behavior of the waveguide is properly weighted over the refractive indices of SiO_2 (1.45), a-Si (3.48), As_2S_3 (2.4) and EP polymer (1.38). The effective TO performance of the waveguide depends on the amount of optical mode contained in each of the layers: SiO_2 (TO coefficient 10^{-5}, confinement factor 24%), a-Si (TO coefficient $2.3{\cdot}10^{-4}$, confinement factor 45%), As_2S_3 (TO coefficient $4{\cdot}10^{-5}$, confinement factor 10%) and EP polymer (TO coefficient $-2.65{\cdot}10^{-4}$, confinement factor 21%).

Racetrack ring resonators in an all-pass filter configuration were fabricated to demonstrate the effectiveness of the athermal and trimmable waveguide technology. The rings have a length of 326 μm (free-spectral-range FSR = 256 GHz) and a bending radius of 20 μm, with a coupling length of

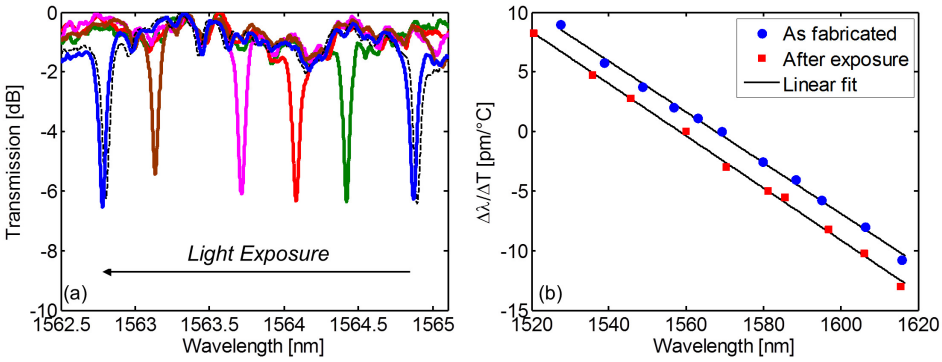

Figure 5.3: *(a) Visible light induced trimming of the resonant wavelength of an athermal and trimmable ring resonator from the as-fabricated condition (blue solid line) to 1 FSR (black dashed line). (b) Athermal performance $\Delta\lambda/\Delta T$ of the athermal and trimmable ring resonator, in the temperature range 20-40°C, before (blue circle markers) and after (red square markers) a 10 nm wide trimming of its resonant wavelength; the black solid line indicates a linear fit of the experimental points.*

100 μm and a gap of 600 nm between the bus waveguide and the resonator. Figure 5.3(a) shows the trimming of the resonant wavelength of a ring filter across an entire FSR. Under near bandgap visible light exposure, the resonance blue-shifts from the as-fabricated condition (blue solid line) to 1 FSR (black dashed line), with neither significant change in the linewidth nor in the notch depth of the filter, and thus with no introduction of additional loss (see Sec. 2.2.3). The trimming is performed with the technique described in Sec. 2.2: a multimode optical fiber, with a 30 μm mode field diameter, is coupled to a common halogen lamp and used to selectively expose desired areas of the ciruit. The lamp has a spectrum in the wavelength range 450-650 nm and an intensity that can be varied from 0.3 mW/cm^2 to 10 mW/cm^2.

The sensitivity of the ring resonance to temperature variation $\Delta\lambda/\Delta T$ was measured before and after trimming of its resonant wavelength, in the temperature range 20-40°C, as shown in Fig. 5.3(b). The temperature sensitivity of the as-fabricated device (blue circle markers) is more than one order of magnitude below that typical of Si waveguides (50 pm/°C and 70 pm/°C respectively on TM and TE polarization) across a wavelength range of almost 50 nm. No appreciable wavelength shift with temperature is observed around 1569 nm, hereinafter named "athermal wavelength", with variations in wavelength that arise from waveguide dispersion. After a 10 nm trimming of the ring resonance, corresponding to about 5 FSRs, the

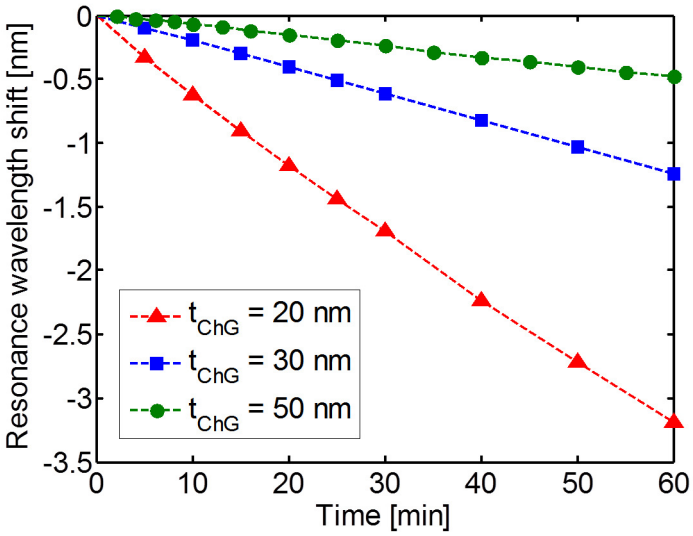

Figure 5.4: *Resonance wavelength shift of athermal and trimmable resonators with different As_2S_3 thicknesses, t_{ChG} = 20, 30, 50 nm, when exposed to a constant visible light intensity of 10 mW/cm^2 for 60 minutes.*

athermal performance rigidly blue-shifts by about the same quantity (red square markers), with no appreciable change in the slope of the temperature sensitivity curve. It is worth noticing that the athermal wavelength is continuously trimmed across the same 10 nm bandwidth, resulting in a value around 1559 nm after exposure.

Athermal and trimmable ring resonators with different thicknesses of the As_2S_3 chalcogenide layer t_{ChG} were fabricated in order to investigate speed and time response of the trimming process, and the effect occurring in As_2S_3 under near bandgap illumination. Figure 5.4 shows the resonant wavelength shift of three identical rings, but with different t_{ChG} of 20, 30 and 50 nm. The exposure was performed with the same light intensity of 10 mW/cm^2 for 60 minutes for all the resonators. Visible light illumination linearly blue-shifts the resonances of the filters, with higher speed for samples with thinner As_2S_3 layer, respectively 53, 21 and 8 pm/min for t_{ChG} = 20, 30, 50 nm. The observed wavelength blue-shift, that corresponds to a decrease of the refractive index of the As_2S_3 glass, as well as the measured trimming rate, that increases with decreasing As_2S_3 thickness, suggests that the dominant effect occurring in these thin As_2S_3 films when exposed to visible light is volume expansion [110, 111].

Finally, it is worth noticing that the athermal and trimmable waveg-

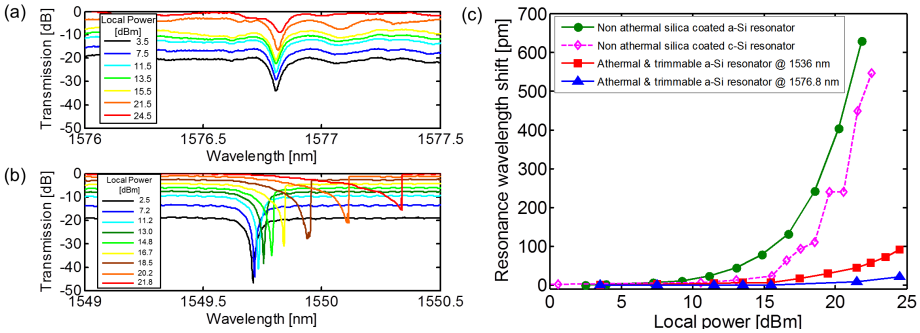

Figure 5.5: *Measured transmission of (a) athermal and trimmable and (b) non-athermal ring resonators for increasing local power stored in the cavity at the resonant wavelength. (c) Measured resonance wavelength shift as a function of the local power for a non-athermal silica coated a-Si resonator (green circle markers and solid line), a non-athermal silica coated c-Si resonator (pink diamond markers and dashed line), and an athermal and trimmable resonator, at the wavelength of 1536 nm (red square markers and solid line) and 1576.8 nm (blue triangle markers and solid line).*

uide design here presented is quite general and can be extended to include devices on TE polarization and other photonic platforms, including also waveguides with p-n regions acting as modulators or switches.

5.1.2 Resiliency to high power induced thermal effects

The transmission of the athermal and trimmable waveguide was tested at high optical power to evaluate its performance for use in both linear and non linear applications. Typically, when operating at high power levels, Si devices experience an extra loss and a thermal red-shift of the transfer function, induced by two-photon-absorption and free-carrier-absorption, which represent the main limitations in non linear applications [43]. One approach that has been demonstrated to mitigate the thermal red-shift induced at high power employs Si etchless ring resonators [112], however devices are still sensitive to ambient temperature fluctuations.

In Fig. 5.5(a) we show the transmission of an athermal and trimmable resonator with a quality factor of about $1.3{\cdot}10^4$ for increasing local power stored in the cavity at the resonant wavelength (and estimated according to [43]), from 3.5 dBm (black line) to 24.5 dBm (red line). No appreciable distortion of the transmitted resonance or change in the linewidth is observed up to a local power level of 21.5 dBm (orange line); only a slight resonant wavelength red-shift amounting to 8 pm (1 GHz) for a local power of 21.5 dBm is measured. For higher power levels the effect of TPA and

thermal processes gradually increases, resulting in a wavelength shift of 20 pm (2.4 GHz) at 24.5 dBm (red line).

However, the TPA/FCA induced thermal red-shift measured in our athermal and trimmable devices is significantly lower than that typically experienced by non-athermal Si waveguides. Figure 5.5(b) shows the transmission of a non-athermal a-Si resonator that has a quality factor ($1.5{\cdot}10^4$) comparable to the athermal and trimmable ring, with the same a-Si waveguide core size, but is coated with SiO_2 instead of As_2S_3 and EP polymer. This device clearly experiences a much larger thermal red-shift than the athermal and trimmable resonator, and a strong distortion of the linewidth induced by optical bistability at high power.

In Fig. 5.5(c) we compare quantitatively the resonant wavelength shift observed in the athermal and trimmable resonator at two different wavelengths (red square and blue triangle markers, and solid lines), as a function of the power stored in the cavity at the resonance, with that observed in the non-athermal a-Si ring resonator (green circle markers and solid line). The thermal red-shift measured in the athermal and trimmable resonator is well below that of the non-athermal device across the entire measured local power range, up to 24.5 dBm. In particular, at a power level of 21.8 dBm, the measured wavelength shift is 628 pm for the non-athermal ring, and 9 pm for the athermal and trimmable ring at the wavelength of 1576.8 nm, thus achieving a 70-fold thermal compensation. Although the magnitude of the thermal red-shift is wavelength dependent in the athermal and trimmable resonators, the substantial thermal compensation provided by this waveguide technology is mantained across a wide wavelength range: for instance, at the wavelength of 1536 nm (red markers and dashed lines), the measured red-shift is 48 pm with a local power of 21.8 dBm, more than one order of magnitude lower than the non-athermal resonator.

Finally, in order to provide a reference level for the results of Fig. 5.5(c), we also report the typical resonant wavelength shift of well known non-athermal silicon-on-insulator resonators [11] (pink diamond markers and dashed line). The crystalline silicon (c-Si) waveguide core has a similar size (480 nm wide, 220 nm thick) to that of the other a-Si resonators (both athermal and trimmable, and non-athermal), and is coated with SiO_2 [43]. The c-Si resonator (measured on TE polarization) experiences roughly the same wavelength shift with increasing local power of the non-athermal a-Si resonator. This suggests that the robustness to high optical power that we demonstrated with a-Si technology can be achieved also with traditional c-Si waveguides employing the athermal design since refractive index and TO coefficient of the two materials are similar.

5.1.3 Toward a CMOS-compatible athermal and trimmable silicon waveguide

Although polymer-assisted athermal waveguide are quite efficient in terms of thermal compensation, polymers materials were addressed to suffer from chemical instability, mechanical weakness, and poor compatibility with CMOS processes [59]. Therefore, many research efforts were recently dedicated to the use of titanium dioxide (TiO_2) as a cladding material of silicon waveguides [113, 114], because it is one of the few CMOS-compatible materials exhibiting negative TO coefficient (-$1{\cdot}10^{-4}$ K^{-1}). By suitably engineering the mode confinement in the waveguide, TiO_2-cladded microring resonators with a resonant shift as low as -1.6 pm/K (over a range of 5 K) for TE polarization [113] and a comparable shift for TM polarization [114] were demonstrated at 1550 nm. However, the price to be paid is the increase of the waveguide propagation loss (up to 8 dB/cm [113] and 16 dB/cm [114]), which is expected to decrease by reducing the scattering at the Si-TiO_2 interface [115]. With the same approach, the temperature dependent wavelength shift of hybrid SiN-TiO_2 microring resonators was reduced down to 0.073 pm/K, which is almost two orders of magnitude lower than that of uncladded SiN resonators [116]. Advantageously, this method can be applied to different waveguide technologies, including plasmonic waveguides [117], and to generic optical circuits. However, recent investigations pointed out that thermo-stress-optic effects can suppress the large negative TO coefficient of TiO_2 (by more than two orders of magnitude) if the material is not allowed to thermally expand [118], this effect constraining the design of the waveguide.

Nevertheless, similarly to the the case of polymer-coated waveguides (Sec. 5.1.1), silicon waveguides remain sensitive to fabrication tolerances and post-fabrication treatments are still required to tune/trim the device to the desired transfer function. In the remaining of this section, the design of a CMOS-compatible athermal and trimmable silicon waveguide is proposed. Athermal operation is achieved with the beneficial thermal compensation provided by TiO_2, whereas the trimming/tuning functionality is provided by a thin layer of CMOS-compatible barium titanate ($BaTiO_3$) sandwiched in between the Si core and the TiO_2 upper cladding, that allows control of its optical properties with application of an electric field.

$BaTiO_3$ is a ferroelectric transparent insulator widely employed in novel spin-electronic devices [119, 120], and as a waveguide on MgO and GaAs-based platforms [121–123] and in Si photonics [124, 125]. Application of an electric field modifies the refractive index of $BaTiO_3$, inducing a varia-

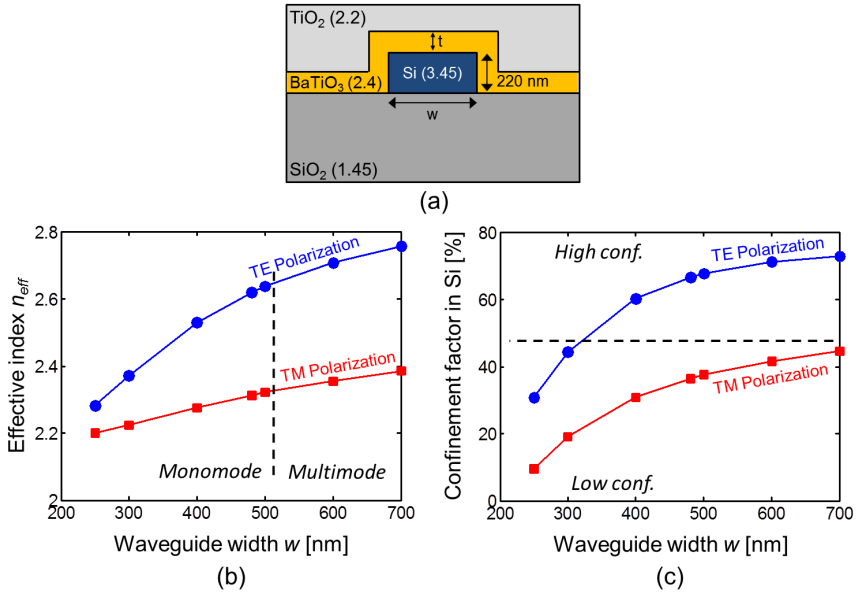

Figure 5.6: *(a) Schematic of the cross-section of the CMOS-compatible athermal and trimmable silicon waveguide, where materials and refractive indices are indicated. Electromagnetic simulations of the (b) effective indices and (c) confinement factors in silicon of TE and TM modes of the waveguide as a function of the waveguide width w (here t = 50 nm). Simulations are performed by means of FMM method.*

tion that can be larger than 0.1 [126]. In addition, $BaTiO_3$ exhibits a pronounced photorefractive effect [127].

Figure 5.6(a) shows a sketch of the cross-section of the CMOS compatible athermal and trimmable silicon waveguide. The thin layer of $BaTiO_3$ (with refractive index at 1550 nm around 2.4 and TO coefficient of $2{\cdot}10^{-4}$ K^{-1}) is grown on top of a Si core channel waveguide (with thickness 220 nm). On top of it a 3 μm thick layer of TiO_2 (with refractive index at 1550 nm of 2.2 and TO coefficient of -10^{-4} K^{-1}) is deposited. The thickness t of the $BaTiO_3$ layer and the width w of the Si core should be designed in order to provide thermal compensation and trimming functionality. It is straightforward to notice that, from the point of view of the athermal design, the main difference with the athermal and trimmable waveguide of Sec. 5.1.1 and 5.1.2 is the TO coefficient of the trimming layer, that here is of the same order of magnitude of that of silicon, and therefore has significant impact on the thermal behavior of the waveguide.

Figures 5.6(a)-(b) show electromagnetic simulations of the effective indices and confinement factors (in the silicon core) of TE and TM modes

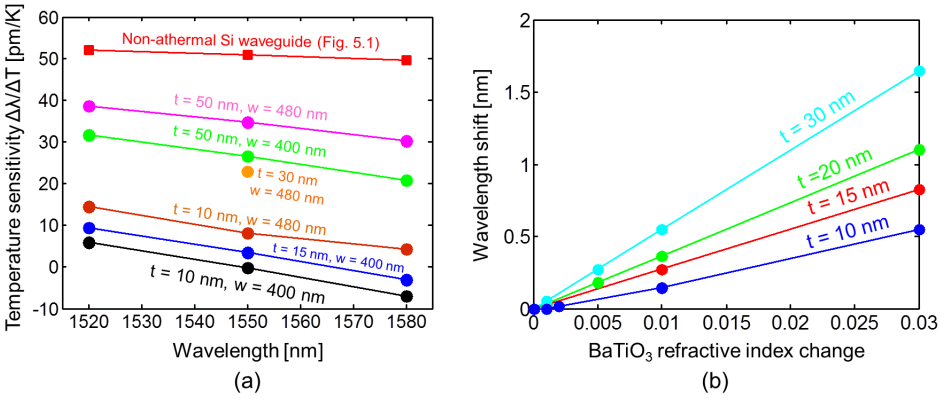

Figure 5.7: *(a) Temperature sensitivity versus wavelength of the athermal and trimmable waveguide for different waveguides widths w and $BaTiO_3$ thicknesses t; the conventional non-athermal waveguide is reported on top with red sqaure markers and solid line. (b) Wavelength shift that can be achieved by changing the barium titanate refractive index by the athermal and trimmable waveguide with w = 400 nm. Simulations are here performed by FMM method.*

of the waveguide for different widths w (here t is fixed to 50 nm). It is worth noticing that w should be narrower than 500 nm in order to provide monomode propagation [Fig. 5.6(a)] but, at the same time, far away from the region around 250-300 nm where backscattering, loss and polarization conversion effects are strong [45]. Furthermore, although athermal operations can be achieved on both polarizations, it is clear that for the same waveguide width TM modes provide lower confinement in the core (and thus a stronger mode sharing with the other layers) than TE, condition that is much desired for the athermal design.

Figure 5.7(a) show simulations of the temperature sensitivity on TM polarization of the proposed waveguide versus wavelength for different waveguide widths and $BaTiO_3$ thicknesses. As w and t are increased the mode expands from the Si core through the $BaTiO_3$ layer and into the TiO_2 upper cladding, providing athermal wavelength at 1550 nm for $w = 400$ nm and $t = 10$ nm (black circle markers and solid line). Also, the dependence from temperature of this waveguide design is about one order of magnitude smaller than that of the non-athermal waveguide (red quare markers and solid line) over a wavelength range of about 60 nm. Also, Fig. 5.7(b) reports the wavelength shift that can be achieved as the refractive index of $BaTiO_3$ is changed for different $BaTiO_3$ thicknesses. The shift that can be achieved increases with the variation in the $BaTiO_3$ index and, given the

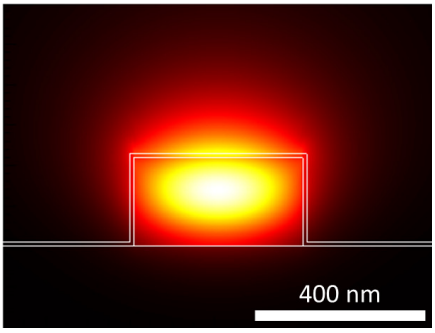

Figure 5.8: *Simulation of the intensity of the TM mode for the athermal and trimmable waveguide with w = 400 nm and t = 10 nm.*

same index change, is larger for thicker $BaTiO_3$ layer. For instance, with an index variation of 0.03 a wavelength shift of about 0.5 nm can be achieved with t = 10 nm, and over 1.5 nm for t = 30 nm. Figure 5.8 reports the simulated intensity of the TM mode of the athermal and trimmable waveguide for w = 400 nm and t = 10 nm. The mode is well distributed between the different layers, with a confinement in the Si core of only 30%.

It is worth noticing that a trade-off between thermal compensation, spectral position of the athermal wavelength, and achievable wavelength shift should be found depending on the applications. Thicker layers of $BaTiO_3$ provide larger trimmability given the same index variation but, at the same time, red-shifts the spectral position of the athermal wavelength, resulting in a higher temperature dependence at the working wavelength. Finally, improved performances can be reached with more advanced waveguide structures, for instance by squeezing the thin trimming layer inside the silicon core [125], and thus having a stronger modal interaction with $BaTiO_3$ and simultaneously the "athermal" layer in direct contact with the waveguide core, or by replacing the SiO_2 undercladding with TiO_2 and having a thicker layer of $BaTiO_3$ on top of the Si core.

5.2 Active stabilization and feedback control

Active stabilization in silicon photonic circuits is typically realized by means of integrated optical actuators such as microheaters (Sec. 2.1) or diode junctions integrated in the waveguides to exploit carrier injection/depletion/accumulation effects [49]. However, active stabilization techniques require the use of feedback loops to locally monitor and continuously set each optical element of the circuit to the desired working point or functionality.

Several approaches have been recently proposed for the active stabilization and control of Si photonics circuits, including microrings and integrated modulators. For instance, the resonant wavelength of Si microrings can be locked to the desired working point by applying dithering signals [25] or homodyne detection schemes [26], and by monitoring the power level [70, 128] or the bit-error-rate [129] of the optical signal. However, all the techniques proposed so far require the use of on-chip or external photodetectors to partially tap the light travelling in the resonator [13]. Though effective on single devices, this approach is not scalable to large scale integration circuits [5,9], where multi-point light tapping would incur in a large amount of optical power wasted for monitoring operation. Furthermore, local feedback control assisted by transparent optical detectors, such as the CLIPP, is envisioned as an enabling tool for the realization of complex and arbitrarily reconfigurable systems-on-a-chip [6, 7, 31].

In the next sections of this chapter, a Si photonic-electronic integrated platform that enables stabilization and feedback control of Si photonics integrated circuits, without the need of tapping any photon from the waveguide, is shown. The status of high quality factor resonators is monitored with the CLIPP, that realizes a fully transparent detector (see Chapter 3 for details) and can be integrated directly inside any photonic circuit, including microrings. The feedback loop, combining the CLIPP read-out system and the microring control functions, is entirely integrated onto an electronic CMOS circuit [130] that is wire-bonded to the Si photonics chip. Advanced functionalities and control operations, such as wavelength tuning, locking, labeling and swapping are demonstrated in a thermally actuated resonator, proving that the presented Si photonic-electronic integrated platform is an efficient and flexible solution for the realization and control of Si photonics circuits hosting many components.

5.2.1 Microring and CLIPP fabrication

Figure 5.9(a) shows a top-view photograph of a microring fabricated in silicon-on-insulator (SOI) technology, where the CLIPP electrodes and the thermal actuator are integrated. The microring is 516 μm long, has 20 μm bending radius, and is realized by a channel waveguide with 480 nm wide and 220 nm thick Si core [Fig. 5.9(b)], patterned by means of electron-beam lithography (see Sec. 3.2 for details) [11]. The waveguide core is buried into a 1 μm thick silicon dioxide (SiO_2) top cladding, that is grown by plasma enhanced chemical vapor deposition (PECVD). On top of it, the metallic NiCr heaters and Au pads of the CLIPP are patterned by lift-off

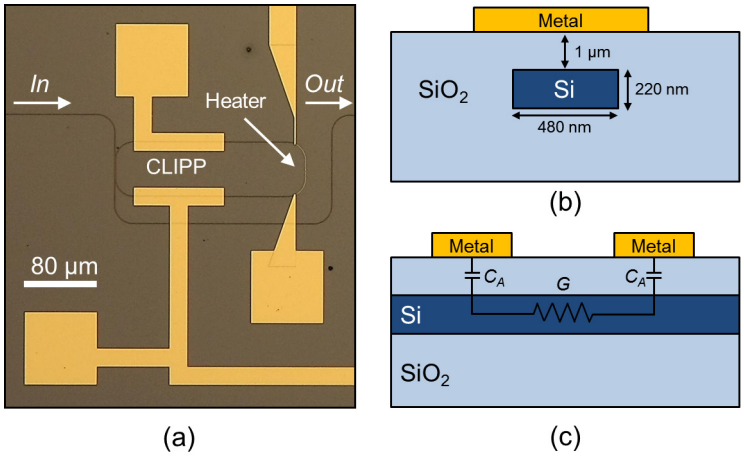

Figure 5.9: *(a) Top-view photograph of the fabricated Si microring, where CLIPP and thermal actuator are integrated. (b) Cross section of the Si core waveguide, with the CLIPP metal electrode deposited on top of the SiO_2 cladding. (c) Longitudinal profile of the Si waveguide showing the CLIPP equivalent circuit in the electrical domain, that is composed of two access capacitances C_A and a resistor of conductance G.*

technique, and placed at sufficient distance from the Si core to avoid any significant absorption of the optical mode by the metal.

As explained in details in Chapter 3, the CLIPP is constituted simply by the two 100 μm long metal electrodes placed on top of the microring waveguide, here mutually spaced by about 83 μm on the side of the bus-to-ring directional coupler. It is worth highlighting again that the CLIPP can be fabricated by using any CMOS-compatible metal technology, and can exploit traditional processes used for the fabrication of thermal actuators, without requiring any additional or specific process step.

For the reader's sake, the equivalent electrical circuit of the CLIPP is reported again in Fig. 5.9(c), that shows the longitudinal profile of the waveguide (stray capacitive coupling to the Si substrate is here neglected, see Sec. 3.6.5 for details). Due to the typical doping of SOI wafers (10^{15} cm^{-3}, p-type) the Si core acts mainly as a resistor of conductance G, whereas the insulating top cladding provides the access capacitances C_A. The CLIPP monitors variations of the waveguide electric conductance ΔG with optical power P, that are induced by a carrier generation effect, occurring at the native Si/SiO_2 interface, associated to intrinsic surface-state-absoption processes [73] (see Chapter 4 for details). These phenomena exist even in ideally smooth interfaces because of the termination of the Si lattice at the walls of the waveguide core [78]. No specific treatment is performed on the

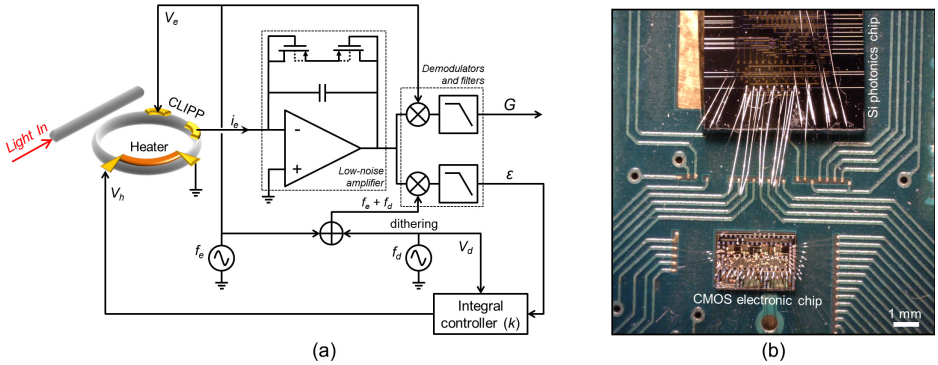

Figure 5.10: *(a) Schematic of the electronic integrated circuit that performs the read-out of the CLIPP electric signal, and manages control operations of the Si photonics microring resonator (such as wavelength tuning, locking, labeling and swapping). (b) Photograph of the Si photonics chip (on the top) hosting the microring resonator, that is wire-bonded to the CMOS electronic chip (in the bottom) containing all the CLIPP read-out and microring control circuitry. Both the photonic and the electronic chips are integrated onto the same printed circuit board.*

Si core surface.

The CLIPP is essentially a non-invasive observer of the local power propagating in an optical waveguide, and therefore can be easily utilized in any applications requiring to monitor the light travelling in a photonic circuit (see Sec. 5.2.3, 5.2.4, and 5.2.5). In addition, it is worth noticing that, thanks to its intrinsic non-perturbative nature, the CLIPP can be placed in any point of the circuit to monitor its local status without affecting its functionality.

5.2.2 The read-out system

The CLIPP observes directly the amount of light stored in the resonant cavity, information that traditionally is not available unless a portion of the optical power is tapped and rerouted to a photodetector, by measuring variations of the electric conductance G of the waveguide core (see Chapter 3).

Read-out operations of the CLIPP electric signal, as well as microring control functionalities (such as wavelength tuning, locking, labeling and swapping), are performed by means of a custom microelectronic circuit [130], whose schematic is shown in Fig. 5.10(a). One of the CLIPP electrodes is excited with a sinuosidal electrical signal, with frequency f_e and amplitude V_e, whereas the current flow i_e at the other one is collected

by means of a low noise amplifier. Then, the CLIPP signal is demodulated at frequency f_e to provide the electric conductance G. The electric read-out frequency of the CLIPP is typically around f_e = 1 MHz in order to bypass the capacitances C_A and access directly the waveguide conductance G, whereas the amplitude of the applied signal is usually V_e = 1 V, so that neither attenuation nor significant perturbation of the optical mode is induced, and without affecting the quality factor of the resonator (see Sec. 3.4 for details). Similarly, the integrated electronic circuit manages control operations of the microring, like wavelength tuning, locking, labeling and swapping, by using the dithering and feedback controller units reported in the schematic (see Sec.5.2.3, 5.2.4, and 5.2.5).

The electronic read-out circuit is integrated in a CMOS chip (0.35 μm process by AMS foundry) with 32 read-out channels, that is wire-bonded to the Si photonics chip hosting the microring resonator (fabricated by the James Watt Nanofabrication Centre at University of Glasgow) [Fig. 5.10(b)]. Both the electronic and the photonic chips are integrated onto the same printed circuit board. This photonic-electronic integrated platform enables to achieve not only improved CLIPP performances (lower noise, lower parasitics, better sensitivity, higher speed etc.) [130], but also offers a simple and flexible system for the realization and control of large scale Si photonics integrated circuits, hosting several components to achieve complex systems-on-chip.

5.2.3 Tuning the microring resonant wavelength

Figure 5.11(a) shows the variations of conductance ΔG induced by the propagation of quasi-transverse electric (TE) polarized light in the resonator, measured by the CLIPP versus wavelength, when the thermal actuator is off (blue line), and then driven with voltage V_h = 2, 3, 4 V (red, green and orange lines). The microring has a linewidth of 51 pm (6.4 GHz), free-spectral-range of 1.115 nm (139.2 GHz), and quality factor of about 30000. Also, the corresponding optical power travelling in the resonator is provided on the rightmost vertical axis, as estimated from the conductance variations measured by the CLIPP (see Sec. 3.3.2 and Fig. 3.2). Any spurious conductance change due to thermal cross-talk effects between CLIPP and heater is here negligible, being more than one order of magnitude smaller than ΔG induced by light at the low power levels utilized in this work.

The effectiveness of the CLIPP to monitor the transfer function of the microring is exploited to automatically tune its resonant wavelength in or-

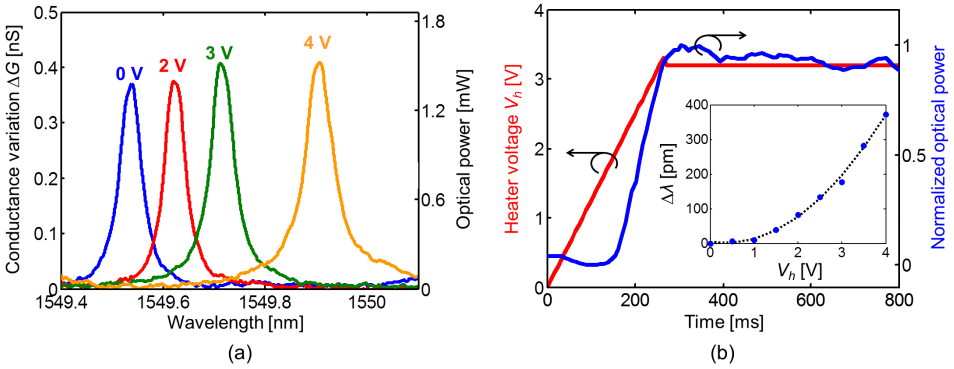

Figure 5.11: *Tuning of the microring resonant wavelength assisted by the CLIPP. (a) Light induced conductance variation ΔG measured by the CLIPP, and corresponding estimated optical power, as a function of wavelength, when the thermal actuator is off (blue line) and then switched on at V_h = 2, 3, 4 V (red, green, and orange lines). (b) Automated tuning of the resonator wavelength to that of an external laser, here detuned by about 230 pm, assisted by the CLIPP; the inset shows the wavelength shift $\Delta\lambda$ measured by the CLIPP as the heater voltage V_h is increased from 0 to 4 V.*

der to overlap with that of an external laser [Fig. 5.11(b)]. The laser wavelength is initially red-shifted with respect to that of the resonator by about 230 pm (4.5 times the ring linewidth), then while the heater voltage V_h is automatically and continuously increased to shift the resonant wavelength (red line) the CLIPP simultaneously monitors the optical intensity stored in the cavity (blue line). The inset of Fig. 5.11(b) shows the CLIPP monitoring the microring resonant wavelength versus the voltage applied to the heater. The tuning process, here achieved in about 260 ms, terminates when the optical power measured by the CLIPP reaches its maximum value, here for V_h = 3.2 V, condition that occurs only when the resonator wavelength is aligned to that of the laser.

5.2.4 Locking the microring resonant wavelength

Here we demonstrate feedback control of the microring by locking its resonant wavelength to that of an external laser. To this aim we utilize the CLIPP to monitor the optical intensity in the microring, and the thermal actuator to adjust its resonant wavelength based on a feedback error signal provided by the CLIPP. In particular, we employ a common dithering technique [25], according to which a small modulation signal is applied to the resonator, and then, by mixing it with the modulated intracavity optical intensity measured by the CLIPP, an error signal is extracted and used to

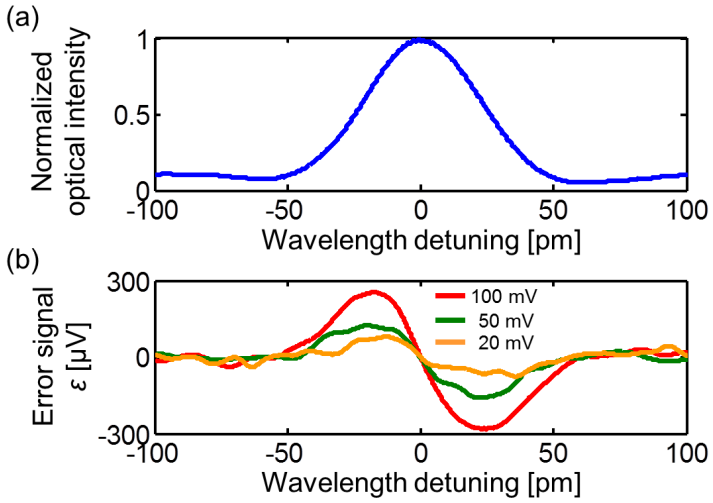

Figure 5.12: *Generation and read-out of the error signal of the feedback-controlled microring. (a) Normalized optical intensity measured by the CLIPP versus wavelength, with V_e = 1 V and f_e = 1 MHz, when a dithering signal with amplitude V_d = 100 mV and frequency f_d = 160 Hz is applied to the heater. (b) Error signal ε extracted by the CLIPP by further demodulating the optical power P at the frequency of the dithering signal f_d for dithering amplitudes V_d = 20, 50, 100 mV.*

drive the feedback loop [as shown in the schematic of Fig. 5.10(a)].

Generation and read-out of the error signal

Figure 5.12(a) shows the optical intensity in the resonator measured by the CLIPP, here low-pass filtered, when a sinusoidal dithering signal with frequency f_d = 160 Hz and amplitude V_d = 100 mV is applied to the heater of the resonator, as in the schematic of Fig. 5.10(a). In addition, a 2 V bias is applied to the heater in order to have the resonant wavelength overlapped to that of the laser. The CLIPP monitors also the corresponding error signal ε [Fig. 5.12(b), red line] by demodulating the resonant optical power at frequency f_e+f_d = 1.00016 MHz. The error signal is zero at the resonant wavelength (λ_r = 1549.54 nm) and maximum on the slope of the resonator ($\lambda_r \pm$ 20 pm). Also, thanks to the antysimmetric shape of ε, no ambiguity is left to what direction λ_r is located. Here, the application of a dithering signal with 100 mV amplitude corresponds to a thermal fluctuation as low as ΔT = 0.14 K (wavelength shift $\Delta\lambda$ = 11 pm corresponding to about 20% of the linewidth), that is in line with those used for tap detectors [25] and does not affect the quality of the transmitted signal [70] . Though small,

the amplitude of V_d can be further reduced to minimize the induced $\Delta\lambda$: in fact, with amplitudes of 50 mV and even 20 mV [Fig. 5.12(b), green and orange lines], corresponding respectively to ΔT = 0.07 K ($\Delta\lambda$ = 5 pm, 10% of the linewidth) and ΔT = 0.03 K ($\Delta\lambda$ = 2 pm, 4% of the linewidth), the error control signal is well above the noise level and can be used to drive the feedback loop.

Implementation of the control loop

In order to have the resonator wavelength λ_r continuously locked to that of an external laser λ_l, the CLIPP monitors simultaneously and continuously the intracavity optical intensity and the level of the error signal ε. As λ_r and λ_l drift apart from each other, the resonant optical power drops and the error signal deviates from zero. Consequently, the voltage applied to the heater is updated with an increment proportional to ε, its sign indicating the direction to follow (heating or cooling), and thus restoring the alignment between λ_r and λ_l.

The feedback loop is implemented by means of an integral controller, whose gain k depends on the magnitude of ε with respect to the wavelength detuning $\Delta\lambda$ [Fig. 5.12(b)], and on the wavelength shift that the heater can achieve [inset of Fig. 5.11(b)]. According to our model, k should be sufficiently high to achieve fast response of the feedback loop, but, at the same time, low enough to guarantee stability of the system. As an example, considering that $\Delta\varepsilon/\Delta\lambda$ = 15 μV/pm around the resonant wavelength when V_d = 100 mV, and that the heater shifts λ_r by about 95 pm/V around 2 V bias, a controller gain around k = 10000 is sufficient to provide a loop response as low as 50 ms, while maintaining the system stability according to the Bode criterion. Here, the controller is implemented by means of a programmable digital platform (FPGA), thus allowing more speed and flexibility in setting the controller parameters with respect to computer-assisted architectures.

Testing the control loop

The feedback loop is here tested against external fluctuations of the laser wavelength. Figure 5.13 shows the optical intensity in the microring, measured by the CLIPP as a function of time, when the feeback routine is on (blue lines) and off (red lines), in presence of a detuning of λ_l by 50 pm (about the same of the resonator linewidth, and corresponding to a temperature variation of 0.7 K), i.e. approximately at the edges of its full linewidth. In Fig. 5.13(a) an instantaneous wavelength shift is imposed by the laser:

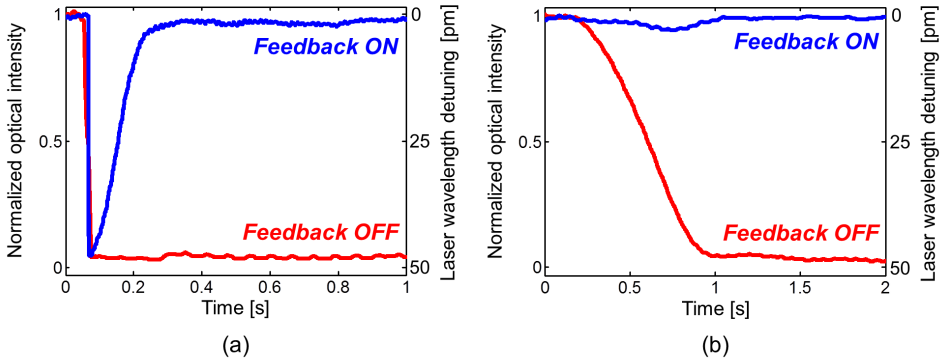

Figure 5.13: *Locking the microring resonant wavelength to that of an external laser λ_l assisted by the CLIPP. Normalized optical intensity in the resonator measured by the CLIPP when the feedback control is on (blue lines) and off (red lines) in presence of (a) an istantaneous wavelength shift and (b) a continuous wavelength sweep (here occurring in about 700 ms) of the external laser by 50 pm (corresponding to 98% of the resonator linewidth, that is the same of a temperature variation of 0.7 K).*

the optical intensity in the resonator drops as λ_l is changed, but then is rapidly brought back (here in about 150 ms) to its initial level (where λ_l and λ_r overlap) by the feedback loop (blue line). In Fig. 5.13(b), instead, the feedback loop compensates for a continuous wavelength sweep of the laser: no significant variation in the resonant optical intensity is observed (blue line) along the entire wavelength detuning (here occurring in about 700 ms), having λ_l and λ_r always locked one to another by the feedback control. The beneficial effect of the feedback loop is confirmed when the control is switched off (red lines): in fact in both cases, as λ_l shifts, the optical intensity in the resonator drops and is never compensated, having the laser wavelength completely outside of the resonator linewidth.

Although the speed of the control loop here achieved is enough to well counteract most of the drifts (thermal and others) experienced by Si photonics microrings, it can be significantly increased either with suitable control laws (such as proportional or proportional-integral) or by enlarging the CLIPP read-out bandwidth. For instance, while keeping the current CLIPP bandwidth (around 1 kHz), if a proportional controller with gain of few thousands is utilized, a loop with time constant down to hundreds of μs is achieved, yet at the price of larger voltage variations at the thermal actuator. On the other side, while maintaining an integral controller, the loop frequency can be increased by using a larger CLIPP bandwidth, yet at the price of larger noise (though typically depending on the square root of the

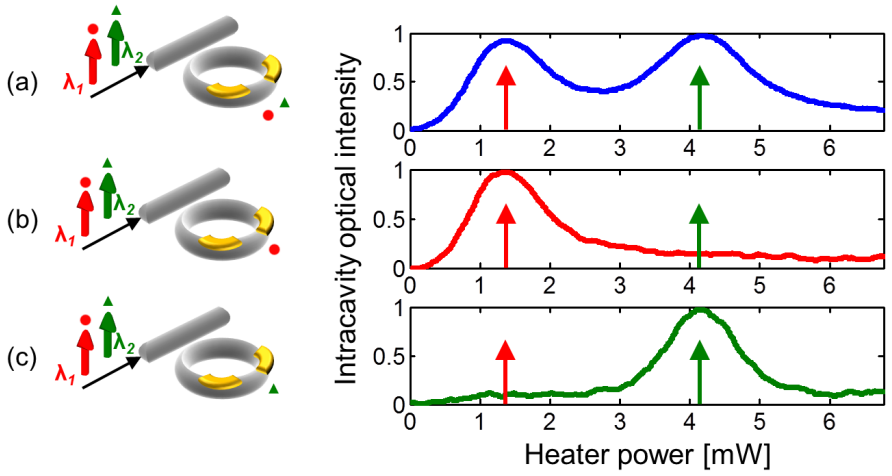

Figure 5.14: *Swapping the resonator wavelength between two optical signals at wavelengths λ_1 (red arrow) and λ_2 (green arrow) injected in the microring. A weak modulation tone with depth 2% is added to label each of the optical carriers: the tone centered on λ_1 has frequency f_1 = 10 kHz (labeled with a red circle), whereas the tone around λ_2 has frequency f_2 = 11 kHz (labeled with a green triangle). The optical intensity measured by the CLIPP in the resonator is reported as a function of the electrical power dissipated on the heater when the CLIPP signal is demodulated at frequencies (a) f_e = 1 MHz, (b) f_e+f_1 = 1.010 MHz, (c) f_e+f_2 = 1.011 MHz. When demodulating the CLIPP signal at frequency f_e, the signals λ_1 and λ_2 are indistinguishable; in constrast, when read-out operations are performed at frequency f_e+f_1 (f_e+f_2) the CLIPP is able to identify distinctively λ_1 (λ_2).*

bandwidth).

5.2.5 Swapping the microring resonant wavelength

Although the CLIPP is in general a broadband light observer, here we show that it is able to monitor and discriminate simultaneously optical signals at different wavelengths. To this aim we inject in the microring two different signals with wavelengths λ_1 = 1549.59 nm and $\lambda_2 = \lambda_1$ + 120 pm, labeled respectively with red and green arrows in Fig. 5.14. A weak modulation tone, with depth 2%, is added to label each of the optical carriers by means of an external modulator. The tone centered around λ_1 has frequency f_1 = 10 kHz, whereas the other one, that is centered around λ_2, has frequency f_2 = 11 kHz (the tones are labeled respectively with red circle and green triangle in Fig. 5.14). The optical intensity observed in the resonator by the CLIPP is shown in Fig. 5.14 as a function of the electrical power dissipated by the heater. When the CLIPP electrical signal is demodulated at the usual

frequency f_e = 1 MHz, the intracavity optical intensity reports two peaks associated to the transmission of both signals λ_1 and λ_2 [blue line in Fig. 5.14(a)], that are therefore indistinguishable. Vice versa, if the read-out operations are performed at frequency f_e+f_1 = 1.010 MHz, the CLIPP is able to identify the signal at λ_1, where the modulation tone at frequency f_1 is added. In fact, as shown in Fig. 5.14(b) with red line, the resonant peak measured by the CLIPP is centered on the first signal (red arrow), whereas no evidence of λ_2 is found (green arrow). Similarly, if the electric signal is demodulated at frequency f_e+f_2 = 1.011 MHz, the measured resonant peak is centered on the second signal (green arrow), that is identified by the CLIPP as wavelength λ_2. It is straightforward now to tune and lock the microring resonant wavelength to that of the first signal λ_1 (λ_2), and then easily swap it to that of the second signal λ_2 (λ_1). Furthermore, it is worth noticing that wavelength swapping operations can be performed by the CLIPP simultaneously on an arbitrarily large number of wavelengths by using several modulation tones and by suitably demodulating the different signals, on signals at the same wavelength but different light polarizations (see Sec. 3.6.2), and on higher order modes in waveguides exploiting mode-division multiplexing schemes [131].

5.3 Fiber-to-waveguide coupling assisted by the CLIPP

The final Section of this Chapter is dedicated to an important application of the CLIPP and feedback loops, that is to assist fiber-to-waveguide coupling procedures. Alhough this topic slightly differs from the applications previously encountered in this Chapter, it is indeed well suited within a larger discussion on circuit stabilization and feedback loop control.

Fast, efficient and low-cost fiber-to-waveguide alignment is a key issue for testing and packaging of photonic integrated circuits. Typically, traditional active fiber-to-waveguide coupling techniques require to have two optical fibers simultaneously aligned to the integrated waveguide [132], one on the side of the laser, the other on the side of the photodetector [Fig. 5.15(a)]. Only when the positions of both fibers are optimized the maximum optical power level is collected at the output by the photodetector.

Besides being inherently a complex task (because of the two degrees of freedom that are the positions of the fibers), this situation presents a significant drawback which may limit its use in practical applications. In fact, the power collected by the output fiber and by the photodetector is affected by the "health status", topology, and complexity of the circuits that are hosted on the photonic chip and that light passes through to reach the output facet.

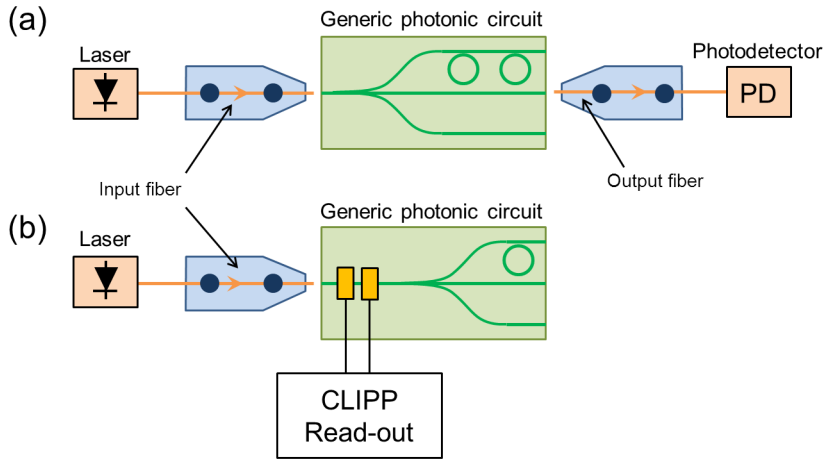

Figure 5.15: *(a) Traditional schematic for active fiber-to-waveguide coupling: two optical fibers have to be simultaneously aligned to the integrated waveguide respectively at the chip input and output facets. (b) Schematic of the fiber-to-waveguide alignment assisted by the CLIPP: only one fiber is aligned at a time, so that first the position of the input fiber is optimized, then that of the output fiber (if necessary). This technique is compatible with both butt-coupling schemes and those requiring grating couplers.*

For instance, if the light that is coupled on the chip travels across a complex circuit composed of several components, or propagates along a lossy waveguide, this will lower the power received by the photodetector, making the alignment process more difficult.

For this reason, passive alignment techniques, that do not require the light to travel across the chip, are preferred [133]. The CLIPP offers a significant advantage to the fiber-to-waveguide coupling problem because it enables to perform the process by aligning only one fiber at a time [Fig. 5.15(b)]. In fact, by placing the CLIPP in proximity of the chip facet, the signal measured by the CLIPP as the input fiber position is changed will help to optimize the position of the fiber itself. It is straightforward to notice that, as shown in Fig. 5.15(b), the electric signal measured by the CLIPP is not affected by the circuit that is hosted on the chip after the CLIPP, and thus the fiber-to-waveguide alignment can be achieved regardless of the circuit hosted on the chip. Furthermore, it is worth noticing that, after the fiber position is optimized, the CLIPP presence can be neglected, being intrinsically a transparent component (see Sec. 3.4).

The effectiveness of this technique is shown in Fig. 5.16, where the CLIPP assists the alignment of a tapered lensed fiber, with a 1.7 μm mode-field-diameter, to a silicon photonic integrated waveguide with width 1 μm

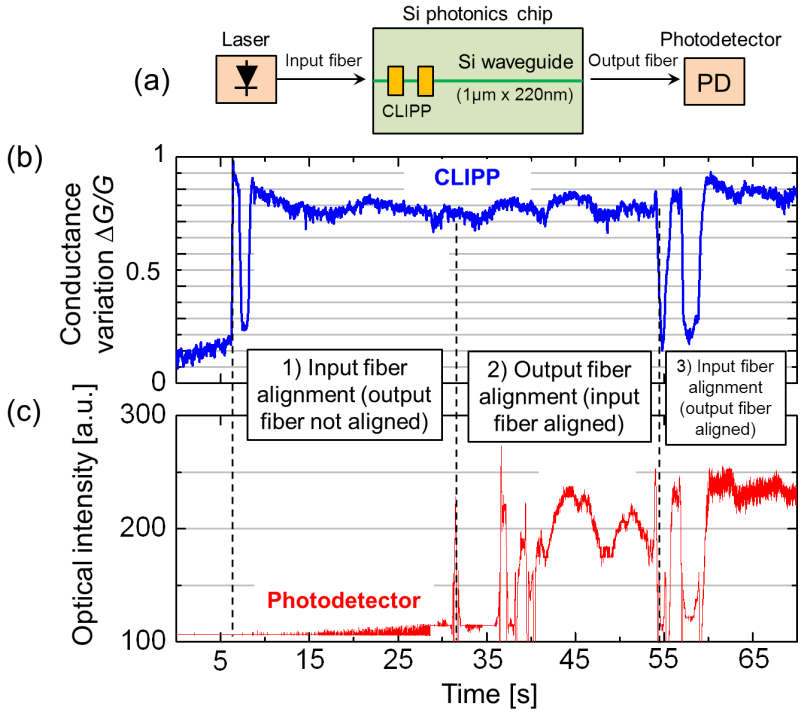

Figure 5.16: *(a) Experimental setup utilized to compare the alignment process assisted by the CLIPP and by a conventional external photodetector. Signal measured by the (b) CLIPP and by the (c) photodetector as the input and output fiber positions are changed. Here tapered lensed fibers with a 1.7 μm mode-field-diameter are utilized.*

and thickness 220 nm (same technology and fabrication process described in Sec. 3.2). The CLIPP is placed in proximity of the chip facet [Fig. 5.16(a)], with the 100 μm long metal contacts at a distance of 100 μm. Here, while the positions of the input and output fibers are changed to optimize the alignment with the integrated waveguide, the light intensity coupled into the waveguide is measured simultaneously with the CLIPP [Fig. 5.16(b)] and with an external photodetector [Fig. 5.16(c)] placed at the output facet of the chip. First, the position of the input fiber is optimized in order to maximize the signal measured by the CLIPP (panel 1). When the CLIPP signal is maximum the position of the input fiber is well aligned to that of the waveguide, however the optical intensity collected at the output by the photodetector is low, being the output fiber misaligned with respect to the photonic waveguide. The signal measured by the photodetector increases when also the output fiber position is changed, and reaches its

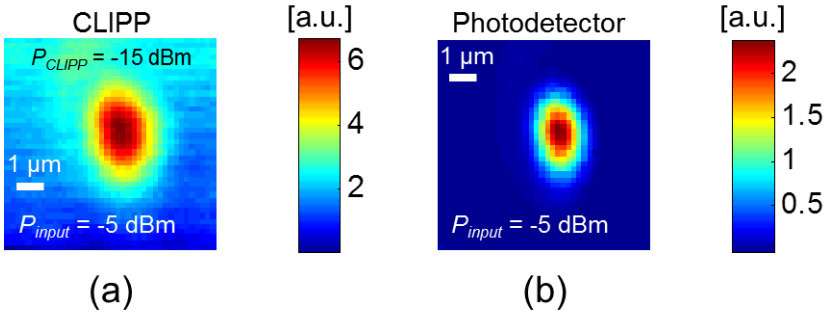

Figure 5.17: *Spatial distribution of light across the Si waveguide structure (in a plane parallel to the chip facet), in a 8 µm × 8 µm area, measured (a) by the CLIPP and (b) by the external photodetector. Each pixel has 200 nm × 200 nm size. The Si waveguide core has size 1 µm × 220 nm.*

maximum only when is optimized (panel 2). It is worth noticing that, in the condition of panel 2, that is when the output fiber position is changed, the signal measured by the CLIPP does not vary, since it is not affected by "what happens" after the CLIPP (that is the circuit health status and the position of the output fiber). Finally, as shown in panel 3, when both fibers are well aligned to the integrated waveguide, if the input fiber position is changed from the optimal position, both the CLIPP and the photodetector signals fluctuate in the same way, that is when one increases (decreases) the other does as well.

The suitability of the CLIPP to assist the fiber-to-waveguide alignment process is further confirmed by the maps shown in Fig. 5.17, where the spatial distribution of light measured by the CLIPP is compared to that collected by an external photodetector at the output of the chip [same experimental setup of Fig. 5.16(a)]. Here, the position of the input fiber is swept across the horizontal and vertical coordinates (in a plane parallel to the chip facet) in a square region of 8 μm × 8 μm around the waveguide with steps of 200 nm, whereas the output fiber is fixed to the optimal position in order to allow the best coupling with the external photodetector. The input power is here -5 dBm, providing a local light intensity of about -15 dBm in the CLIPP. From a qualitative point of view, it is straightforward to notice that there is an excellent agreement between the distribution measured by the CLIPP and that provided by the photodetector. In fact, the maximum of both signals, that represents the waveguide center where light intensity is maximum, is observed in the same position of the considered area, and then decreases toward the outer regions of the waveguide.

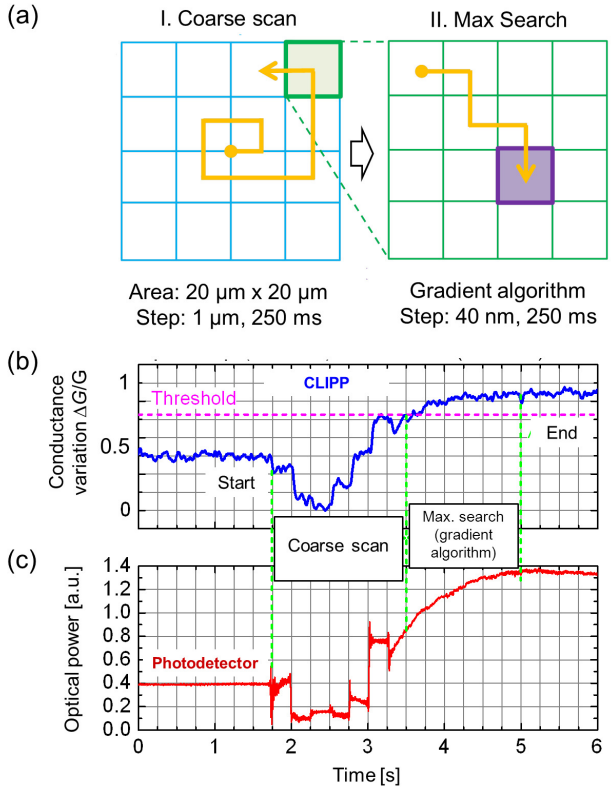

Figure 5.18: *Automated fiber-to-waveguide coupling. (a) Schematic representation of the automated alignment performed through an initial coarse scan of the input fiber position, and then with a gradient algorithm enabling to reach quickly the optimal fiber position. Signal measured (b) by the CLIPP and (c) by the external photodetector during the automated alignment process, that here is achieved in about 3 s.*

Finally, the CLIPP-assisted fiber-to-waveguide coupling process can be performed automatically with a feedback loop in order to achieve optimal alignment on a time scale of only few seconds. According to the routine that is schematically reported in Fig. 5.18(a), initially the input fiber is swept across a large area around the waveguide center, then when a certain threshold is exceeded by the CLIPP signal a gradient algorithm is applied in order to maximize the power coupled in the waveguide. Here, by performing the initial coarse scan across a region of 20 μm $\times$ 20 μm with steps of 1 μm, and then by applying a gradient algorithm with steps of 40 nm, the optimal coupling position is reached in about 3 s, having chosen a step time of 250 ms. This is shown in Fig. 5.18(b) and (c) that report respectively the signal measured by the CLIPP and by the photodetector as the input fiber

reaches its optimal position.

In conclusion, the CLIPP offers an efficient solution to assist fiber-to-waveguide alignment processes that are essential for testing and packaging of photonic integrated circuits. With respect to active techniques, light coupling assisted by the CLIPP requires the use of only one optical fiber, thus reducing significantly their complexity. The procedure, that here is achieved in about 3 s, can be further speeded up by using advanced optimization algorithms. Finally, fiber-to-waveguide alignment with the CLIPP can be extended to other semiconductor technologies, such as indium phosphide, where the CLIPP operation was demonstrated (see Sec. 3.7).

CHAPTER 6

Toward complex systems-on-chip

Recently, new terms and concepts, such as reconfiguration, adaptability, stabilization and control, have appeared in integrated optics, and are currently becoming paradigms for the silicon photonics platform. In particular, the delivery of advanced [7] and arbitrary functionalities [6] is highly desired for large scale integration circuits, and represents a fundamental step to make photonics leap away from a device level to a newer systems-on-chip paradigm [5].

This Chapter discusses issues such as reconfigurability and adaptability through examples of complex PICs, whose operation and functionalities are enabled by the devices and technologies developed in the previous Sections of this thesis, that are the CLIPP, power-saving actuators, stabilization, and feedback control. Sections 6.1 and 6.2 show respectively transfer function recovery and reconfiguration of high-order coupled resonator optical waveguide (CROW) filters and delay lines [134]. These functionalities, that are here presented in an As_2S_3 platform and are enabled by low-power photo-induced trimming, are more general and apply to other technologies. In fact, similar functionalities are shown also for the silicon platform in Sec. 6.3, where the CLIPP assists the thermo-optic tuning of a CROW. Finally, in Sec. 6.4 a variable symbol-rate differential phase-shift keying (DPSK)

receiver is discussed, focusing on the tuning and reconfiguration of the device, adaptability to the input symbol-rate, and stabilization and robustness to thermal and nonlinear effects.

6.1 Transfer function recovery of high-order filters

Photo-induced trimming, that was analyzed in details in Sec. 2.2, is here utilized to recover the transfer function of 2^{nd}- and 4^{th}-order CROWs in As_2S_3 technology, whose reponse is completely distorted by the unavoidable fabrication tolerances. This result can be applied directly to silicon photonics devices employing the As_2S_3-assisted design (see Sec. 2.2.2).

Coupled-resonator structures were realized in As_2S_3 core waveguides [cross-section shown in Fig. 2.3(a) and fabrication details in 2.2.1] by cascading identical coupled ring-resonators with 100 μm bending radius and 350×200 μm^2 footprint, providing a free spectral range *FSR* = 130 GHz (i.e. 1.04 nm). The ring-to-ring coupling sections have a gap distance of 700 nm and are optimized by laterally shifting the rings.

Cascaded resonators coupled to two bus waveguides, such as those shown in Fig. 6.1(a_1), are suitable structures for realizing high-order bandpass filters [134], provided that all the rings resonate at the same resonant wavelength. Fig. 6.1(a_2) shows the frequency domain transmission of a two-ring As_2S_3 filter at the Drop port for TM input polarization. Black dashed line refers to the filter as fabricated, that is before any light exposure treatment. Because of fabrication tolerances, the mismatch of the resonance wavelengths λ_{R_i} (i being the ring number), that are shifted by about 0.35 nm, severely distorts the response from the desired flat top passband.

To recover the desired transfer function, the resonance spread was compensated by individually trimming the resonances λ_{R_i} to the same wavelength λ_0 = 1523.2 nm with the technique described in Sec. 2.2.1 and 2.2.2. After light exposure the measured transmission of the filter [blue solid line in Fig. 6.1(a_2)] is nicely flat with an extinction ratio as high as 20 dB and linewidth of 32.5 GHz.

Then, once the desired spectral response was recovered, photosensitivity was further exploited to finely adjust the operation wavelength of the filter. By simultaneously exposing both resonators to visible light, as shown in Fig. 6.1(b_1), the transfer function of the device can be rigidly red-shifted. For instance, Fig. 6.1(b_2) shows the trimming of the transfer function of the filter across an entire *FSR* (from blue dashed line to red solid line), here achieved in less than 4 minutes of exposure.

Then, the same approach is employed to recover the transfer function

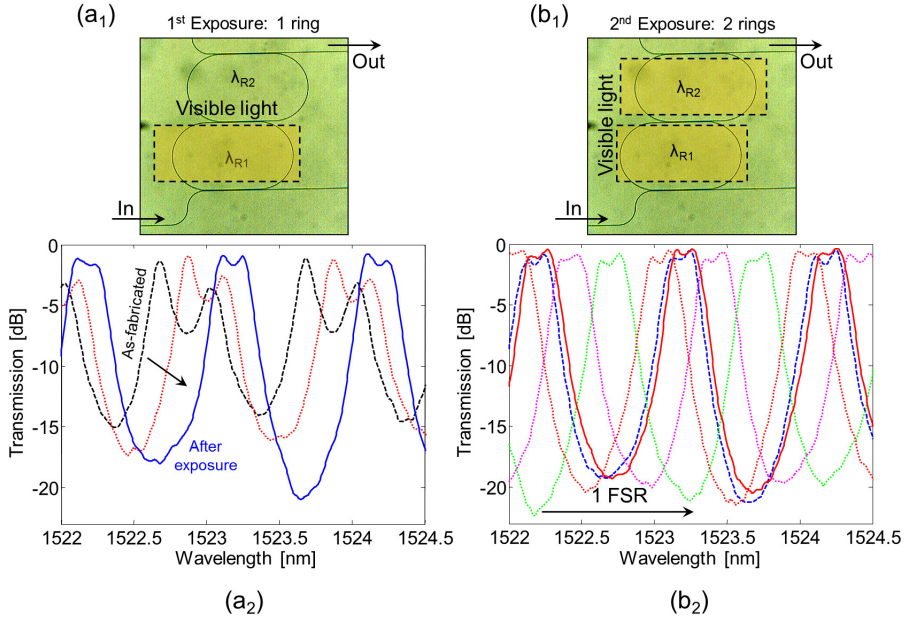

Figure 6.1: *(a_1)-(a_2) Transfer function recovery and (a_1)-(a_2) wavelength trimming of a two coupled ring resonator filter realized in As_2S_3 chalcogenide waveguides. Exposure of one microring enables to compensate for the spectral mismatch of the two resonances (λ_{R_1} and λ_{R_2}), whereas illumination of both resonators rigidly red-shifts the response of the device.*

of an even more complex filter, that is composed of 4 coupled microring resonators [Fig. 6.2(a)]. The frequency domain transmission of the four-ring As_2S_3 structure is shown in Fig. 6.2(b) and (c) at both Through (b) and Drop (c) ports for TM input polarization. The ring-to-ring power coupling coefficients are $\{0.26, 0.20, 0.26\}$, while the ring to bus coupling is 0.57. Black dotted lines refer to the filter as fabricated. Here, the effect of fabrication tolerances is even more severe, and the spectral response is so distorted that no light is transmitted to the Drop port [Fig. 6.2(c)].

After individually trimming each resonator by means of light exposure, the measured transmission of the filter [red and blue solid lines in Fig. 6.2(a) and (b)] is in a very good agreement with the theoretical curves (red and blue dashed lines). At the Drop port the filter exhibits almost flat pass-bands with a bandwidth B = 35 GHz and with more than 23 dB extinction ratio. The insertion loss at the transmission maxima is about 8 dB, corresponding to an average loss figure of 2 dB/ring. The residual $\pm$2 dB in-band ripple is due to deviations from the designed coupling ratios, resulting in an

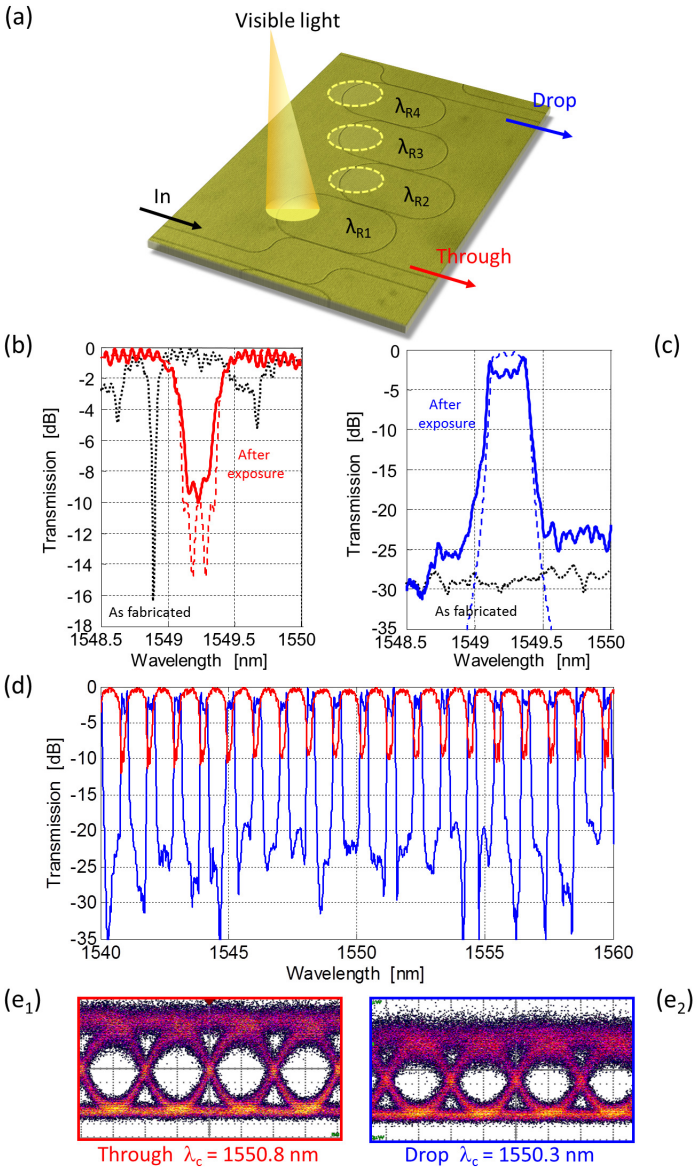

Figure 6.2: *(a) Top-view photograph of the fabricated 4-ring As_2S_3 filter, the technique employed to recover its transfer function is also shown. Normalized spectral response of the device at the (b) Through and (c) Drop ports: measurement before (dotted lines) and after (solid lines) photo-induced trimming are compared with theoretical curves (dashed lines). (d) Measured response at Through (red) and Drop (blue) ports over a 20 nm wide wavelength range. (e) Eye diagrams of a 10 Gbit/s OOK signal at the (e_1) Through port (λ_c = 1550.8 nm) and (e_2) Drop ports (λ_c =1550.3 nm).*

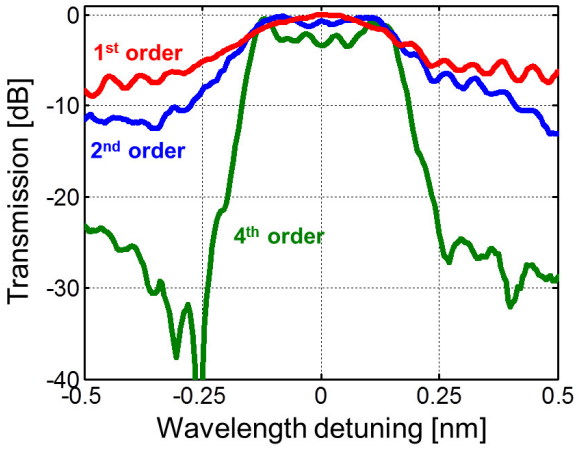

Figure 6.3: *Transmission at the Drop port of As_2S_3 coupled resonator filters composed of N = 1, 2, 4 resonators. For larger N the linewidth of the filter narrows and the extinction ratio increases providing nice filtering passbands.*

imperfect apodization of the device. At the Through port, the in-band return loss is nearly as high as 10 dB. As shown in Fig. 6.2(d), these properties are maintained over a wavelength range larger than 20 nm, except for a 17% increase in the bandwidth due to the wavelength sensitivity of the directional couplers.

The system performance of the trimmed filter was evaluated through the transmission of a 10 Gbit/s intensity modulated on-off keying (OOK) signal (2^7-1 pseudorandom bit sequence). Fig. 6.2(e_1) shows the measured eye diagram at the Through port when the carrier wavelength λ_c = 1550.8 nm is out of the band of the filter, that is when the light signal propagates in the bus waveguide only. When the signal spectrum lies within a passband of the filter ($\lambda_c = \lambda_0 = 1550.3$ nm), the signal is transmitted to the Drop port. As shown by the eye diagram of Fig. 6.2(e_2), despite a slightly higher optical noise level, which is essentially due to the higher insertion loss, no significant distortion is observed in the dropped signal, proving the effectiveness of the trimming procedure.

The time stability of the trimming process was checked by storing the devices in the dark for several weeks after light exposure. Measurements performed after the storage period revealed that the shape of the frequency domain response was well preserved, and neither distortions nor time drifts occurred in the eye-diagrams. The only relaxation effect observed was a slight rigid shift of the spectrum, that can be easily counteracted by keeping

the whole chip at a controlled temperature.

Moreover, Fig. 6.3 shows the normalized transmission of As_2S_3 CROW filters of increasing order, that is with an increasing number of coupled resonators N = 1, 2, 4 (respectively in red, blue and green line). As the number of resonators increases the linewidth of the filter narrows resulting in a sharper transmission passband. Also, higher order filters provide a larger off-band extinction ratio, that is smaller than 10 dB for N = 1, about 13 dB for N = 2, and larger than 30 dB for N = 4, this proving the effectiveness of CROWs to realize flat and sharp filters.

Finally, it is worth noticing that by placing CLIPPs in strategic points of these circuits (such as for instance inside the microrings to monitor the optical power stored in the cavities) transfer function recovery and trimming/-tuning procedures can be performed more easily by locally monitoring each single resonator instead of the whole chain (see Sec. 6.3).

6.2 Reconfiguration of high-order delay lines

Photo-induced trimming is here exploited to demonstrate a permanent reconfiguration of As_2S_3 coupled ring-resonator structures. A reconfigurable delay line was fabricated according to the sketches of Fig. 6.4, where only one bus waveguide is coupled to the rings chain. As described in [135], a light signal can propagate through the structure only if its carrier wavelength matches the resonant wavelength of the rings, that is if $\lambda_{R_i} = \lambda_c$. The first off-resonant ring reflects the signal which back-propagates towards the output port, the overall delay linearly increasing with the number N of on-resonance rings.

Figure 6.4 shows transmission experiments through a four-ring delay-line, with bandwidth B = 50 GHz, ring-to-ring power coupling coefficients $\{0.47, 0.35, 0.33\}$, and coupling coefficient 0.71 between the bus waveguide and the first ring. The reference eye diagram of Fig. 6.4(b_1) is measured in the case of minimum delay, occurring when all the rings are off-resonance ($\lambda_{R_i} \neq \lambda_c$ and N = 0) and the light signal propagates in the bus waveguide only. The delay is then set to a higher value by selectively trimming the resonance of an increasing number N of rings. For example, Fig. 6.4(b_2) and Fig. 6.4(b_3) show the eye-diagram delayed by 32 ps and 53 ps, when the first three and four rings resonate at λ_c, respectively. As in thermally actuated architectures [135], the delay can be adjusted continuously between the minimum (N = 0) and the maximum (N = 4) value. Once the desired delay has been set, the visible light source is switched off and the structure holds the selected delay with no need for any powered actuator.

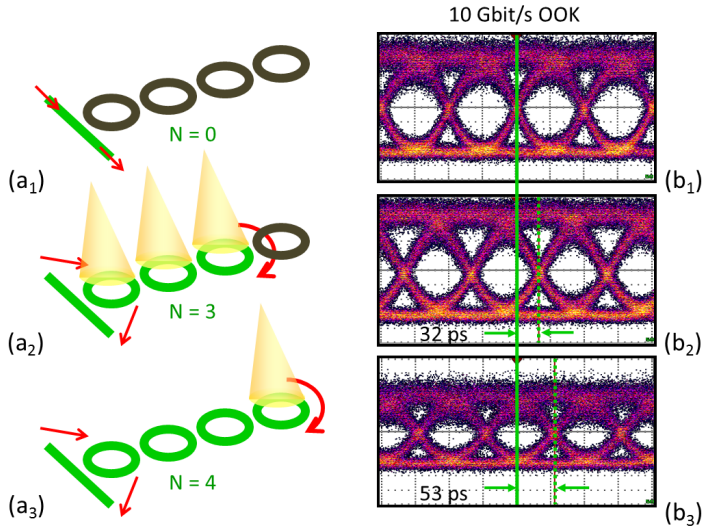

Figure 6.4: *(a) Reconfiguration of a coupled resonator reconfigurable delay line by means of photo-induced trimming. (b) Eye-diagrams of a 10 Gbit/s OOK signal transmitted through a four-ring As_2S_3 delay-line when the number N of on-resonance rings is set to (b_1) N = 0, reference delay; (b_2) N = 3, 32 ps delay; and (b_3) N = 4, 53 ps delay.*

6.3 Local monitoring of complex filters

Transfer function recovery, trimming/tuning and reconfiguration of complex circuits, such as high-order filters or delay lines, can be performed more easily by placing CLIPPs in relevant and strategic regions of the circuit. Here, we show this concept by tuning a silicon CROW composed of two directly coupled racetrack resonators.

Figure 6.5(a) shows a top-view microphotograph of the fabricated device. The two resonators have the same geometric length $L_r = 644$ μm, resulting in a *FSR* of about 860 pm. The power coupling coefficient between the resonators is 0.05, while the coupling between the bus waveguides and the rings is 0.1. Thermal actuators are placed on the waveguide of each resonator to independently tune their resonances. (Details on the waveguide and CLIPP technologies can be found in Sec. 3.2, whereas additional information about the heaters in Sec. 2.1). CLIPPs are positioned on the Through port and inside each resonator to monitor the light power in each relevant portion of the circuit.

In order to show the accuracy of the CLIPP-assisted monitoring and tuning approach, the electric signal $\Delta G/G$ measured by the CLIPP located at the Through port of the circuit [Fig. 6.5(b)] is directly compared to the

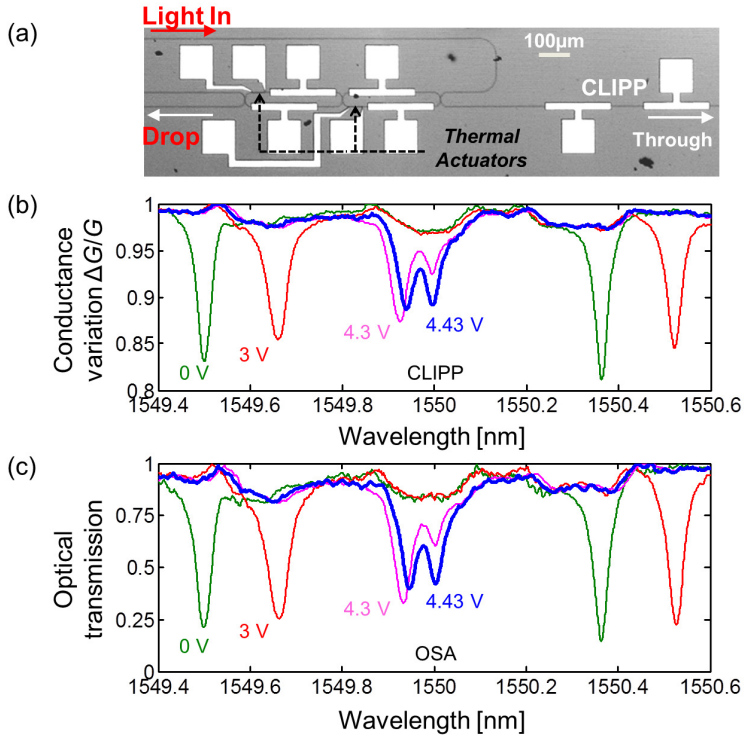

Figure 6.5: *Layout of the two-ring filter with CLIPPs placed at the Through port and inside the ring resonators, and with thermal actuators enabling to adjust the resonance of each ring. (b) Normalized conductance $\Delta G/G$ measured by the CLIPP (driving voltage V_e = 1 V and frequency f_e = 2 MHz) placed at the Through port for different voltage applied by the thermal actuator. (c) Optical transmission measured at the Through port by a conventional OSA for different voltage applied to the thermal actuator.*

optical signal acquired at the same output port by using a conventional optical-spectrum-anlyzer (OSA) [Fig. 6.5(c)]. The two signals were simultaneously acquired for several tuning configurations of the device. In Fig. 6.5(b)-(c), green dashed lines show the transmission spectrum when thermal actuators are switched off (0 V). Even though the two resonators are nominally identical, due to fabrication tolerances the two resonant frequencies are shifted by about half *FSR*, the resonance of the first resonator (the one coupled to the input bus waveguide) being around 1549.45 nm, while the resonance of the second resonator being around 1550 nm. Starting from this condition, the heater placed on the first resonator is switched on to align the resonant frequency to that of the other resonator. When the voltage is increased from 0 V to 4.43 V, the resonance mismatch is ther-

mally compensated and the two ring resonances overlap (blue solid lines). An excellent agreement is found between the CLIPP response and OSA reference spectrum for any tuning condition of the device.

This result demonstrates that the CLIPP can be effectively used to monitor the working point of a generic photonic integrated circuit, regardless of the presence of other cascaded devices. Information on individual device operation reduces the complexity of tuning algorithms, that would become prohibitive when a large number of devices are integrated in a complex architecture. Furthermore, the operation of the circuit can be locked to the desired working point by using feedback control loops, as discussed in Sec. 5.2.4.

6.4 Adaptive functionalities: a variable DPSK receiver

This Section analyzes an integrated variable symbol-rate DPSK receiver in silicon photonics, based on coupled resonator delay line. This structure provides an ideal platform to discuss issues of tuning, stabilization, reconfigurability and adaptability in a complex high-order silicon PIC.

DPSK optical transmission systems offer several advantages over on-off keying (OOK) systems in terms of tolerance to fiber chromatic dispersion and nonlinearities, increased robustness to narrow optical filtering, and 3-dB improvement of the receiver sensitivity when combined with balanced detection [136]. Direct-detection of DPSK signals requires the conversion of phase modulation to intensity modulation, which is usually performed by means of Mach-Zehnder interferometers with a fixed delay equal to the inverse of the signal symbol rate (e.g. 100 ps delay at 10 Gsym/s) [137]. However, the detection of DPSK signals affected by bandwidth-narrowing due to concatenated filters [138] or by chromatic dispersion [139] may be improved if the delay at the receiver deviates from the one-symbol delay. Furthermore, receivers capable of demodulating signals at variable symbol-rates would better fulfill the requirements of optical communication systems, which are evolving toward gridless schemes with higher channel flexibility and dynamic bandwidth allocation [140].

A possible approach is to use constant-delay microring resonators as DPSK receivers, which have been demonstrated to be more robust to symbol-rate variations compared to constant-delay MZI receivers [141]. However, in these schemes some power penalty is inherently observed when the symbol rate deviates from the optimum value. Therefore, variable delay DPSK receivers have been attracting an increasing interest. Several solutions have been proposed in free-space [142] and optical fiber [143]

technologies: however, while offering large delay tunability and good optical performance, these devices are bulky and expensive. An integrated solution for an interferometer with adaptive delay has been realized by using cascaded MZIs [144], yet this device provides only a discrete switching between three delays. More recently Suzuki et al. have demonstrated an integrated silicon photonics differential quadrature PSK (DQPSK) receiver, where the delay can be varied through an all-pass microring slow-light architecture [145]. In this device, tunability from 7.4 to 9 Gsym/s was achieved by individually controlling the resonance of 10 microring resonators.

Here a simpler approach is demonstrated to realize an integrated variable symbol-rate receiver for DPSK optical systems. The variable delay is obtained by means of a CROW (such as that of Sec. 6.2) inserted in one arm of a conventional unbalanced MZI. The fabricated device is realized in SOI technology and can be tuned to optimally detect DPSK signals at any symbol rates between 9.8 and 15 Gsym/s.

6.4.1 Device concept

As shown in the schematic of Fig. 6.6(a), the proposed device consists of an unbalanced MZI with a tunable delay line coupled with the longer arm of the interferometer. The delay line, consisting of a tunable CROW in reflective configuration, is used to modify the mutual delay between the two arms of the MZI in order to adapt the receiver bandwidth to the symbol rate of the incoming DPSK signal. Figure 6.6(a) shows the case of a MZI coupled with a three-ring CROW, but the proposed concept applies to an arbitrary number of resonators.

The working principle of a tunable CROW delay-line was already discussed in Sec. 6.2 and is here briefly summarized referring to Fig. 6.6(b). If the bandwidth of the incoming signal, that is assumed to be centered at wavelength λ_{in}, does not match the transmission bandwidth B of the CROW, the signal is not coupled to the CROW and propagates in the bus waveguide only. In these conditions, the relative delay between the MZI arms is minimum and provides the maximum attainable free spectral range $FSR_{max} = c/(n_g \Delta L_{MZI})$ of the receiver, where ΔL_{MZI} is the geometric unbalance between the two arms of the MZI, c is the vacuum light speed and n_g is the waveguide group index. The delay provided by the CROW can be increased by setting the resonant wavelength λ_{R_i} of an increasing number M of adjacent resonators to λ_{in}. In a CROW with identical resonators with the same coupling coefficients K_{R_i}, each ring provides a delay

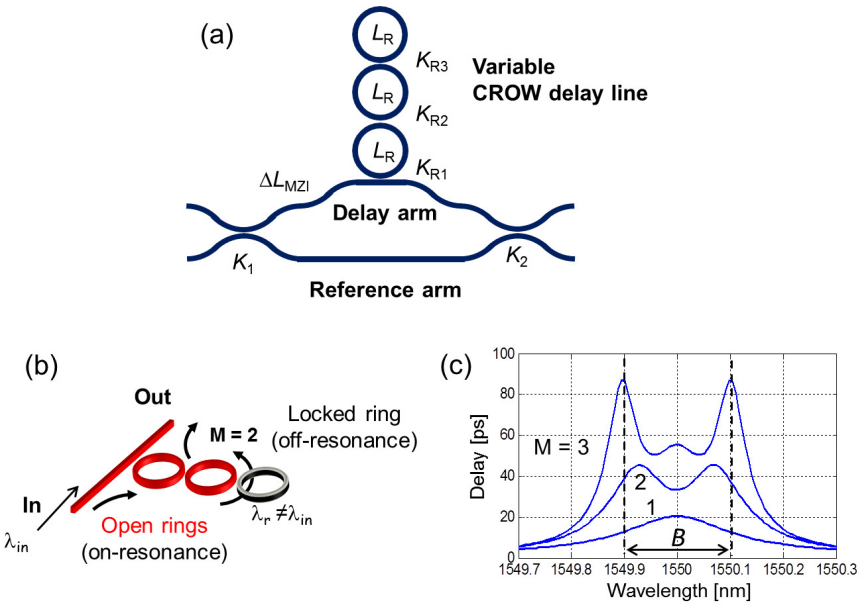

Figure 6.6: *(a) Schematic of the variable delay DPSK receiver consisting of an unbalanced MZI loaded with a tunable CROW delay line. (b) Delay tuning mechanism of a reflective CROW delay line. (c) Simulated group delay of the CROW delay line when M rings (M = 1, 2, 3) are progressively set to resonance.*

comprised between 0 (locked ring, off-resonance condition) and

$$T_{max} = \frac{2}{\pi B} \tag{6.1}$$

that is the delay due to the double pass light propagation across a ring in on-resonance condition (open ring). By partially detuning the resonance of the last open ring, any intermediate delay between 0 and T_{max} can be added in order to control the overall delay with continuity [50].

Actually, the need for impedance matching of the CROW to the bus waveguide requires that K_{R_i} progressively decreases (that is the finesse of the resonators increases) along the structure [146], so that the maximum delay provided by each resonator slightly deviates from the mean value T_{max} provided by Eq. 6.1. For example, Fig. 6.6(c) shows the simulated group delay of a tunable CROW delay line made of 3 identical coupled resonators with geometric length L_R = 476 μm, n_g = 4.2, and $FSR = c/(n_g L_R)$ = 150 GHz. The coupling coefficients (K_{R_1} = 0.76, K_{R_2} = 0.26, and K_{R_3} = 0.15) are designed in order to provide a bandwidth B of about 25 GHz. The additional delay provided by each open ring, averaged across the CROW

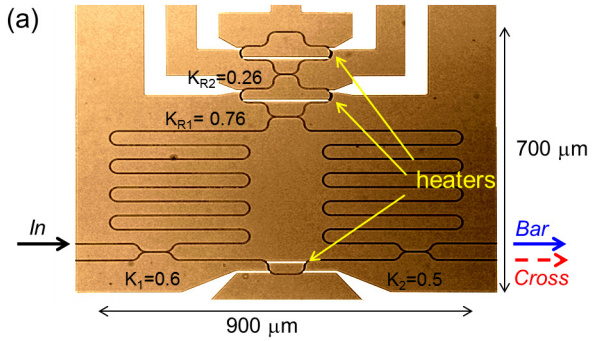

Figure 6.7: *Top-view photograph of the silicon photonics variable symbol-rate DPSK receiver.*

passband, is 17 ps (M = 1), 22 ps (M = 2), and 23 ps (M = 3). The tuning approach, which is here numerically shown for 3 rings only, can be generalized to an arbitrary number of coupled rings [48].

The group delay of the CROW is not constant across the transmission band B and exhibits two sharp peaks at the band edges. Moreover, some ripples are originated by the interference of the delayed optical signal with the small raction of the light that is not coupled with the CROW (about 5% in the considered example). However, no significant distortion occurs in the delayed signal provided that the group delay variations across the signal bandwidth are small. This condition is achieved if the impedance matching of the structure is optimized and if the signal spectrum is entirely contained within the CROW passband [50].

6.4.2 Device fabrication and characterization

The proposed device was fabricated by the University of Glasgow on a SOI platform with the same technology described in Sec. 2.1 and Sec. 3.2. The top view photograph of the fabricated device is shown in Fig. 6.7. The MZI unbalance is ΔL_{MZI} = 4736 μm and the longer arm is folded in order to keep the overall footprint as small as 900 μm $\times$ 700 μm. To minimize radiation loss in the bends and at the straight-to-curved waveguide transitions, the minimum curvature radius of the circuit is larger than 20 μm. A CROW made of two microring resonators is coupled to the longer arm of the MZI. The rings have a racetrack geometry with the same design parameters of the first two rings of the device considered in Fig. 6.6(c), that is L_R = 476 μm, K_{R_1} = 0.76 and K_{R_2} = 0.26. The directional couplers of the rings have a gap distance between the waveguide of 300 nm, and a coupling length

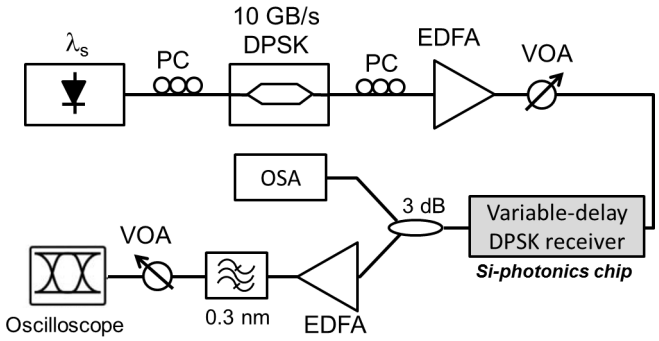

Figure 6.8: *Schematic of the experimental setup employed for the characterization of the variable symbol-rate DPSK receiver.*

of 26 μm and 56 μm, respectively. The power coupling coefficients of the MZI directional couplers, K_1 = 0.6 and K_2 = 0.5, were optimized to compensate for the delay-dependent loss of the CROW in order to guarantee a good extinction ratio (*ER*) of the MZI response at any tuning conditions (see Sec. 6.4.4). Metallic heaters were deposited onto the waveguides to thermally adjust the resonant wavelengths λ_{R_1} and λ_{R_2} of the rings [43], and to finely set the phase of the reference arm of the MZI.

6.4.3 Experimental setup

Figure 6.8 shows the experimental setup used for the optical characterization of the proposed device and for evaluating its performance on the detection of DPSK signals. A tunable laser is employed to generate a continuous-wave (CW) optical signal at a wavelength λ_s around 1550 nm. The light source is modulated with a $LiNbO_3$ phase modulator driven by a 10 Gb/s signal. The modulated signal is then amplified by an erbium-doped fiber amplifier (EDFA) and its intensity is controlled through a variable optical attenuator (VOA). Two polarization controllers (PCs) are used to adjust the polarization of the light at the input of the modulator and of the chip, respectively. Tapered lensed fibers with 1.7 μm spot size were employed to couple the light into and out of the silicon chip. The state of polarization is set to TE and the coupling loss of the inverse taper is about 5 dB.

In order to perform simultaneous time domain and frequency domain measurements, at the output of the chip a 3 dB fiber coupler is employed to transmit a portion of the signal to an OSA and to a 20 GHz optical sampling oscilloscope. Due to the limited sensitivity of the oscilloscope used for eye diagram measurements (about -15 dBm), a second EDFA is used to

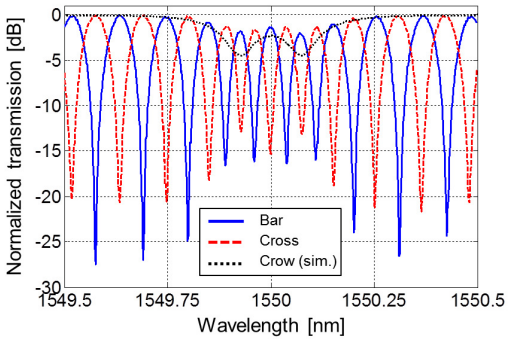

Figure 6.9: *Measured transmission of the device at the Bar port (blue solid curve) and at the Cross port (red dashed line) when both rings resonate at 1550 nm. The black dashed curve shows the simulated transmission of the CROW in the same tuning condition.*

compensate for the insertion loss of the chip (about 12 dB) and a VOA is added to keep a constant power level of about -9 dBm at the input of the photodiode. The signal is also filtered using a tunable band pass filter with a bandwidth of 0.3 nm to remove the off-band amplified spontaneous emission (ASE) noise generated by the two EDFAs.

6.4.4 Experimental results

Spectral response and delay tuning

The measured spectral response at the two output ports of the fabricated device is shown in Fig. 6.9, when the resonant wavelengths of both rings are tuned at the same wavelength λ_0 = 1550 nm. Referring to Fig. 6.7, the blue solid curve shows the transmission at the Bar port, while the red dashed curve is the transmission at the Cross port. The simulated intensity transmission of the CROW in this tuning condition is shown by the black dashed curve. At wavelengths outside the CROW transmission band (for instance between 1549.5 nm and 1549.8 nm) the delay of the CROW is almost zero, and the receiver exhibits the maximum attainable *FSR* of 15 GHz, corresponding to the delay T_{MZI} = 66.7 ps between the MZI waveguides of the MZI arms. Around λ_0, the CROW adds a delay of about 34.5 ps [see Fig. 6.6(c)], that reduces the *FSR* to the minimum value of 9.8 GHz. Since the delay of the CROW can be continuously tuned between 0 and 34.5 ps, any intermediate *FSR* can be achieved at the desired wavelength.

Figure 6.10(a) shows the tunability of the device transmission spec-

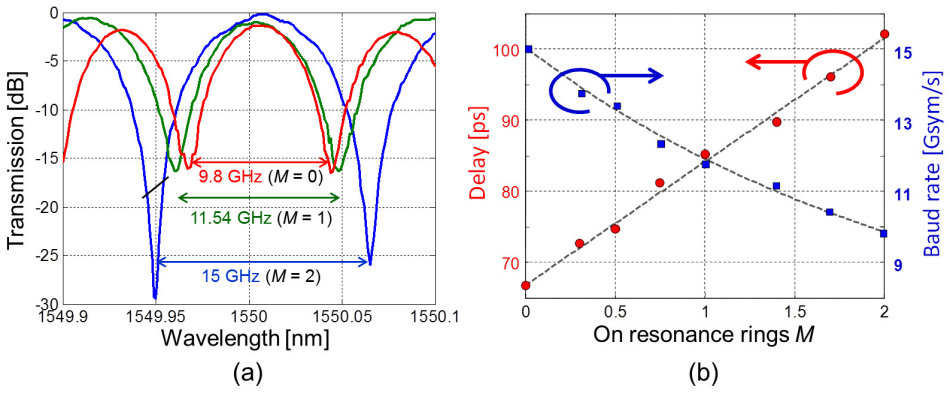

Figure 6.10: *(a) Measured transmission of the variable delay MZI when both rings are off-resonance (blue curve, λ_{R_1} = λ_{R_2} = 1550.6 nm, FSR = 15 GHz), only the first ring is on resonance (green curve, λ_{R_1} = 1550 nm, λ_{R_2} = 1550.6 nm, FSR = 11.54 GHz), and both rings are on resonance (red curve, λ_{R_1} = λ_{R_2} = 1550 nm, FSR = 9.8 GHz). (b) The receiver delay (red circles) and symbol-rate (blue squares) are continuously tuned from 66 ps (15 Gsym/s) to 102 ps (9.8 Gsym/s) by shifting the rings resonances.*

trum around λ_0. Let us assume as initial condition that both rings are off-resonance, that is $\lambda_{R_1} \neq \lambda_0$ and $\lambda_{R_2} \neq \lambda_0$ (blue curve, *FSR* = 15 GHz). Starting from this condition, the resonance λ_{R_1} of the first ring is tuned to λ_0, thus reducing the *FSR* of the device to 11.54 GHz (green curve). Then, by having also the second ring resonate at $\lambda_{R_2} = \lambda_0$, the *FSR* is further reduced to 9.8 GHz (red curve). Figure 6.10(b) shows the measured delay (red circles) between the MZI arms at several tuning conditions between the minimum and maximum attainable *FSR*. Partial detuning of the rings provides continuous delay tunability, from 66.6 ps to 102 ps, enabling the use of the receiver for the optimal detection of DPSK signals with a symbol rate spanning from 9.8 to 15 Gsym/s (blue squares).

Figure 6.10(a) shows that the *FSR* decrease is associated with a reduction of the *ER* of the receiver. This effect is mainly due to the delay-dependent loss of the CROW. The round trip loss of the ring resonators was estimated around 0.35 dB/turn, where 0.15 dB loss is due to the waveguide propagation loss (3 dB/cm), and 0.2 dB loss is from the excess loss of the directional couplers and the straight-curve transitions in the resonator geometry. Nonetheless, an *ER* higher than 15 dB was observed at any tuning conditions between the minimum and maximum *FSR*. In a single-ended receiver, the expected power penalty due to non-infinite *ER* is less than 0.5 dB for $ER > 15$ dB, while in a balanced detection scheme is almost negligi-

ble [137]. The total on-chip insertion loss of the device is slightly affected by the delay-dependent loss of the CROW, since it increases from 1 dB to 2 dB loss from the maximum to the minimum *FSR* condition.

Full tunability of the receiver requires that the ring round trip phase is shifted from 0 to π to bring the resonators from off-resonance to on-resonance state. An additional phase shift of up to π is required in the shorter arm of the MZI to align the receiver response to the wavelength of the transmitted signal. As in conventional MZIs, a π phase-shift between the MZI arms is responsible for the half *FSR* shift of the spectral response, that is for the mutual switch of the Bar and Cross ports. Since the power consumption of the fabricated heaters is 10 mW to achieve π-shift less than 30 mW are needed for the full tunability of the receiver. However, the power consumption can be significantly reduced by employing the As_2S_3-assisted Si waveguide structure presented in Sec. 2.2.2 that does not require power-hungry thermo-optic actuators.

DPSK signal detection

The variable delay MZI was employed to receive a 10 Gsym/s binary DPSK signal transmitted at a wavelength of 1550 nm. In particular, in this experiment, the delay of the CROW was optimized to match the exact symbol rate of the signal and optimize the performance of the system. The quality of the detected signal was evaluated by considering the system Q-factor and the half-height horizontal opening A_h of the eye diagram, the latter providing direct information on the impairments associated with intersymbol interference (ISI) effects.

Figure 6.11(a) shows the comparison between the simulated (circles) and measured (squares) A_h of the intensity modulated signal detected in single-ended configuration versus the delay mismatch $\Delta\tau$ between the MZI delay and the symbol time. Simulations were performed by using the measured spectral response of the MZI receiver and assuming a noise-free optical signal. When the two rings are tuned off-resonance, the symbol rate does not match the *FSR* of the receiver (*FSR* = 15 GHz) and $\Delta\tau$ = -34 ps (blue square). In these conditions, the measured eye-diagram [shown Fig. 6.11(b_1)] is triangularly shaped because of the strong ISI that causes an evident splitting of the signal transitions. The eye opening A_h is as low as 49 ps and the Q-factor is 5.35.

By opening the first ring (λ_{R_1} = 1550 nm), $\Delta\tau$ is reduced to -14 ps, transition splitting in the detected eye diagram disappears (b_2), and A_h increases to 67 ps (green square). Full delay-mismatch compensation ($\Delta\tau$ = 0) is obtained when the second ring is partially opened (λ_{R_2} about 1549.82

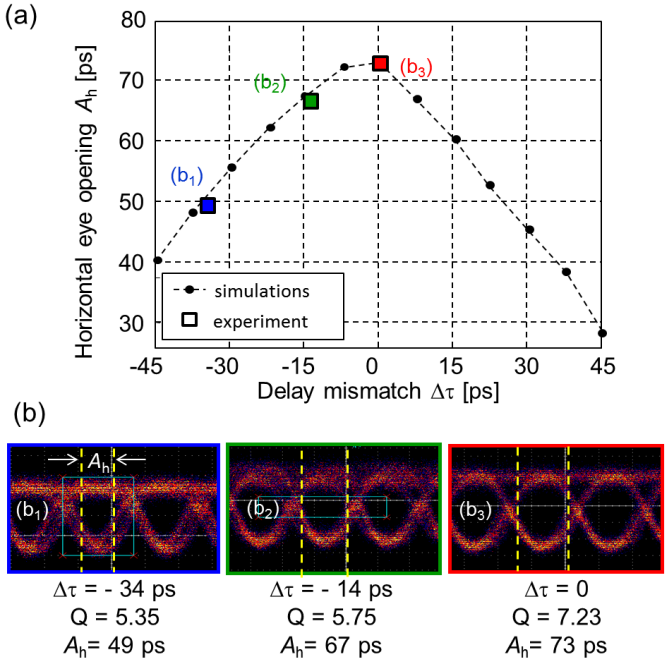

Figure 6.11: *Performance of the variable delay DPSK receiver for a 10 Gsym/s signal. (a) Simulated (circles) and measured (squares) horizontal opening A_h of the detected eye-diagram versus the mismatch $\Delta\tau$ between the MZI delay and the symbol time. Measured eye diagrams are shown in (b).*

nm) and the detected eye diagram (b_3) exhibits the maximum opening A_h = 73 ps (red square) and a Q-factor of more than 7. In these conditions, the amplitude modulation depth of the demodulated signal is more than 10 dB.

The results refer to the receiver used in single-ended configuration. However, as shown in Fig. 6.9, within the CROW passband the proposed device behaves as a conventional MZI, that is constructive interference at one output port implies destructive interference at the other port. Therefore, balanced detection can be adopted to improve receiver performance.

Robustness to nonlinear effects and stabilization

The variable delay DPSK receiver was also tested at high input power to evaluate the impact of nonlinear effects on the detected signal. The receiver was first calibrated in the linear regime to have the best performance ($\Delta\tau$ = 0) for a 10 Gsym/s signal. Black curve in Fig. 6.12(a) shows the device transmission when the power in the input waveguide of the receiver is 0

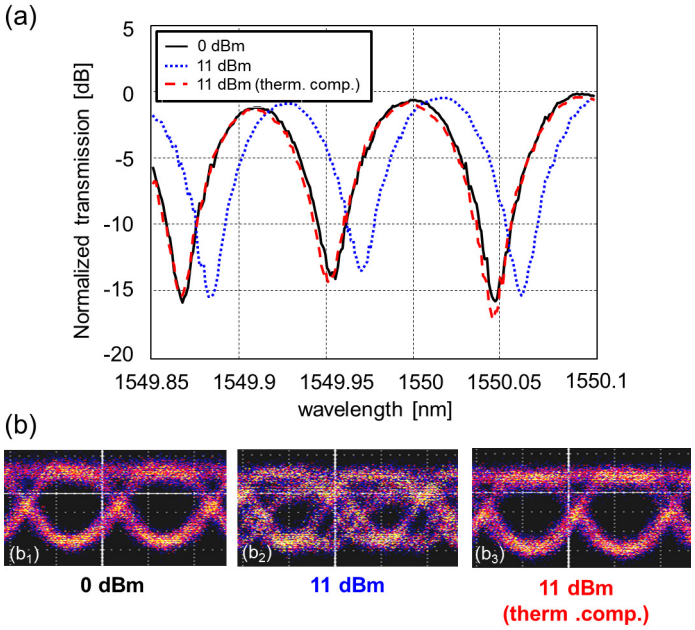

Figure 6.12: *(a) Frequency-domain response of the variable delay receiver optimized for the detection of a 10 Gsym/s DPSK signal for increasing power in the input waveguide: 0 dBm (black solid curve), 11 dBm (blue dotted curve). The red dashed curve shows the thermally compensated nonlinear response. (b) Eye diagrams of the detected signal when the receiver operates in the three conditions shown in (a).*

dBm and the detected eye is shown in Fig. 6.12(b_1). When the input power is increased to 11 dBm, thermal effects induced by two-photon absorption (TPA) introduce a distortion of the device transmission [43,67] , that mainly consists of a 22 pm red-shift of the spectral response (blue dotted curve). As shown in Fig. 6.12(b_2), this misalignment between the receiver and the signal carrier frequencies causes a strong distortion of the eye diagram. The nonlinear red-shift can be easily compensated by adjusting the temperature of the integrated heaters in order to make the high power spectral response overlap the calibrated linear response (red dashed curve) and restore the eye diagram [see Fig. 6.12(b_3)].

It is worth noticing that, by employing the athermal and trimmable Si photonic waveguide developed in Sec. 5.1.1, the receiver would be insensitive to high-power induced thermal effects and thus intrinsically robust to thermal nonlinearities. Further, at the same time, full reconfigurability and adaptability of the receveir to different symbol-rate would be preserved thanks to the As_2S_3 trimming layer.

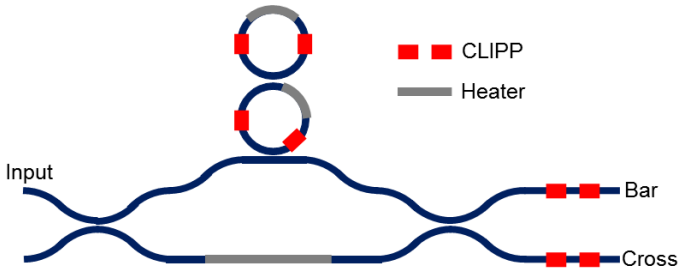

Figure 6.13: *Scheme of the DPSK receiver with CLIPPs (in red) and heaters (in grey) to feedback control and stabilize its operation.*

On the other hand, stabilization and control of the circuit to compensate for thermal fluctuations (both in the linear and nonlinear regimes) can be achieved by means of feedback control loops assisted by the CLIPP. For instance, with reference to Fig. 6.13, it is sufficient to place the CLIPPs (in red) inside each resonator to monitor the delay introduced by the CROW, and on the Bar and Cross ports of the MZI to monitor its unbalance. Then, with a similar scheme to that of Fig. 5.10(a), the information provided by the CLIPPs can be used to drive the heaters (in grey) placed on the microrings and on the MZI.

6.4.5 Discussion

The symbol-rate variability range of the receiver discussed in Sec. 6.4.4 was designed in order to provide a proof-of-concept demonstration of the device performance with 10 Gbit/s signals. However, silicon photonics enables the scalability of the proposed receiver up to 100 Gsym/s systems and beyond.

A variable symbol-rate DPSK receiver operating from 40 to 100 Gsym/s can be realized with a MZI unbalance ΔL_{MZI} = 714 μm (providing a delay of 10 ps, corresponding to FSR_{max} = 100 GHz) and a CROW with B = 100 GHz. A 100 GHz bandwidth can be obtained with ring resonators with a FSR of 600 GHz and the same coupling coefficients K_{R_i} used in Fig. 6.6(c). The corresponding geometric length of the rings (120 μm) requires a bending radius of more than 15 μm, that is achievable with silicon photonics waveguides with no significant bending loss. With these design parameters, the delay provided by each ring is 4.6 ps (M = 1), 5.5 ps (M = 2), and 5.7 ps (M = 3), thus providing delay tunability from 10 ps to about 26 ps, corresponding to a bandwidth tunability from 100 GHz to less than 40 GHz.

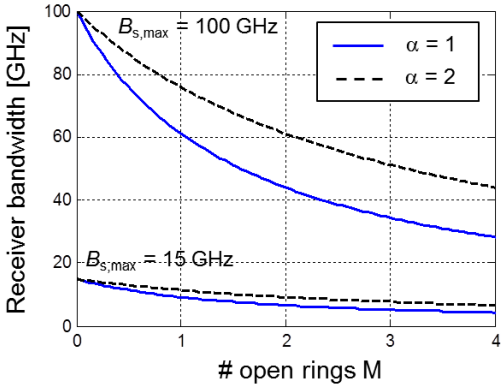

Figure 6.14: *Tunability range of the variable-symbol rate receiver versus the number of open rings loaded to the longer arm of the MZI. Maximum receiver bandwidths (M = 0) of 15 and 100 GHz are considered. Blue solid curves indicate the case B = B_s (α = 1), black dashed curves indicate the case B = 2B_s (α = 2).*

The maximum tunability range achievable with the proposed receiver can be simply related to the number of rings loaded to the longer arm of the MZI. In fact, the ratio between the maximum and minimum bandwidth of the receiver, respectively given by the maximum and minimum *FSR* of the ring-loaded MZI, is given by

$$\frac{FSR_{max}}{FSR_{min}} = \frac{T_{MZI} + T_{CROW,max}}{T_{MZI}} = 1 + \frac{MT_{max}}{T_{MZI}} \tag{6.2}$$

where $T_{CROW,max}$ is the maximum delay provided by a CROW with M rings set to resonant condition (open rings). Both the fixed delay T_{MZI} between the MZI arms and the delay T_{max} given by each ring [see eq. 6.1] depend on the bandwidth B_s of the signal to be detected. In fact, T_{MZI} has to be chosen in order to exactly match the maximum signal bandwidth, that is $T_{MZI} = B_{s,max}^{-1}$. Then, in order to avoid significant distortion of the detected signal, $B_{s,max}$ has to be smaller than the CROW bandwidth B, that is $T_{max} = 2/\alpha\pi B_{s,max}$, where $\alpha = B/B_{s,max}$ (with $\alpha > 1$). By substituting the conditions on T_{MZI} and T_{max} into eq. 6.2, one straightforwardly obtains

$$\frac{FSR_{max}}{FSR_{min}} = 1 + \frac{2M}{\alpha\pi} \tag{6.3}$$

relating the tunability range of the variable-symbol rate DPSK receiver to the number of rings of the CROW.

Figure 6.14 numerically shows the tunability range of receivers designed to have maximum bandwidths (M = 0) of 15 GHz and 100 GHz, respectively. By assuming $B = B_s$ (blue solid curve, $\alpha = 1$), the number of required rings is minimized and more than 50% bandwidth tunability is achieved with only 2 rings. However, this can result in some signal distortion originated by the band-edge peaks in the group delay response of the CROW [see Fig. 6.6(c)], especially when many rings are employed ($M > 3$). In the device discussed in Sec. 6.4.4, the bandwidth of the CROW (B = 25 GHz) was chosen about twice the signal bandwidth (black solid curve, α = 2), and no evidence of signal distortion was observed. Therefore, the α-parameter has to be optimized, typically between values of 1 and 2, as a tradeoff between requirements on signal quality, electric power consumption for the tuning of the receiver and complexity of the tuning scheme, that increase with the number of rings to be controlled.

A final consideration concerns the sensitivity of the device to the state of polarization of the incoming light. In this device, polarization sensitivity is related to the large birefringence of the silicon waveguides, and not to the device architecture. To mitigate polarization sensitivity in high index contrast waveguides, polarization diversity schemes can be adopted, where the polarization at the input of the chip is split into the orthogonal TE and TM components, and the TM component (typically) is rotated to TE in order to have only TE polarized light on chip [147, 148]. This is a general scheme that can be adopted for most devices and is applicable to the proposed receiver too.

Conclusion

The final Section of this thesis summarizes the main results and achievements of this work, suggesting also future developments and perspectives for this research activity.

As we learn since the beginning of this thesis, photonic integrated circuits are intrinsically imperfect because they are extremely sensitive to the effects of fabrication tolerances, temperature fluctuations, mutual cross-talk etc. For this reason, in order to increase the scale of integration in photonics, some novel tools and devices, such as low-power actuators and post-fabrication treatments, transparent photodetectors, and feedback loops, need to be developed. This enables to cope with the aforementioned parasitics, and thus to move from a level of single-devices to a concept of systems-on-chip.

To this aim, low power actuators and post-fabrication trimming techniques, based on the integration of photosensitive As_2S_3 chalcogenide glass with photonic waveguides, were developed. The spectral response of As_2S_3 core devices (such as resonators and MZIs) and As_2S_3-assisted Si microrings was permanently trimmed to compensate for fabrication tolerances and for circuit reconfiguration. Devices were selectively exposed to near band-gap visible light with low intensity (i.e., few mW/cm^2) to change the refractive index of the As_2S_3 glass, and therefore the effective index of the waveguide and the effective behavior of the circuit. Photo-induced trimming of Si resonators was performed by shifting the microring resonance by about 6.7 nm, and thus inducing an effective index change of the chalcogenide glass larger than 10^{-2}. Saturation effects, wavelength range, velocity and

temporal stability of the process were discussed in details. Compared to alternative approaches, requiring sophisticated and expensive tools, the visible light sensitivity of As_2S_3 allows the realization of an extremely simple and low-cost trimming technique, employing only a common halogen lamp and an optical fiber. Despite its simplicity, the trimming is highly selective and accurate, enabling local changes in the optical properties of the circuit with a resolution of about 30 μm, that can be easily narrowed down by one order of magnitude with a special fiber or a lens. Results demonstrate that photo-induced permanent trimming can be exploited for compensation of fabrication tolerances and for setting-and-reconfiguration of the device response, without the need for always-on, power-hungry thermo-optic or electro-optic conventional actuators.

However, when integrating several components, the action of actuators and post-fabrication treatments need to be assisted by local information on the status of each embedded device of the circuit. This information should be made available without affecting the operation of the circuit itself, that is with no introduction of additional loss or perturbations of the optical field. To this purpose, the first non-invasive observer of light was demonstrated in silicon photonics waveguides. This transparent light monitor, that is the ContactLess Integrated Photonic Probe (CLIPP), exploits the interaction of the optical mode with intrinsic surface states, that are located at the interface between the Si core and the waveguide cladding within the first atomic layers from the surface. Light monitoring is performed by measuring the changes of the conductance of the Si core of the waveguide with light. Monitoring of optical power across 40 dB dynamic range, down to -30 dBm, both on monomode and multimode waveguides, and both on TE and TM polarizations is demonstrated. Furthermore, several CLIPPs were placed in a photonic circuit, thus enabling multipoint monitoring of devices, such as microring resonators. The non-invasive nature of the CLIPP was tested by looking for a perturbation component at the frequency of the applied CLIPP voltage: only an ultrasmall perturbation of the waveguide effective index is observed, that is caused by the non-zero electrooptic effect of Si waveguides, which is comparable to that that would be induced by thermal fluctuations of only few mK. Also, extensive investigation of the CLIPP performances, in terms of dependence on waveguide geometry, polarization, wavelength, speed, sensitivity, and miniaturization, was reported. Finally, extension of the CLIPP to other photonic platforms, such as indium phosphide, is shown.

Thanks to the development of the CLIPP concept and its applications, much attention was focused to the investigation of the effects that occur in

Si waveguides in presence of light and affect the propagation of the optical mode. In particular, the effect of variations in the carrier mobility (induced by temperature change, radiation pressure or electrostriction induced optical forces, and carrier density variations) and density (induced by TPA/FCA processes and SSA mechanisms) were investigated to establish that SSA is the physical process behind the operation of the CLIPP. Moreover, a novel all-optical technique for the observation of SSA induced carrier absorption was developed, which was found to be one order of magnitude larger than TPA for low optical power levels (up to about 1 mW). Also, by comparing this measurement (all-optical) with the CLIPP observation (electrical), it was possible to confirm directly that SSA is indeed the effect enabling the CLIPP operation.

Then, the low-power actuators and the CLIPP were utilized to stabilize the operation of Si circuits and to provide feeedback control. Here, the first passive athermal and trimmable Si waveguide was proposed and experimentally demonstrated. By sandwiching a thin layer of photosensitive As_2S_3 glass between the Si core and a negative thermo-optic coefficient polymer cladding, simultaneous athermal operation and trimming functionality were provided to a Si waveguide. Sensitivity to thermal variations in a ring resonator were as low as $\pm$ 5 pm/K across a 50 nm wavelength range, with one wavelength where no appreciable sensitivity with temperature changes was observed. Fine trimming across 10 nm (5 FSRs) was shown, preserving the thermal dependence of the waveguide after trimming. Passive thermal mitigation was also shown at high-power to compensate for temperature induced non-linear wavelength shifts, achieving a 70-fold compensation with respect to conventional SiO_2-coated Si waveguides up to a power level of about 22 dBm. Furthermore, potential extension of the athermal and trimmable waveguide design to a fully CMOS-compatible material platform was shown by using $BaTiO_3$ as the trimming/tuning layer and TiO_2 as the thermal compensation material.

Active stabilization and feedback control was demonstrated in a thermally actuated high quality factor Si resonator by using a CLIPP integrated inside the microring. First, tuning of the resonant wavelength assisted by the CLIPP was shown: while the voltage applied to the heater is changed the CLIPP simultaneously monitors the light intensity in the cavity without affecting the quality factor of the resonator. The tuning procedure was also performed automatically on a time scale of few hundreds of ms. Then, the resonant wavelength is locked to that of an external laser. Feedback control is performed by means of a dithering approach and by exploiting the error signal provided by the CLIPP, that is then utilized by an integral controller

to drive the loop. The effectiveness of this approach was tested in presence of a laser wavelength detuning by 50 pm (that is about the same of the linewidth of the resonator), that is compensated in about 150 ms. The speed of the loop can be increased with advanced control laws/algorithms or by enlarging the CLIPP read-out bandwidth. Furthermore, the CLIPP is able to monitor and discriminate suitably labeled signals, allowing one to tune and lock photonic devices to the wavelength of a channel, regardless of the presence of other signals, simultaneously coexisting in the same photonic device (indeed this can be applied not only to different wavelengths, but also to different modes and polarizations). All these advanced control functionalities are possible thanks to a CMOS microelectronic circuit that is bridged to the Si photonic chip. The possibility of managing feedback-controlled photonics through standard CMOS electronics makes this approach directly exploitable in system-level applications. The compactness and scalability of CMOS electronics to multichannel read-out systems allows one also to extend the presented approach to the control of complex integrated circuits hosting many photonic components.

Then, a nice application of the CLIPP was found in the process of fiber-to-waveguide alignment. Thanks to its non-invasive nature, the CLIPP can be placed near the facet of the photonic chip, so that the signal measured depends only on the coupling between the external fiber and the waveguide, regardless of what photonic circuit is hosted on the sample and regardless of its "health status" and performance. By exploiting this approach one fiber at a time can be aligned to the photonic waveguide, thus overcoming the inherent complexity of traditional approaches that require the simultaneous alignment of two fibers. Furthermore, by using feedback loops the fiber-to-waveguide coupling process can be performed in a few seconds time scale, and then after alignment is achieved the CLIPP presence can be neglected thanks to its non-perturbative nature.

Finally, the tools, techniques and devices that were developed within this work were used in more complex photonic structures to show concepts and advanced functionalities such as circuit reconfiguration and adaptability. In particular, transfer function recovery (necessary because of the presence of strong fabrication tolerances) and circuit reconfiguration to adapt the devices to specific needs were demonstrated in high-order filters and delay lines composed of several As_2S_3 coupled resonators by exploiting the photo-induced trimming technique. These results show that the PIC functionality can be modified after fabrication to fulfill specific applications, and is held after trimming withous continuous power consumption. Local monitoring of Si coupled resonator structures was achieved with the

assistance of the CLIPP, thus showing how the tuning process can be simplified with respect to conventional approaches. Finally, an example of an even more complex structure, that is a variable symbol-rate DPSK receiver composed of a MZI and a coupled resonator delay line, is provided. Design, experimental characterization, tuning, and stabilization with respect to Si nonlinearities are reported. This example, besides nicely showing the perspective of this work, offers a nice circuit platform to discuss issues of tuning, stabilization, reconfigurability and adaptability in complex, high-order PICs.

In conclusion, the work developed within this thesis is expected to find direct application and exploitation in photonic integrated circuits aggregating many components. In particular, the CLIPP, along with the action of feedback loops and low-power actuators, provides a nice set of tools to boost the complexity of integrated photonics and for the delivery of advanced functionalities.

Publications

A list of the publications and original contributions of this thesis is here provided.

Journals

1. S. Grillanda, F. Morichetti, N. Peserico, P. Ciccarella, A. Annoni, M. Carminati, and A. Melloni, "Non-invasive monitoring of mode-division multiplexed channels on a silicon photonic chip," submitted to the *J. Lightwave Technol.* special issue of ECOC 2014 (Oct. 2014). (***Invited***).

2. M. Carminati, S. Grillanda, P. Ciccarella, G. Ferrari, M. Strain, M. Sampietro, A. Melloni, and F. Morichetti, "Fiber to waveguide alignment assisted by a transparent integrated light monitor," submitted to *IEEE Photon. Technol. Lett.* (Aug. 2014).

3. S. Grillanda, M. Carminati, F. Morichetti, P. Ciccarella, A. Annoni, G. Ferrari, M. Strain, M. Sorel, M. Sampietro, and A. Melloni, "Non-invasive monitoring and control in silicon photonics using CMOS integrated electronics," *Optica*, vol. 1, no. 3, pp. 129-136, Aug. 2014.

4. M. Mattarei, A. Canciamilla, S. Grillanda, and F. Morichetti, "Variable symbol-rate DPSK receiver based on silicon photonics coupled-resonator delay line," *J. Lightwave Technol.*, vol. 32, no. 19, pp. 3317-3323, Oct. 2014.

5. F. Morichetti, S. Grillanda, and A. Melloni, "Breakthroughs in photonics 2013: toward feedback-controlled integrated photonics," *IEEE Photon. Jour.*, vol. 6, no. 2, pp. 1-6, Apr. 2014. (***Invited***).

6. F. Morichetti, S. Grillanda, M. Carminati, G. Ferrari, M. Sampietro, M. Strain, M. Sorel, and A. Melloni, "Non-invasive on-chip light observation by contactless waveguide conductivity monitoring," *IEEE J. Sel. Top. in Quantum Electron.*, vol. 20, no. 4, pp. 292-301, July 2014.

7. S. Grillanda, V. Raghunathan, V. Singh, F. Morichetti, J. Michel, L. Kimerling, A. Melloni, and A. Agarwal, "Post-fabrication trimming of athermal silicon waveguides," *Opt. Lett.*, vol. 38, no. 24, pp. 5450-5453, Dec. 2013.

8. J. Mu, Z. Han, S. Grillanda, A. Melloni, J. Michel, L. Kimerling, and A. Agarwal, "Towards ultra-subwavelength optical latches," *Appl. Phys. Lett.*, vol. 103, no. 4, pp. 043115-4, July 2013.

9. A. Canciamilla, F. Morichetti, S. Grillanda, P. Velha, M. Sorel, V. Singh, A. Agarwal, L. Kimerling, and A. Melloni, "Photo-induced trimming of chalcogenide-assisted silicon waveguides," *Opt. Express*, vol. 20, no.14, pp. 15807-15817, June 2012.

10. A. Canciamilla, S. Grillanda, F. Morichetti, C. Ferrari, J. Hu, J. Musgraves, K. Richardson, A. Agarwal, L. Kimerling, and A. Melloni, "Photo-induced trimming of coupled ring-resonator filters and delay lines in As2S3 chalcogenide glass," *Opt. Lett.*, vol. 36, no. 20, pp. 4002-4004, Oct. 2011.

Patent applications

1. A. M. Agarwal, A. Canciamilla, F. Morichetti, S. Grillanda, L. C. Kimerling, A. Melloni, J. Michel, V. Raghunathan, V. Singh, "Athermal Photonic Waveguide With Refractive Index Tuning," US 2013 0243383 A1, Feb. 2012.

2. A. Melloni, M. Sampietro, G. Ferrari, S. Grillanda, F. Morichetti, M. Carminati, "Optical radiation detection system comprising an electric parameter measuring circuit," WO 2014/096449 A1, Dec. 2012.

Conferences

1. S. Grillanda, F. Morichetti, N. Peserico, P. Ciccarella, A. Annoni, M. Carminati, M. Sampietro, and A. Melloni, "Hitless Monitoring of Wavelength and Mode-Division Multiplexed Channels on a Silicon Photonic Chip," submitted to OFC 2015 (Nov. 2014).

2. A. Melloni, F. Morichetti, S. Grillanda, A. Annoni, M. Sampietro, and C. Carminati, "Feedback and control in integrated optics enabled by ContactLess Integrated Photonic Probe," submitted to Photonics West 2015 (July 2014). (***Invited***).

3. M. Carminati, G. Ferrari, P. Ciccarella, S. Grillanda, F. Morichetti, A. Melloni, and M. Sampietro, "Low-noise instrument for non-invasive monitoring of photonic integrated circuits," submitted to 2015 IEEE International Instrumentation and Measurement Technology Conference (Oct. 2014).

4. S. Grillanda, M. Carminati, F. Morichetti, P. Ciccarella, A. Annoni, G. Ferrari, M. Sampietro, A. Melloni, "Feedback control of silicon microrings by non-invasive photonic probe," Integrated Photonics Research, Silicon, and Nanophotonics (IPR), San Diego (CA), July 13-17, 2014, paper JM4B.3.

5. S. Grillanda, F. Morichetti, M. Carminati, P. Ciccarella, A. Annoni, G. Ferrari, M. Sampietro, A. Melloni, "Wavelength tuning, locking and swapping of a silicon photonics microring resonator by transparent light monitor," European Conference on Optical Communications (ECOC), Cannes, France, Sept. 21-25, 2014, paper We 1.4.4.

6. M. Carminati, S. Grillanda, P. Ciccarella, F. Morichetti, G. Bellotti, D. Bianchi, G. Ferrari, A. Melloni, and M. Sampietro, "Impedance-based transparent monitoring of light for local control of integrated photonic circuits," XXVIII Eurosensors, Brescia (Italy), September 8-10, 2014, paper 5348.

7. S. Grillanda, M. Carminati, F. Morichetti, A. Annoni, P. Ciccarella, G. Ferrari, M. Sampietro and A. Melloni, "Wavelength locking of a silicon microring resonator assisted by contactLess integrated photonic probe," International Conference on Group IV Photonics (GFP), Paris (France), August 27-29, 2014, paper ThC2.

8. S. Grillanda, F. Morichetti, M. Carminati, P. Ciccarella, G. Ferrari, M. Sampietro, and A. Melloni, "Transparent monitoring of light in

integrated optics," European Conference on Integrated Optics (ECIO), Nice (France), June 27-27, 2014, paper Fr 3a R3

9. M. Carminati, P. Ciccarella, S. Grillanda, F. Morichetti, G. Ferrari, A. Melloni, and M. Sampietro, "Low-noise electronics for light monitoring based on contactless waveguide conductivity tracking for closed-loop silicon photonics," accepted at the Riunione Nazionale Gruppo Elettronica, Italy, 2014.

10. F. Morichetti, D. Melati, S. Grillanda, G. Gentili, and A. Melloni, "Understanding, mitigating, and exploiting surface effects in optical waveguides," 16th Photonics North Conference 2014, Paper 13.40 (May 2014). (***Invited***).

11. M. Carminati, S. Grillanda, F. Morichetti, P. Ciccarella, G. Ferrari, M. Sampietro, and A. Melloni, "Automated fiber-to-waveguide coupling assisted by a non-invasive integrated light monitor," Conference on Lasers and Electro-Optics (CLEO), San Jose (CA), June 8-13, 2014, paper JTu4A.80.

12. S. Grillanda, F. Morichetti, M. Carminati, G. Ferrari, M. Strain, M. Sorel, M. Sampietro, and A. Melloni, "Non-invasive integrated light probe," Conference on Lasers and Electro-Optics (CLEO), San Jose (CA), June 8-13, 2014, paper STh3M.3.

13. M. Carminati, S. Grillanda, F. Morichetti, S. Sala, P. Ciccarella, D. Bianchi, G. Ferrari, M. Sampietro, and A. Melloni, "Fiber to silicon waveguide automated coupling driven by a transparent on-chip light monitor," IEEE Optical Interconnects Conference, Coronado (CA), May 4-7, 2014, paper TuP13.

14. F. Morichetti, S. Grillanda, M. Carminati, G. Ferrari, M. Strain, M. Sorel, M. Sampietro, and A. Melloni, "Non-invasive monitoring of silicon microring resonators through contactless integrated photonics probes," IEEE Optical Interconnects Conference, Coronado (CA), May 4-7, 2014, paper MB3.

15. F. Morichetti, A. Annoni, S. Grillanda, P. Orlandi, S. Malaguti, A. Parini, M. J. Strain, M. Sorel, G. Bellanca, P. Bassi, and A. Melloni, "The outcomes of SAPPHIRE, a generic foundry platform for silicon photonics," accepted at the XX Riunione Nazionale di Elettromagnetismo (RiNEm), Padova, Italy, Sept. 2014.

16. F. Morichetti, S. Grillanda, M. Carminati, G. Ferrari, M. Sampietro, and A. Melloni, "Non-invasive light detection on a silicon chip," accepted at the XX Riunione Nazionale di Elettromagnetismo (RiNEm), Padova, Italy, Sept. 2014.

17. C. Alonso Ramos, F. Morichetti, S. Grillanda, A. Ortega-Monux, I. Molina-Fernandez, and A. Melloni, "Photonic Integrated Dual-Mode Filters Realized with Ring Resonators Loaded by Bragg Gratings," in Integrated Photonics Research, Silicon and Nanophotonics, OSA Technical Digest (online) (Optical Society of America, 2013), paper IT5A.3.

18. V. Raghunathan, S. Grillanda, A. Canciamilla, V. Singh, F. Morichetti, J. Michel, A. Agarwal, A. Melloni, L. Kimerling, "High capacity, photo-trimmable athermal silicon waveguides," Group IV Photonics (GFP), 2012 IEEE 9th International Conference on, vol., no., pp.45-47, 29-31 Aug. 2012.

19. S. Grillanda, A. Canciamilla, F. Morichetti, J. Hu, V. Raghunathan, V. Singh, A. Agarwal, L. Kimerling, and A. Melloni, "Exploiting photosensitive As2S3 chalcogenide glass in photonic integrated circuits," Transparent Optical Networks (ICTON), 2012 14th International Conference on, vol., no., pp.1-4, 2-5 July 2012.

20. V. Raghunathan, S. Grillanda, V. Singh, A. Canciamilla, F. Morichetti, A. Agarwal, J. Michel, A. Melloni, and L. C. Kimerling, "Trimming of Athermal Silicon Resonators," in Integrated Photonics Research, Silicon and Nanophotonics, OSA Technical Digest (online) (Optical Society of America, 2012), paper IW4C.5.

21. F. Morichetti, A. Canciamilla, S. Grillanda, P. Orlandi, S. Malaguti, M. Strain, M. Sorel, G. Bellanca, P. Bassi, and A. Melloni, "SAPPHIRE: A Generic Foundry Platform for Silicon Photonics," XIX Riunione Nazionale di Elettromagnetismo (RiNEm), Rome, Italy, 10-14 Sept. 2012.

22. A. Canciamilla, C. Ferrari, M. Mattarei, F. Morichetti, S. Grillanda, A. Melloni, M. Strain, M. Sorel, P. Orlandi, and P. Bassi, "A variable delay integrated receiver for differential phase-shift keying optical transmission systems," 16th European Conference on Integrated Optics (ECIO), Sitges, Barcelona, Spain, 18-20 April 2012.

23. A. Melloni, S. Grillanda, A. Canciamilla, C. Ferrari, F. Morichetti, M. Strain, M. Sorel, V. Singh, A. Agarwal, and L. Kimerling, "Photo-induced trimming of chalcogenide-assisted silicon photonic circuits," Proc. SPIE 8266, 82660A (2012). (***Invited***).

24. A. Canciamilla, S. Grillanda, C. Ferrari, F. Morichetti, A. Melloni, P. Velha, M. Sorel, J. Hu, J. Musgraves, K. Richardson, V. Singh, A. Agarwal, and L. Kimerling, "Visible light trimming of chalcogenide-assisted photonic integrated circuits," Group IV Photonics (GFP), 2011 8th IEEE International Conference on, vol., no., pp.56-58, 14-16 Sept. 2011.

25. A. Melloni, A. Canciamilla, C. Ferrari, S. Grillanda, F. Morichetti, P. Velha, M. Sorel, J. Hu, J. Musgraves, B. Zdyrko, I. Luzinov, K. Richardson, V. Singh, A. Agarwal, and L. Kimerling, "Exploiting photosensitivity in chalcogenide-assisted integrated optics," in Integrated Photonics Research, Silicon and Nanophotonics, OSA Technical Digest (CD) (Optical Society of America, 2011), paper IMB1. (***Invited***).

26. S. Grillanda, A. Canciamilla, F. Morichetti, and A. Melloni, "Roughness induced backscattering and polarization rotation in optical waveguides," 13th Photonics North Conference, Ottawa, Canada, 16-18 May 2011.

Bibliography

[1] C. R. Doerr, L. L. Buhl, L. Chen, and N. Dupuis, "Monolithic flexible-grid 1x2 wavelength-selective switch in silicon photonics," *J. Lightwave Technol.*, vol. 30, no. 4, pp. 473–478, Feb. 2012.

[2] D. A. B. Miller, "Device requirements for optical interconnects to silicon chips," *Proc. of IEEE*, vol. 97, no. 7, pp. 1166–1185, Jul. 2009.

[3] M. S. Luchansky and R. C. Bailey, "Rapid, multiparameter profiling of cellular secretion using silicon photonic microring resonator arrays," *J. Am. Chem. Soc.*, vol. 133, no. 50, pp. 20500–20506, Oct. 2011.

[4] J. W. Silverstone, D. Bonneau, K. Ohira, N. Suzuki, H. Yoshida, N. Iizuka, M. Ezaki, C. M. Natarajan, M. G. Tanner, R. H. Hadfield, V. Zwiller, G. D. Marshall, J. G. Rarity, J. L. O'Brien, and M. G. Thompson, "On-chip quantum interference between silicon photon-pair sources," *Nat. Photon.*, vol. 8, no. 2, pp. 104–108, Feb. 2014.

[5] T. Baehr-Jones, T. Pinguet, P. L. Guo-Qiang, S. Danziger, D. Prather, and M. Hochberg, "Myths and rumours of silicon photonics," *Nat. Photon.*, vol. 6, no. 4, pp. 206–208, Apr. 2012.

[6] D. A. B. Miller, "Self-configuring universal linear optical component," *Photon. Res.*, vol. 1, no. 1, pp. 1–15, Jun. 2013.

[7] D. A. B. Miller, "Designing linear optical components," *Opt. Photon. News*, vol. 24, no. 212, pp. 38–38, Dec. 2013.

[8] N. K. Fontaine, C. R. Doerr, M. A. Mestre, R. Ryf, P. Winzer, L. Buhl, Y. Sun, X. Jiang, and R. Lingle, "Space-division multiplexing and all-optical MIMO demultiplexing using a photonic integrated circuit," *in National Fiber Optic Engineers Conference*, paper PDP5B.1, OSA Technical Digest (Optical Society of America, 2012).

[9] J. Sun, E. Timurdogan, A. Yaacobi, E. S. Hosseini, and M. R. Watts, "Large-scale nanophotonic phased array," *Nature*, vol. 493, no. 7431, pp. 195–199, Jan. 2013.

[10] C. R. Doerr, "Proposed architecture for MIMO optical demultiplexing using photonic integration," *IEEE Photon. Technol. Lett.*, vol. 23, no. 21, pp. 1573–1575, Nov. 2011.

[11] M. Gnan, S. Thoms, D. S. Macintyre, R. M. De La Rue, and M. Sorel, "Fabrication of low-loss photonic wires in silicon-on-insulator using hydrogen silsesquioxane electron-beam resist," *Electr. Lett.*, vol. 44, no. 2, pp. 115–116, Jan. 2008.

[12] A. Biberman, M. J. Shaw, E. Timurdogan, J. B. Wright, and M. R. Watts, "Ultralow-loss silicon ring resonators," *Opt. Lett.*, vol. 37, no. 20, pp. 4236–4238, Oct. 2012.

[13] E. Timurdogan, C. M. Sorace-Agaskar, J. Sun, E. S. Hosseini, A. Biberman, M. R. Watts, "An ultralow power athermal silicon modulator," *Nat. Comm.*, vol. 5, no. 4008, Jun. 2014.

[14] S. Assefa, F. Xia, and Y. Vlasov, "Reinventing germanium avalanche photodetector for nanophotonic on-chip optical interconnects," *Nature*, vol. 464, no. 7285, pp. 80–84, Mar. 2010.

[15] J. Michel, J. Liu, and L. C. Kimerling, "High-performance Ge-on-Si photodetectors," *Nat. Photon.*, vol. 4, no. 8, pp. 527–534, Aug. 2010.

[16] R. Gonzalez, B. M. Gordon, and M. A. Horowitz, "Supply and threshold voltage scaling for low power CMOS," *IEEE J. Solid-State Circuits*, vol. 32, no. 8, pp. 1210–1216, Aug. 1997.

[17] R. Chau, B. Doyle, S. Datta, J. Kavalieros, and K. Zhang, "Integrated nanoelectronics for the future," *Nat. Mater.*, vol. 6, no. 11, pp. 810–812, Nov. 2007.

[18] P. Dong, W. Qian, H. Liang, R. Shafiiha, N. Feng, D. Feng, X. Zheng, A. Krishnamoorthy, and M. Asghari, "Thermally tunable silicon racetrack resonators with ultralow tuning power," *Opt. Express*, vol. 18, no. 19, pp. 20298–20304, Sept. 2010.

[19] A. Liu, L. Liao, D. Rubin, J. Basak, Y. Chetrit, H. Nguyen, R. Cohen, N. Izhaky, and M. Paniccia, "Recent development in a high-speed silicon optical modulator based on reverse-biased pn diode in a silicon waveguide," *Semicond. Sci. Technol.*, vol. 23, no. 6, pp. 064001–064008, 2008.

[20] W. M. Green, M. J. Rooks, L. Sekaric, and Y. A. Vlasov, "Ultra-compact, low RF power, 10 Gb/s silicon Mach-Zehnder modulator," *Opt. Express*, vol. 15, no. 25, pp. 17106–17113, Dec. 2007.

[21] W De Cort, J. Beeckman, T. Claes, K. Neyts, and R. Baets, "Wide tuning of silicon-on-insulator ring resonators with a liquid crystal cladding," *Opt. Lett.*, vol. 36, no. 19, pp. 3876–3878, Sept. 2011.

[22] J. Pfeifle, L. Alloatti, W. Freude, J. Leuthold, and C. Koos, "Silicon-organic hybrid phase shifter based on a slot waveguide with a liquid-crystal cladding," *Opt. Express*, vol. 20, no. 14, pp. 15359–15376, Jun. 2012.

[23] W. H. P. Pernice and H. Bhaskaran, "Photonic non-volatile memories using phase change materials," *Appl. Phys. Lett.*, vol. 101, no. 17, pp. 171101–4, Oct. 2012.

[24] R. M. Briggs, I. M. Pryce, and H. A. Atwater, "Compact silicon photonic waveguide modulator based on the vanadium dioxide metal-insulator phase transition," *Opt. Express*, vol. 18, no. 11, pp. 11192–11201, May 2010.

[25] K. Padmaraju, D. F. Logan, T. Shiraishi, J. J. and Ackert, A. P. Knights, and K. Bergman, "Wavelength locking and thermally stabilizing microring resonators using dithering signals," *J. Lightwave Technol.*, vol. 32, no. 3, pp. 505–512, Feb. 2014.

[26] J. A. Cox, A. L. Lentine, D. C. Trotter, and A. L. Starbuck, "Control of integrated micro-resonator wavelength via balanced homodyne locking," *Opt. Express*, vol. 22, no. 9, pp. 11279–11289, May 2014.

[27] X. Zheng, E. Chang, P. Amberg, I. Shubin, J. Lexau, F. Liu, H. Thacker, S. S. Djordjevic, S. Lin, Y. Luo, J. Yao, J.-H. Lee, K. Raj, R. Ho, J. E. Cunningham, and A. V. Krishnamoorthy, "A high-speed, tunable silicon photonic ring modulator integrated with ultra-efficient active wavelength control," *Opt. Express*, vol. 22, no. 10, pp. 12628–12633, May 2014.

[28] C. R. Doerr, N. K. Fontaine, and L. L. Buhl, "PDM-DQPSK silicon receiver with integrated monitor and minimum number of controls," *IEEE Photon. Technol. Lett.*, vol. 24, no. 8, pp. 697–699, Apr. 2012.

[29] X. Zheng, E. Chang, P. Amberg, I. Shubin, J. Lexau, F. Liu, H. Thacker, S. S. Djordjevic, S. Lin, Y. Luo, J. Yao, J.-H. Lee, K. Raj, R. Ho, J. E. Cunningham, and A. V. Krishnamoorthy, "A high-speed, tunable silicon photonic ring modulator integrated with ultra-efficient active wavelength control," *Opt. Express*, vol. 22, no. 10, pp. 12628–12633, May 2014.

[30] B. G. Lee, A. V. Rylyakov, W. M. J. Green, S. Assefa, C. W. Baks, R. Rimolo-Donadio, D. M. Kuchta, M. H. Khater, T. Barwicz, C. Reinholm, E. Kiewra, S. M. Shank, C. L. Schow, and Y. A. Vlasov, "Monolithic silicon ntegration of scaled photonic switch fabrics, CMOS logic, and device driver circuits," *J. Lightwave Technol.*, vol. 32, no. 4, pp. 743–751, Feb. 2014.

[31] J. K. Doylend and A. P. Knights, "The evolution of silicon photonics as an enabling technology for optical interconnection," *Laser Photon. Rev.*, vol. 6, no. 4, pp. 504–525, Jul. 2012.

[32] P. DasMahapatra, R. Stabile, A. Rohit, and K. A. Williams, "Optical crosspoint matrix using broadband resonant switches," *IEEE J. Sel. Topics in Quantum Electron.*, vol. 20, no. 4, pp. 1–10, Aug. 2014.

[33] N. Sherwood-Droz, H. Wang, L. Chen, B. G. Lee, A. Biberman, K. Bergman, and M. Lipson, "Optical 4x4 hitless silicon router for optical Networks-on-Chip (NoC)," *Opt. Express*, vol. 16, no. 20, pp. 15915–15922, Sep. 2008.

[34] L. Chen and Y. Chen, "Compact, low-loss and low-power 8x8 broadband silicon optical switch," *Opt. Express*, vol. 20, no. 17, pp. 18977–18985, Aug. 2012.

[35] R. Ji, J. Xu, and L. Yang, "Five-port optical router based on microring switches for photonic networks-on-chip," *IEEE Photon. Technol. Lett.*, vol. 25, no. 5, pp. 492–495, Mar. 2013.

[36] D. A. B. Miller, "All linear optical devices are mode converters," *Opt. Express*, vol. 20, no. 21, pp. 23985–23993, Oct. 2012.

[37] D. J. Richardson, J. M. Fini, and L. E. Nelson, "Space-division multiplexing in optical fibres," *Nat. Photon.*, vol. 7, no. 5, pp. 354–362, May 2013.

[38] P. J. Winzer, "Making spatial multiplexing a reality," *Nat. Photon.*, vol. 8, no. 5, pp. 345–348, May 2014.

[39] X. Chen, A. Li, J. Ye, A. A. Amin, and W. Shieh, "Reception of mode-division multiplexed superchannel via few-mode compatible optical add/drop multiplexer," *Opt. Express*, vol. 20, no. 13, pp. 14302–14307, Jun. 2012.

[40] R. Ryf, S. Randel, A. H. Gnauck, C. Bolle, R. Essiambre, P. J. Winzer, D. W. Peckham, A. McCurdy, and R. Lingle, "Space-division multiplexing over 10 km of three-mode fiber using coherent 6x6 MIMO processing," *in Optical Fiber Communication Conference and Exposition (OFC/NFOEC), 2011 and the National Fiber Optic Engineers Conference*, (2011).

[41] N. K. Fontaine, "Devices and components for space-division multiplexing in few-mode fibers," *in Optical Fiber Communication Conference/National Fiber Optic Engineers Conference 2013*, paper OTh1B.3, OSA Technical Digest (online) (Optical Society of America, 2013).

[42] F. Xia, L. Sekaric, and Y. Vlasov, "Ultracompact optical buffers on a silicon chip," *Nat Photon.*, vol. 1, no. 1, pp. 65–71, 2007.

[43] A. Canciamilla, M. Torregiani, C. Ferrari, F. Morichetti, R. M. De La Rue, A. Samarelli, M. Sorel, and A. Melloni, "Silicon coupled-ring resonator structures for slow light applications: potential, impairments and ultimate limits," *J. Opt.*, vol. 12, no. 10, p. 104008, Sept. 2010.

[44] M. A. Popovic, T. Barwicz, E. P. Ippen, and F. X. Kartner, "Global design rules for silicon microphotonic waveguides: sensitivity, polarization and resonance tunability," *in Conference on Lasers and Electro-Optics/Quantum Electronics and Laser Science Conference and Photonic Applications Systems Technologies*, paper CTuCC1., Technical Digest (CD) (Optical Society of America, 2006).

[45] F. Morichetti, A. Canciamilla, C. Ferrari, M. Torregiani, A. Melloni, and M. Martinelli, "Roughness induced backscattering in optical silicon waveguides," *Phys. Rev. Lett.*, vol. 104, no. 3, pp. 033902–033904, Jan. 2010.

[46] F. Morichetti, A. Canciamilla, M. Martinelli, A. Samarelli, R. M. De La Rue, M. Sorel, and A. Melloni, "Coherent backscattering in optical microring resonators," *Appl. Phys. Lett.*, vol. 96, no. 8, pp. 081112–3, 2010.

[47] C. Ferrari, F. Morichetti, and A. Melloni, "Disorder in coupled-resonator optical waveguides," *J. Opt. Soc. Am. B*, vol. 26, no. 4, pp. 858–866, Mar. 2009.

[48] A. Melloni, A. Canciamilla, C. Ferrari, F. Morichetti, L. O'Faolain, T. F. Krauss, R. M. De La Rue, A. Samarelli, and M. Sorel, "Tunable delay lines in silicon photonics: coupled resonators and photonic crystals, a comparison," *IEEE Photon. Journal*, vol. 2, no. 2, pp. 181–194, Apr. 2010.

[49] S. Ibrahim, N. K. Fontaine, S. S. Djordjevic, B. Guan, T. Su, S. Cheung, R. P. Scott, A. T. Pomerene, L. L. Seaford, C. M. Hill, S. Danziger, Z. Ding, K. Okamoto, and S. J. B. Yoo, "Demonstration of a fast-reconfigurable silicon CMOS optical lattice filter," *Opt. Express*, vol. 19, no. 14, pp. 13245–13256, June 2011.

[50] F. Morichetti, A. Melloni, C. Ferrari, and M. Martinelli, "Error-free continuously-tunable delay at 10 Gbit/s in a reconfigurable on-chip delay-line," *Opt. Express*, vol. 16, no. 12, pp. 8395–8405, Mar. 2008.

[51] K. Padmaraju and K. Bergman, "Resolving the thermal challenges for silicon microring resonator devices," *Nanophotonics*, vol. 2, no. 4, pp. 1–14, Sept. 2013.

[52] Q. Fang, J. Song, X. Luo, L. Jia, M. Yu, G. Lo G, and Y. Liu, "High efficiency ring-resonator filter with NiSi heater," *IEEE Photon. Technol. Lett.*, vol. 24, no. 5, pp. 350–352, Mar. 2012.

[53] A. H. Atabaki, A. A. Eftekhar, S. Yegnanarayanan, and A. Adibi, "Sub-100-nanosecond thermal reconfiguration of silicon photonic devices," *Opt. Express*, vol. 21, no. 13, pp. 15706–15718, July 2013.

[54] J. Schrauwen, D. Van Thourhout, and R. Baets, "Trimming of silicon ring resonator by electron beam induced compaction and strain," *Opt. Express*, vol. 16, no. 6, pp. 3738–3743, Mar. 2008.

[55] Y. Shen, I. B. Divliansky, D. N. Basov, and S. Mookherjea, "Electric-field-driven nano-oxidation trimming of silicon microrings and interferometers," *Opt. Lett.*, vol. 36, no. 14, pp. 2668–2670, July 2011.

[56] C. J. Chen, J. Zheng, T. Gu, J. F. McMillan, M. Yu, G. Lo, D. L. Kwong, and C. W. Wong, "Selective tuning of high-Q silicon photonic crystal nanocavities via laser-assisted local oxidation," *Opt. Express*, vol. 19, no. 13, pp. 12480–12489, June 2011.

[57] D. Bachman, Z. Chen, A. M. Prabhu, R. Fedosejevs, Y. Y. Tsui, and V. Van, "Femtosecond laser tuning of silicon microring resonators," *Opt. Lett.*, vol. 36, no. 23, pp. 4695–4697, Dec. 2011.

[58] S. T. Chu, W. Pan, S. Sato, T. Kaneko, B. E. Little, and Y. Kokubun, "Wavelength trimming of a microring resonator filter by means of a UV sensitive polymer overlay," *IEEE Photon. Technol. Lett.*, vol. 11, no. 6, pp. 688–690, June 1999.

[59] D. K. Sparacin, C. Hong, L. C. Kimerling, J. Michel, J. P. Lock, and K. K. Gleason, "Trimming of microring resonators by photo-oxidation of a plasma-polymerized organosilane cladding material," *Opt. Lett.*, vol. 30, no. 17, pp. 2251–2253, 2005.

[60] J. Hu, N. Carlie, L. Petit, A. Agarwal, K. Richardson, and L. Kimerling, "Demonstration of chalcogenide glass racetrack microresonators," *Opt. Lett.*, vol. 33, no. 8, pp. 761–763, Apr. 2008.

[61] J. Hu, N. Carlie, N. N. Feng, L. Petit, A. Agarwal, K. Richardson, and L. Kimerling, "Planar waveguide-coupled, high-index-contrast, high-Q resonators in chalcogenide glass for sensing," *Opt. Lett.*, vol. 33, no. 21, pp. 2500–2502, Oct. 2008.

[62] A. Saliminia, A. Villeneuve, T. V. Galstyan, S. LaRochelle, and K. Richardson, "First and second-order Bragg gratings in single-mode planar waveguides of chalcogenide glasses," *J. Lightwave Technol.*, vol. 27, no. 5, pp. 837–842, May 1999.

[63] T. V. Galstyan, J. F. Viens, A. Villeneuve, K. Richardson, and M. A. Duguay, "Photoinduced self-developing relief gratings in thin film chalcogenide As2S3 glasses," *J. Lightwave Technol.*, vol. 15, no. 8, pp. 1343–1347, Aug. 1997.

[64] D. Ielmini, A. L. Lacaita, and D. Mantegazza, "Recovery and drift dynamics of resistance and threshold voltages in phase-change memories," *IEEE Trans. Electron Devices*, vol. 54, no. 2, pp. 308–315, Feb. 2007.

[65] N. Carlie, J. D. Musgraves, B. Zdyrko, I. Luzinov, J. Hu, V. Singh, A. Agarwal, L. C. Kimerling, A. Canciamilla, F. Morichetti, A. Melloni, and K. Richardson, "Integrated chalcogenide waveguide resonators for mid-IR sensing: leveraging material properties to meet fabrication challenges," *Opt. Express*, vol. 18, no. 25, pp. 26728–26743, Dec. 2010.

[66] M. A. Popovic, T. Barwicz, M. S. Dahlem, F. Gan, C. W. Holzwarth, P. T. Rakich, H. I. Smith, E. P. Ippen, and F. X. Kartner, "Tunable, fourth-order silicon microring-resonator add-drop filters," *in 33rd European Conference and Exhibition of Optical Communication (ECOC)*, paper 123, IET Seminar Digests (2007).

[67] Q. Lin, O. J. Painter, and G. P. Agrawal, "Nonlinear optical phenomena in silicon waveguides: modeling and applications," *Opt. Express*, vol. 15, no. 25, pp. 16604–16644, Nov. 2007.

[68] J. Hu, M. Torregiani, F. Morichetti, N. Carlie, A. Agarwal, K. Richardson, L. C. Kimerling, and A. Melloni, "Resonant cavity-enhanced photosensitivity in As2S3 chalcogenide glass at 1550 nm telecommunication wavelength," *Opt. Lett.*, vol. 35, no. 6, pp. 874–876, Mar. 2010.

[69] W. A. Zortman, D. C. Trotter, and M. R. Watts, "Silicon photonics manufacturing," *Opt. Express*, vol. 18, no. 23, pp. 23598–23607, Oct. 2010.

[70] K. Padmaraju, D. F. Logan, X. Zhu, J. J. Ackert, A. P. Knights, and K. Bergman, "Integrated thermal stabilization of a microring modulator," *Opt. Express*, vol. 21, no. 12, pp. 14342–14350, Jun. 2013.

[71] T. K. Liang, H. K. Tsang, I. E. Day, J. Drake, and A. P. Knights, "Silicon waveguide two-photon absorption detector at 1.5 μm wavelength for autocorrelation measurements," *Appl. Phys. Lett.*, vol. 81, no. 7, pp. 1323–1325, Aug. 2002.

[72] T. Tanabe, H. Sumikura, H. Taniyama, A. Shinya, and M. Notomi, "All-silicon sub-Gb/s telecom detector with low dark current and high quantum efficiency on chip," *Appl. Phys. Lett.*, vol. 96, no. 10, p. 101103, Mar. 2010.

[73] T. Baehr-Jones, M. Hochberg, and A. Scherer, "Photodetection in silicon beyond the band edge with surface states," *Opt. Express*, vol. 16, no. 3, pp. 1659–1668, Jan 2008.

[74] H. Chen, X. Luo, and A. W. Poon, "Cavity-enhanced photocurrent generation by 1.55 μm wavelengths linear absorption in a p-i-n diode embedded silicon microring resonator," *Appl. Phys. Lett.*, vol. 95, no. 17, pp. 171111–171113, Oct. 2009.

[75] J. D. B. Bradley, P. E. Jessop, and A. P. Knights, "Silicon waveguide-integrated optical power monitor with enhanced sensitivity at 1550 nm," *Appl. Phys. Lett.*, vol. 86, no. 24, pp. 241103–241113, Jun. 2005.

[76] M. W. Geis, S. J. Spector, M. E. Grein, R. T. Schulein, J. U. Yoon, D. M. Lennon, S. Deneault, F. Gan, F. X. Kaertner, and T. M. Lyszczarz, "CMOS-compatible all-Si high-speed waveguide photodiodes with high responsivity in near-infrared communication band," *Photon. Technol. Lett.*, vol. 19, no. 3, pp. 152–154, Feb. 2007.

[77] E. H. Nicollian and J. R. Brews, *MOS physics and technology*. New York, NY, USA: Wiley, 1982, 1982.

[78] W. Monch, *Semiconductor surfaces and interfaces*. Berlin, Germany: Springer-Verlag, 2001.

[79] M. Carminati, G. Ferrari, F. Guagliardo, and M. Sampietro, "ZeptoFarad capacitance detection with a miniaturized CMOS current front-end for nanoscale sensors," *Sens. Actuators A, Phys.*, vol. 172, no. 1, pp. 117–123, Dec. 2011.

[80] F. Morichetti, A. Canciamilla, C. Ferrari, A. Samarelli, M. Sorel, and A. Melloni, "Travelling-wave resonant four-wave mixing breaks the limits of cavity-enhanced all-optical wavelength conversion," *Nat. Commun.*, vol. 2, no. 296, pp. 115–116, May 2011.

[81] M. Casalino, G. Coppola, M. Iodice, I. Rendina, and L. Sirleto, "Near infrared sub-bandgap all-silicon photodetectors: state of the art and perspectives," *Sensors*, vol. 10, no. 12, pp. 10571–10600, Nov. 2010.

[82] D. M. Kim, H. C. Kim, and H. T. Kim, "Photonic high-frequency capacitance-voltage characterization of interface states in metal-oxide-semiconductor capacitors," *IEEE Trans. Electron. Devices*, vol. 49, no. 3, pp. 526–528, Mar. 2002.

[83] R. H. Bube, *Photoconductivity of solids*. New York, NY, USA: Krieger, 1978.

[84] A. Goossens and J. Schoonman, "The impedance of surface recombination at illuminated semiconductor electrodes: a non-equilibrium approach," *J. Electroanal. Chem.*, vol. 289, no. 1-2, pp. 11–27, Aug. 1990.

[85] J. R. Hauser, "Extraction of experimental mobility data for MOS devices," *IEEE Trans. Electron. Devices*, vol. 43, no. 11, pp. 1981–1988, Nov. 1996.

[86] Q. Xu, B. Schmidt, A. Pradhan, and M. Lipson, "Micrometre-scale silicon electro-optic modulator," *Nature*, vol. 435, no. 7040, pp. 325–327, May 2005.

[87] A. Griffith, J. Cardenas, C. B. Poitras, and M. Lipson, "High quality factor and high confinement silicon resonators using etchless process," *Opt. Express*, vol. 20, no. 19, pp. 21341–21345, Sept. 2012.

[88] G. Cocorullo, F. G. Della Corte, and I. Rendina, "Temperature dependence of the thermo-optic coefficient in crystalline silicon between room temperature and 550 K at the wavelength of 1523 nm," *Appl. Phys. Lett.*, vol. 74, no. 22, pp. 3338–33440, May 1999.

[89] R. S. Jacobsen, K. N. Andersen, P. I. Borel, J. Fage-Pedersen, L. H. Frandsen, O. Hansen, M. Kristensen, A. V. Lavrinenko, G. Moulin, H. Ou, C. Peucheret, B. Zsigri, and A. Bjarklev, "Strained silicon as a new electro-optic material," *Nature*, vol. 441, no. 7090, pp. 199–200, May 2006.

[90] M. Carminati, M. Vergani, G. Ferrari, L. Caranzi, M. Caironi, and M. Sampietro, "Accuracy and resolution limits in quartz and silicon substrates with microelectrodes for electrochemical biosensors," *Sens. Actuat. B*, vol. 174, pp. 168–175, Nov. 2012.

[91] M. Smit et al., "An introduction to InP-based generic integration technology," *Semicond. Sci. Technol.*, vol. 29, p. 083001, 2014.

[92] P. Chaisakul, D. Marris-Morini, J. Frigerio, D. Chrastina, M. S. Rouifed, S. Cecchi, P. Crozat, G. Isella, and L. Vivien, "Integrated germanium optical interconnects on silicon substrates," *Nat Photon.*, vol. 8, no. 6, pp. 482–488, May 2014.

[93] H. Rongrui and Y. Peidong, "Giant piezoresistance effect in silicon nanowires," *Nat. Nano.*, vol. 1, no. 1, pp. 42–46, Oct. 2006.

[94] P. T. Rakich, Z. P. Wang, and P. Davids, "Scaling of optical forces in dielectric waveguides: rigorous connection between radiation pressure and dispersion," *Opt. Lett.*, vol. 36, no. 2, pp. 217–219, Jan. 2011.

[95] P. T. Rakich, P. Davids, and Z. Wang, "Tailoring optical forces in waveguides through radiation pressure and electrostrictive forces," *Opt. Express*, vol. 18, no. 14, pp. 14439–14453, Jun. 2010.

[96] W. R. Thurber, R. L. Mattis, Y. M. Liu, and J. J. Filliben, "Resistivity-dopant density relationship for phosphorus-doped silicon," *J. Electrochem. Soc.*, vol. 127, no. 8, pp. 1807–1812, Apr. 1980.

[97] D. A. Antoniadis, A. G. Gonzalez, and R. W. Dutton, "Boron in near-intrinsic 100 and 111 silicon under inert and oxidizing ambient diffusion and segregation," *J. Electrochem. Soc.*, vol. 125, no. 5, pp. 813–819, May 1978.

[98] D. Melati, A. Melloni, and F. Morichetti, "Real photonic waveguides: guiding light through imperfections," *Adv. Opt. Photon.*, vol. 6, no. 2, pp. 156–224, Jun. 2014.

[99] R. A. Soref and B. R. Bennett, "Electrooptical effects in silicon," *IEEE Jour. of Quantum Electron.*, vol. 23, no. 1, pp. 123–129, Jan. 1987.

[100] Y. Kokubun, N. Funato, and M. Takizawa, "Athermal waveguides for temperature-independent lightwave devices," *IEEE Photon. Technol. Lett.*, vol. 5, no. 11, pp. 1297–1300, Nov. 1993.

[101] Y. Kokubun, S. Yoneda, and S. Matsuura, "Temperature-independent optical filter at 1.55 μm wavelength using a silica-based athermal waveguide," *Electron. Lett.*, vol. 34, no. 4, pp. 367–369, Feb. 1998.

[102] J.-M. Lee, D.-J. Kim, H. Ahn, S.-H. Park, and G. Kim, "Temperature dependence of silicon nanophotonic ring resonator with a polymeric overlayer," *J. Lightwave Technol.*, vol. 25, no. 8, pp. 2236–2243, Aug. 2007.

[103] V. Raghunathan, W. N. Ye, J. Hu, T. Izuhara, J. Michel, and L. Kimerling, "Athermal operation of silicon waveguides: spectral, second order and footprint dependencies," *Opt. Express*, vol. 18, no. 17, pp. 17631–17639, Aug. 2010.

[104] V. Raghunathan, *Athermal photonic devices and circuits on a silicon platform*. Massachusetts Institute of Technology, 2013. available online at http://hdl.handle.net/1721.1/79921.

[105] B. Guha, B. Kyotoku, and M. Lipson, "CMOS-compatible athermal silicon microring resonators," *Opt. Express*, vol. 18, no. 4, pp. 3487–3493, Feb. 2010.

[106] S. Dwivedi, H. D'heer, and W. Bogaerts, "A compact all-silicon temperature insensitive filter for WDM and bio-sensing applications," *IEEE Photon. Technol. Lett.*, vol. 25, no. 22, pp. 2160–2167, Nov. 2013.

[107] L. Zhou, K. Okamoto, and S. J. B. Yoo, "Athermalizing and trimming of slotted silicon microring resonators with UV-sensitive PMMA upper-cladding," *IEEE Photon. Technol. Lett.*, vol. 21, no. 17, pp. 1175–1177, Sept. 2009.

[108] A. van Popta, R. DeCorby, C. Haugen, T. Robinson, J. McMullin, D. Tonchev, and S. Kasap, "Photoinduced refractive index change in As2Se3 by 633nm illumination," *Opt. Express*, vol. 10, no. 15, pp. 639–644, Jul. 2002.

[109] D. K. Sparacin, R. Sun, A. M. Agarwal, M. A. Beals, J. Michel, L. C. Kimerling, T. J. Conway, A. T. Pomerene, D. N. Carothers, M. J. Grove, D. M. Gill, M. S. Rasras, S. S. Patel, and A. E. White, "Low-loss amorphous silicon channel waveguides for integrated photonics," *in 3rd IEEE International Conference on Group IV Photonics (IEEE, 2006)*, pp. 255–257.

[110] K. Tanaka, "Photoexpansion in As2S3 glass," *Phys. Rev. B*, vol. 57, no. 9, pp. 5163–5167, Mar. 1998.

[111] Z. Yang, N. C. Anheier Jr, H. A. Qiao, and P. Lucas, "Simultaneous microscopic measurements of photodarkening and photoexpansion in chalcogenide films," *J. Phys. D*, vol. 42, no. 13, p. 135412, June 2009.

[112] L.-W. Luo, G. S. Wiederhecker, K. Preston, and M. Lipson, "Power insensitive silicon microring resonators," *Opt. Lett.*, vol. 37, no. 4, pp. 590–592, Feb. 2012.

[113] S. S. Djordjevic, K. Shang, B. Guan, S. T. S. Cheung, L. Liao, J. Basak, H.-F. Liu, and S. J. B. Yoo, "CMOS-compatible, athermal silicon ring modulators clad with titanium dioxide," *Opt. Express*, vol. 21, no. 12, pp. 13958–13968, Jun. 2013.

[114] B. Guha, J. Cardenas, and M. Lipson, "Athermal silicon microring resonators with titanium oxide cladding," *Opt. Express*, vol. 21, no. 2, pp. 26557–26563, Nov. 2013.

[115] J. D. B. Bradley, C. Evans, J. T. Choy, O. Reshef, P. B. Deotare, F. Parsy, K. C. Phillips, M. Lončar, and E. Mazur, "Submicrometer-wide amorphous and polycrystalline anatase TiO2 waveguides for microphotonic devices," *Opt. Express*, vol. 20, no. 21, pp. 23821–23831, Oct. 2012.

[116] F. Qiu, A. M. Spring, F. Yu, S. Yokoyama, "Complementary metal-oxide-semiconductor compatible athermal silicon nitride/titanium dioxide hybrid micro-ring resonators," *Appl. Phys. Lett.*, vol. 102, no. 5, pp. 051106–3, Feb. 2013.

[117] S. Zhu, G.-Q. Lo, J. Xie, and D.-L. Kwong, "Toward athermal plasmonic ring resonators based on Cu-TiO2-Si hybrid plasmonic waveguide," *IEEE Photon. Technol. Lett.*, vol. 25, no. 12, pp. 1161–1164, Jun. 2013.

[118] J. Bovington, R. Wu, K.-T. Cheng, and J. E. Bowers, "Thermal stress implications in athermal TiO2 waveguides on a silicon substrate," *Opt. Express*, vol. 22, no. 1, pp. 661–666, Jan. 2014.

[119] S. Valencia, A. Crassous, L. Bocher, V. Garcia, X. Moya, R. O. Cherifi, C. Deranlot, K. Bouzehouane, S. Fusil, A. Zobelli, A. Gloter, N. D. Mathur, A. Gaupp, R. Abrudan, F. Radu, A. Barthelemy, and M. Bibes, "Interface-induced room-temperature multiferroicity in BaTiO3," *Nat. Mat.*, vol. 10, no. 10, pp. 753–758, Aug. 2011.

[120] G. Radaelli, S. Brivio, I. Fina, and R. Bertacco, "Correlation between growth dynamics and dielectric properties of epitaxial BaTiO3 films," *Appl. Phys. Lett.*, vol. 100, no. 10, pp. 102904–4, 2012.

[121] A. Petraru, J. Schubert, M. Schmid, and C. Buchal, "Ferroelectric BaTiO3 thin-film optical waveguide modulators," *Appl. Phys. Lett.*, vol. 81, no. 8, pp. 1375–1377, 2002.

[122] D. Chen, T. E. Murphy, S. Chakrabarti, and J. D. Phillips, "Optical waveguiding in BaTiO3 /MgO/AlxOy /GaAs heterostructures," *Appl. Phys. Lett.*, vol. 85, no. 22, pp. 5206–5208, Nov. 2004.

[123] P. Tang, D.J. Towner, A.L. Meier, and B.W. Wessels, "Low-Loss electrooptic BaTiO3 thin film waveguide modulator," *IEEE Photon. Technol. Lett.*, vol. 16, no. 8, pp. 1837 – 1839, Aug. 2004.

[124] C. Xiong, W. H. P. Pernice, J. H. Ngai, J. W. Reiner, D. Kumah, F. J. Walker, C. H. Ahn, H. X. Tang, "Active silicon integrated nanophotonics: ferroelectric BaTiO3 devices," *Nano Lett.*, vol. 14, no. 3, pp. 1419–1425, Jan. 2014.

[125] S. Abel, T. Stoferle, C. Marchiori, D. Caimi, L. Czornomaz, C. Rossel, M. Rossell, R. Erni, M. Sousa, H. Siegwart, J. Hofrichter, M. Stuckelberger, A. Chelnokov, B. J. Offrein, and J. Fompeyrine, "Electro-optical active barium titanate thin films in silicon photonics devices," *in Advanced Photonics 2013*, OSA Technical Digest (online) (Optical Society of America, 2013), paper IW4A.5.

[126] H. Chaib, L. M. Eng, and T. Otto, "Dielectric polarization and refractive indices of ultrathin barium titanate films on strontium titanate single crystals," *J. Phys. Condens. Matter*, vol. 17, no. 1, pp. 161–179, Jan. 2012.

[127] J. Feinberg, D. Heiman, A. R. Tanguay Jr., and R. W. Hellwarth, "Photorefractive effects and light induced charge migration in barium titanate," *J. Appl. Phys.*, vol. 51, no. 3, pp. 1297–1305, 1980.

[128] K. Padmaraju, J. Chan, L. Chen, M. Lipson, and K. Bergman, "Thermal stabilization of a microring modulator using feedback control," *Opt. Express*, vol. 20, no. 27, pp. 27999–28008, Dec. 2012.

[129] W. A. Zortman, A. L. Lentine, D. C. Trotter, and M. R. Watts, "Bit-error-rate monitoring for active wavelength control of resonant modulators," *IEEE Micro*, vol. 33, no. 1, pp. 42–52, Jan. 2013.

[130] M. Carminati, *et al.*, "Low-noise CMOS impedance sensing chip for transparent light tracking in integrated photonics," *manuscript in preparation*, Jul. 2014.

[131] L.-W. Luo, N. Ophir, C. P. Chen, L. H. Gabrielli, C. B. Poitras, K. Bergman, and M. Lipson, "WDM-compatible mode-division multiplexing on a silicon chip," *Nat. Comm.*, vol. 5, no. 12, Jan. 2014.

[132] Y. Zheng and J. Duan, "Alignment algorithms for planar optical waveguides," *Optical Engineering*, vol. 51, no. 10, p. 103401, Oct. 2012.

[133] R. Hauffe, U. Siebel, K. Petermann, R. Moosburger, J. R. Kropp, and F. Arndt, "Methods for passive fiber chip coupling of integrated optical devices," *IEEE Trans. on Advanced Packaging*, vol. 24, no. 4, pp. 450–455, Nov. 2001.

[134] F. Morichetti, C. Ferrari, A. Canciamilla, and A. Melloni, "The first decade of coupled resonator optical waveguides: bringing slow light to applications," *Laser Photon. Rev.*, vol. 6, no. 1, pp. 74–96, Jan. 2012.

[135] A. Melloni, F. Morichetti, C. Ferrari, and M. Martinelli, "Continuously tunable 1 byte delay in coupled-resonator optical waveguides," *Opt. Lett.*, vol. 33, no. 20, pp. 2389–2391, Oct. 2008.

[136] A. H. Gnauck and P. J. Winzer, "Optical phase-shift-keyed transmission," *J. Lightwave Technol.*, vol. 23, no. 1, pp. 115–130, Jan. 2005.

[137] G. Bosco and P. Poggiolini, "On the joint effect of receiver impairments on direct-detection DQPSK systems," *J. Lightwave Technol.*, vol. 24, no. 3, pp. 1323–1333, Mar. 2006.

[138] B. Mikkelsen, C. Rasmussen, P. Mamyshev, and F. Liu, "Partial DPSK with excellent filter tolerance and OSNR sensitivity," *Electron. Lett.*, vol. 42, no. 23, pp. 1363–1364, Nov. 2006.

[139] Y. K. Lize, L. Christen, X. Wu, J. Y. Yang, S. Nuccio, T. Wu, A. E. Willner, and R. Kashyap, "Free spectral range optimization of return-to-zero differential phase shift keyed demodulation in the presence of chromatic dispersion," *Opt. Express*, vol. 15, no. 11, pp. 6817–6822, May 2007.

[140] O. Gerstel, M. Jinno, A. Lord, and S. J. B. Yoo, "Elastic optical networking: a new dawn for the optical layer?," *IEEE Communications Magazine*, vol. 50, no. 2, pp. s12–s20, Feb. 2012.

[141] K. Xu, G.K.P. Lei, S.M.G. Lo, Z. Cheng, C. Shu, and H.K. Tsang, "Bit-rate-variable DPSK demodulation using silicon microring resonators with electro-optic wavelength tuning," *IEEE Photon. Technol. Lett.*, vol. 24, no. 14, pp. 1221–1223, Jul. 2012.

[142] J. Li, K. Worms, R. Maestle, D. Hillerkuss, W. Freude, and J. Leuthold, "Free-space optical delay interferometer with tunable delay and phase," *Opt. Express*, vol. 19, no. 12, pp. 11654–11666, Jun. 2011.

[143] Y. Dai and C. Shu, "Bit-rate variable DPSK demodulation based on cascaded four-wave mixing," *Opt. Express*, vol. 19, no. 4, pp. 2952–2958, Feb. 2011.

[144] Y. Nasu, K. Hattori, T. Saida, Y. Hashizume, and Y. Sakamaki, "Silica-based adaptive-delay DPSK demodulator with a cascaded Mach-Zehnder interferometer configuration," *in Proceed. 36th European Conference on Optical Communications*, Sept. 2010.

[145] K. Suzuki, H. Nguyen, T. Tamanuki, F. Shinobu, Y. Saito, Y. Sakai, and T. Baba, "Slow-light-based variable symbol-rate silicon photonics DQPSK receiver," *Opt. Express*, vol. 20, no. 4, pp. 4796–4804, Feb. 2012.

[146] A. Melloni and M. Martinelli, "Synthesis of direct-coupled-resonators bandpass filters for WDM systems," *J. Lightwave Technol.*, vol. 20, no. 2, pp. 296–303, Feb. 2002.

[147] T. Barwicz, M. R. Watts, M. A. Popovic, P. T. Rakich, L. Socci, F. X. Kartner, E. P. Ippen, and H. I. Smith, "Polarization-transparent microphotonic devices in the strong confinement limit," *Nat. Photon.*, vol. 1, no. 1, pp. 57–60, Jan. 2007.

[148] H. Fukuda, K. Yamada, T. Tsuchizawa, T. Watanabe, H. Shinojima, and S. Itabashi, "Silicon photonic circuit with polarization diversity," *Opt. Express*, vol. 16, no. 7, pp. 4872–4880, Mar. 2008.